

NORTHWESTERN UNIVERSITY

Element-Specific Magnetism Studies on Patterned Magnetic
Structures and Magnetic Films

A DISSERTATION

SUBMITTED TO THE GRADUATE SCHOOL
IN PARTIAL FULFILLMENT OF THE REQUIREMENTS

for the degree

DOCTOR OF PHILOSOPHY

Field of Materials Science and Engineering

By

Yongseong Choi

EVANSTON, ILLINOIS

June 2005

UMI Number: 3177701

Copyright 2005 by
Choi, Yongseong

All rights reserved.

INFORMATION TO USERS

The quality of this reproduction is dependent upon the quality of the copy submitted. Broken or indistinct print, colored or poor quality illustrations and photographs, print bleed-through, substandard margins, and improper alignment can adversely affect reproduction.

In the unlikely event that the author did not send a complete manuscript and there are missing pages, these will be noted. Also, if unauthorized copyright material had to be removed, a note will indicate the deletion.

UMI[®]

UMI Microform 3177701

Copyright 2005 by ProQuest Information and Learning Company.

All rights reserved. This microform edition is protected against
unauthorized copying under Title 17, United States Code.

ProQuest Information and Learning Company
300 North Zeeb Road
P.O. Box 1346
Ann Arbor, MI 48106-1346

© Copyright by Yongseong Choi 2005

All Rights Reserved

ABSTRACT

Element-Specific Magnetism Studies on Patterned Magnetic Structures and Magnetic Films

Yongseong Choi

In continuous (Fe/Gd) and patterned (Fe/Gd, NiFe/Co) magnetic multilayer films, the effects of interfacial coupling, proximity, anisotropy (intrinsic and shape), and termination were investigated, and how they modify the magnetization reversal processes and magnetization depth profiles was studied. X-ray resonant scattering and absorption techniques combined with micromagnetic simulations were used to study films in an element specific and depth-resolved way.

In an aligned-phase Fe/Gd multilayer, the Gd layers near the Fe/Gd interfaces were studied using x-ray resonant magnetic scattering measurements. From the experimental results, the Gd layer-specific magnetization depth profiles were obtained. An enhanced magnetic ordering in the interfacial Gd layers was observed, and the observed results were consistent with theoretical calculation results and x-ray magnetic circular dichroism measurement results.

A termination layer effect and the role of magnetic anisotropy in the Fe layers were studied on different sets of Fe/Gd multilayers that showed twisted magnetic states. X-ray magnetic circular dichroism (XMCD) measurements were performed in a surface-to-bulk way. The experimental results were reproduced in micromagnetic simulations, and the observed features near the compensation point were explained by the combined effect of a termination layer and a magnetic anisotropy.

Magnetic domain configurations were studied in a hole array patterned Fe/Gd multilayer using XMCD measurements and micromagnetic simulations. The interplay between an intrinsic anisotropy and a shape anisotropy affected domain configurations, and coherent rotations of three types of domains were observed. Similarly, on a pseudo-spin-value type patterned film, local magnetization was measured using XMCD with micro-focused x-ray beams.

On patterned dot array films, it was demonstrated that the layer selective magnetization depth profiles could be obtained from patterned arrays using x-ray resonant magnetic scattering.

Approved

Professor Michael J. Bedzyk
Department of Materials Science and Engineering
Northwestern University Evanston, IL

Final Examination Committee:
Prof. Michael J. Bedzyk, Chair
Dr. George Srajer
Prof. David N. Seidman
Prof. Mark C. Hersam

Acknowledgements

First of all, I would like to thank God for giving me an opportunity to study at Northwestern University and a chance to work with great people at Argonne National Laboratory.

I am grateful to my advisors Professor Michael Bedzyk and Dr. George Srajer for their advice and guidance. I would like to thank Dr. Srajer for his encouragement and support. I would also like to express my gratitude to my two mentors Dr. Dongryeol Lee and Dr. Daniel Haskel. I appreciate their patience and time spent to teach me hands-on knowledge in XRMS and XMCD. I thank Dr. Jonathan Lang for his help and advice on my experiments. I thank Drs. John Freeland, Andy Cady, Zahirul Islam, and Dave Keavney for being supportive and helpful.

Most of all, I am grateful to my parents for their love and trust, and I thank my wife for having faith in me and always making me feel what I do is meaningful and important.

Contents

ABSTRACT	iii
Acknowledgements	v
List of Tables	ix
List of Figures	x
Chapter 1. Introduction	1
1.1. Magnetic thin films and artificially patterned magnetic films	1
1.2. Magnetism and X rays	5
Chapter 2. Structural and Magnetic Characterization of Antiferromagnetically Coupled Fe/Gd Multilayers	12
2.1. Background	12
2.2. Interfacial Magnetism Study on Antiferromagnetically Coupled Fe/Gd Multilayers using X-ray Resonant Magnetic Scattering	15
2.3. Discussion	37
2.4. Conclusion	46
Chapter 3. Spin reorientations and surface effects in Fe/Gd magnetic films	48
3.1. Background	48

3.2. Measurement of inhomogeneous magnetization using surface-to-bulk sensitive XMCD	51
3.3. Results and Discussion	61
3.4. Conclusion	76
Chapter 4. Magnetic Domain Studies on Patterned Structures	77
4.1. Magnetic Hole Arrays	79
4.2. Pseudo-spin-value wire	96
Chapter 5. Structural and magnetic characterization of Co dot arrays using soft x-ray resonant magnetic scattering	105
5.1. Experiments	106
5.2. Analysis and Discussion	110
5.3. Future Work	113
5.4. Conclusion	118
Chapter 6. Conclusion	119
References	122
Appendix A. Specular X-ray Reflectivity	132
A.1. Parratt's recursive relation with Nevot-Croce roughness	132
A.2. Geometrical correction and resolution function	135
Appendix B. Experimental Setup for Magnetism studies using polarized synchrotron radiations	138
B.1. Beamline Optics: phase retarder, monochromator, microfocusing	138

B.2. Beamline Setup for Experiments	145
Appendix C. Atomic scattering factors for x-ray resonant scattering	148
C.1. Atomic scattering factors near resonant energies	148
C.2. Optical constants	151
Appendix D. Micromagnetic Simulation	153

List of Tables

2.1	Parameters derived from fits to the charge-magnetic specular reflectivity data.	38
3.1	Optical constants of Gd and Fe at a non-resonant (7.0 keV) and a resonant energy of Gd (7.245 keV).	53
3.2	Parameters from fits to the measured reflectivity on the two Fe/Gd multilayers.	53
3.3	Critical angles θ_C for Gd and Fe layers at 7.112 (Fe K) and 7.247 (Gd L_3) keV.	58

List of Figures

1.1	Illustrations of giant magnetoresistance, exchange bias, and superparamagnetism.	3
1.2	Illustration of x-ray resonant scattering and absorption process used in characterization of ferromagnetic materials.	10
1.3	Schematic of magnetic dichroic signal measurements.	11
2.1	Theoretical saturation moments of bulk Gd and Fe are plotted as a function of temperature.	13
2.2	Phase diagram of magnetic phases of a Fe/Gd multilayer.	14
2.3	SQUID magnetometry measurements on the Fe/Gd multilayer.	18
2.4	Experimental setup at beamline 4ID of APS at ANL.	19
2.5	Scattering geometry.	20
2.6	The XMCD measurements on the Fe/Gd multilayer for opposite orientations of photon wave vector and sample magnetization.	23
2.7	The XRMS measurements at $\phi = 0^\circ$ and 90°	24
2.8	Charge-magnetic reflectivity measurements at temperatures 20, 100, 200, and 300 K.	25

2.9	Specular reflectivity measurements (symbols), the DWBA calculation (red lines), the BA calculation (blue lines).	33
2.10	Charge-magnetic reflectivity curves in Fig. 2.9 are re-plotted, and the BA and DWBA calculations are plotted separately.	34
2.11	DWBA fitting results with a uniform Gd-layer magnetization model was compared with the DWBA fitting results in Fig. 2.9.	35
2.12	Calculated electric field intensity profiles are shown for the six Bragg peak angles.	36
2.13	Gd magnetization profiles.	42
2.14	Specular reflectivity (dark) and off-specular reflectivity (gray) measurements.	44
2.15	Average Gd layer magnetization at each temperature.	45
3.1	Possible magnetic states of a ferrimagnetic (Fe/Gd) multilayer depending on temperature, applied field, and layer thickness.	50
3.2	SQUID measurements on the Fe-terminated and Gd-terminated (Fe/Gd) multilayers.	51
3.3	X-ray reflectivity curves measurements on Fe/Gd multilayers at 7.0 and 7.245 keV.	56
3.4	XMCD measurements on the Fe/Gd multilayer across the Gd L_3 and the Fe K absorption edges.	57

3.5	Calculated electric field intensity inside the multilayers at a grazing incident angle, 0.355° .	58
3.6	Gd layer magnetization at temperatures between 20 and 300 K.	60
3.7	XMCD-hysteresis loops from the Fe-terminated sample at 45, 65, 80, 90, 115, and 145 K.	67
3.8	Micromagnetic simulations on the Fe-terminated multilayer.	68
3.9	The effect of a weak anisotropy in Fe layers.	69
3.10	Spin configurations from the simulations for the Fe-terminated sample at a temperature near T_{Comp} at the selected field values as the field was swept as in Figure 3.8.	70
3.11	Surface and bulk magnetization directions at (1) surface twist state, (2) near T_{Comp} , and (3) bulk twisted state.	71
3.12	Spin configurations from the micromagnetic simulations are shown for the Fe-terminated sample at a temperature below T_{Comp} at the selected field values as the field was swept as in Figure 3.8.	72
3.13	Spin configurations from the simulations for the Fe-terminated sample at a temperature above T_{Comp} at the selected field values as the field was swept as in Figure 3.8.	73
3.14	XMCD-hysteresis loops from the Gd-terminated sample at 80, 95, and 103 K.	74

3.15	Micromagnetic simulations on the Gd-terminated multilayer.	75
4.1	Patterning by e-beam lithography and lift-off process.	78
4.2	Experimental geometry for MOKE measurements.	81
4.3	MOKE measurements on the unpatterned film.	82
4.4	MOKE measurements on the patterned film.	84
4.5	Experimental geometry for XMCD vector magnetometry setup.	85
4.6	XMCD energy scan around the Fe K absorption edge.	86
4.7	XMCD experimental results and micromagnetic simulation results on the hole array.	87
4.8	θ -rocking scans on the hole array.	88
4.9	Micromagnetic simulations of the hole array with different parameters.	92
4.10	Spin configurations of the hole array.	93
4.11	A pseudo-spin-value structure patterned into a wire shape.	98
4.12	XMCD hysteresis loops measured from the buried Co layer and micromagnetic simulations on the Co layer.	102
4.13	Micromagnetic simulations results on the Co and permalloy layers.	103
5.1	SEM image of the Co dot array and scattering geometry for soft x-ray resonant magnetic scattering.	107

5.2	SXRMS measurements on the Co dot array.	109
5.3	Geometry for x-ray scattering measurements on the Co dot array.	111
5.4	SXRMS reflectivity data and fits for the Co dot array.	112
5.5	The fitted parameters and model used for the SXRMS reflectivity fit.	113
5.6	Layer selective magnetization hysteresis loops from the permalloy(Py, Ni ₈₀ Fe ₂₀)-Cobalt dot arrays with and without a spacer layer.	116
5.7	SXRMS reflectivity data from the permalloy(Py, Ni ₈₀ Fe ₂₀)-Cobalt dot arrays with and without a spacer layer.	117
A.1	Multilayer structure with N layers on a substrate.	133
A.2	An interface with roughness and an interface with intermixing.	134
A.3	Geometrical factor correction at grazing incident angles.	136
A.4	A footprint scan for the geometrical factor correction at grazing incident angles.	136
B.1	The beamline optics at 4ID-A/B, APS, ANL.	140
B.2	Diamond phase retarder for circularly polarized x rays.	141
B.3	Phase retarder scan.	143
B.4	<i>Pharet</i> program for calculation of the phase retarder offset angle.	143
B.5	Calculated phase retarder offset angle.	144

B.6	Pd mirror to reject higher harmonics.	144
B.7	The beamline setup for scattering experiments at 4ID-D, APS, ANL.	147
B.8	The beamline setup for microfocusing experiments at 4ID-D, APS, ANL.	147
C.1	Absorption measurements in fluorescence geometry near the Gd L ₂ edge at T=20 K, and 2.1 kOe applied field.	150

CHAPTER 1

Introduction

1.1. Magnetic thin films and artificially patterned magnetic films

Recent advances in lithographic and other fabrication techniques have led to the fabrication of a number of novel magnetic systems at the nanometer length scale. The reduced dimensions in these systems lead to modified physical properties, and as dissimilar materials are brought together in these systems, novel magnetic behaviors, such as giant magneto-resistance [1] and exchange coupling [2], have been observed (Fig. 1.1). In these artificial systems, a better knowledge of the interactions occurring at the nanometer length scale is crucial to understand the overall behavior of the systems. As the overall dimensions are reduced, the magnetic interactions occurring at surfaces, interfaces, and confined geometries become more important due to their increased contribution to the overall properties. As it is in the case of giant magneto-resistance and exchange coupling, many of these artificial structures are inhomogeneous. In these systems with alloyed or heterostructured layers, it also becomes important to gain fundamental knowledge of the contributions from the individual constituents.

Periodic arrays of magnetic structures have received much attention recently because of their potential as high density magnetic storage media. One of the major driving forces in information storage technologies is to increase the density of stored

information per media volume. With the conventional continuous magnetic thin films, one bit is stored in a few tens of magnetic grains. To increase the area density, the number of grain per bit or a grain size has to decrease. However, this approach of increasing density will soon reach the physical limit [superparamagnetic limit, illustrated in Fig. 1.1(c)] where reduced volume per bit can be unstable to primarily thermal fluctuations. With the recent advances in patterning techniques, it has been suggested that patterning magnetic films can be a viable alternative to the current continuous film technology. In addition, from the fundamental point of view, because of the reduced size and lateral confinement effects, the patterned structures show magnetic behaviors different from their counterparts of the continuous film structures.

In magnetic multilayers, the overall magnetic behavior is often determined by the magnetic interactions at interfaces. For example, the interface magnetism plays a crucial role in giant magnetoresistance [1], exchange biased [2] systems, spin tunnel [3], and spintronics [4]. In some antiferromagnetic multilayers, the competition between the exchange, Zeeman, and anisotropy interactions can lead to a spin flop transition, resulting in a canting of sublattice magnetization [5]. At magnetic interfaces and surfaces, magnetic behaviors are often different from their bulk counterparts so that changes in magnetic transition ordering temperature, magnetic moment, magnetic anisotropy, and spin orientations can occur. For example, in antiferromagnets with the spin flop transition, spin flop transition at surface was observed to occur at lower fields than the bulk transition [6]. However, the determination of the structural and magnetic properties of surfaces, interfaces, and confined structures still remains to be challenging due to the difficulty of detecting and isolating contributions from these.

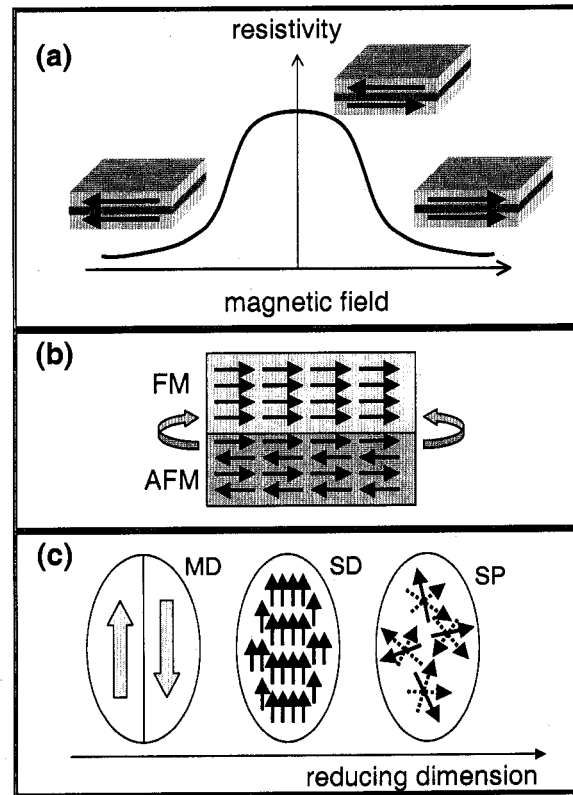


Figure 1.1. Illustrations of giant magnetoresistance (GMR), exchange bias, and superparamagnetism. (a) GMR exploits the dependence of resistivity on the spin orientations in the two ferromagnetic layers. (b) Exchange bias effect due to the interlayer coupling between a ferromagnetic (FM) and antiferromagnetic (AFM) layers. (c) Magnetic domain states in a ferromagnet at different dimensions. MD: multi-domain state, SD: single domain at a few hundreds nanometers to a few microns, and SP: superparamagnetic state at a few tens of nanometers. In the superparamagnetic state, no stable magnetization is reachable and the moment orientations are randomly distributed in space due to thermal fluctuation.

Most common techniques for magnetization characterizations are MFM (magnetic force microscopy), MOKE (magneto-optical Kerr effect), SQUID (superconducting quantum interference device), and magnetic neutron scattering. MFM is based on atomic force microscope (AFM) where a magnetic probe tip interacts with the magnetic fields generated by the sample. MFM-imaging can achieve high spatial resolution (sub-100 nm), but the disadvantage is that the MFM is an indirect probe and that the measured interactions are often difficult to quantify. What is measured in MFM-imaging is the spatial derivatives of the fields generated by a magnetic sample. In MOKE measurements, the interaction between polarized laser light and a magnetic sample is measured. Some of the limitations of the MOKE are limited penetration depth of visible light and wavelength-limited scattering. In SQUID measurements, sample magnetic moments can be directly measured, and relatively wide ranges of temperature and field can be studied. In magnetic neutron scattering, the direct coupling between neutron spin and sample spin and orbital moments are used. With neutrons, the magnetic scattering amplitude is very large, but neutron scattering generally have smaller q -range is limited, it typically requires relatively larger samples compared with other techniques. Compared with the neutron scattering, magnetic scattering amplitude with x rays is weaker, but the x-ray based magnetic scattering can typically achieve higher spatial resolution. The most evident advantage of x-ray based magnetic characterizations is element-specificity that can be achieved with resonant techniques.

The objective of this thesis is to investigate the role of interfaces in magnetic thin films and the effect of artificial patterning on magnetic domains. Taking an advantage

of x-ray's unique capabilities (element-specificity and ability to probe buried structures), x-ray scattering and spectroscopy techniques were used to gain more insight into the role of interfaces in magnetic multilayer films in a layer-selective way. To study the magnetic domains from patterned structures, a combined approach of x-ray spectroscopy and micromagnetic simulation was used. The outline of the thesis is as follows. In the first chapter, the introduction of x-ray and magnetic materials is briefly presented. X-ray resonant magnetic scattering studies for the interface magnetism in Fe/Gd multilayers are presented in chapter 2. Field dependent spin reorientations of Fe/Gd multilayers are presented in chapter 3. In chapter 4, magnetic domain studies on patterned magnetic structures are presented. In chapter 5, x-ray resonant magnetic scattering results on dot arrays are presented. In chapter 6 these results are summarized.

1.2. Magnetism and X rays

Magnetism arises from the spin of electrons, the orbital motion of the electrons, and the interaction of the two. Depending on the response to externally applied magnetic fields, materials can be categorized as diamagnetic, paramagnetic, or ferromagnetic. Diamagnetism is a weak magnetism that can be found in all materials and it opposes applied magnetic fields. Paramagnetism is stronger than diamagnetism and causes magnetization proportional to the applied magnetic field in the same direction. At finite temperatures, the spins in paramagnetic materials are thermally agitated and oriented randomly without an external field.

Compared with diamagnetism and paramagnetism, ferromagnetism is a stronger effect, and ferromagnetic materials exhibit distinct characteristics such as spontaneous magnetization, magnetic hysteresis, and saturation. Below the transition temperature (Curie temperature) ferromagnetic materials are divided into spontaneously magnetized small domains without an external field. However the magnetization vectors of these domains are randomly oriented so that the net resultant magnetization is zero. The effect of an applied field in ferromagnetic materials is not to induce magnetization in atomic level, but rather to align the magnetization vectors of spontaneously magnetized domains.

The materials having ferromagnetic ordering are transition metals, rare-earth elements and their alloys. For transition metals (Ni, Co, Fe) ferromagnetic ordering is due to the unpaired electrons in unfilled $3d$ shells. For rare-earths (for example, Gd) ferromagnetic ordering is due to the unpaired electrons in unfilled $5d$ and localized $4f$ shells. In rare-earths, $4f$ electron wave functions are highly localized, and the magnetic ordering is explained by the indirect exchange between $4f$ electrons through the spin-polarized $5d$ - $6s$ conduction electrons. In transition metals, ferromagnetism is described by the Stoner model (itinerant electron model) [7]. The contributions of paired electrons in filled shells to magnetic moments are cancelled by the contributions of the electrons with the opposite sign. For ferromagnetic metals, electronic bands are split into two: one band with majority spin and the other with minority spin. The magnetic exchange splitting between majority and minority spin band contributes to ferromagnetism. The magnetic exchange splitting is the average energy shift between electrons with up spin relative to ones with down spin. Due to the

exchange splitting, the minority spin band is filled less than the majority band as illustrated in Fig. 1.2(a), and this causes the spin imbalance that produces magnetic moments [8].

X rays interact with matter through the electron's charge and its magnetic moment. With x rays, magnetic materials can be studied by scattering and absorption processes, but the interaction between x rays and the electron's magnetic moment is relatively weak. At a non-resonant energy, magnetic scattering intensities are usually a few orders of magnitude smaller than charge scattering intensities. On a electron, a plane polarized electromagnetic wave exerts a magnetic force and a electric force, and the magnetic force is smaller than the electric force by the ratio of the photon energy to the electron rest mass energy. This ratio is typically a few percent. In addition, all electrons (paired/unpaired) contribute to the charge density while only unpaired electrons contribute to the magnetization density. These two combined effects cause a magnetic scattering amplitude to be a few order of magnitude smaller than a charge scattering amplitude. Moreover, the measured intensity in an experiment is proportional to the square of the amplitude, causing magnetic signals to be very weak [9].

Magnetic scattering/absorption intensities are not only small, but the formalism is relatively complicated. However, the essential point is that there is a strong polarization and energy dependence on the scattered intensity. Resonant magnetic scattering technique is often used for magnetic materials to achieve an enhancement in measured signals. For the resonant magnetic scattering, the incident x-ray energy is set to the absorption edge of an element of interest. At the $L_{2,3}$ edges in the rare-earth, the

M_{2-4} edges in the actinide elements, and the K and L edges in the transition metals, significantly enhanced resonant magnetization-sensitive x-ray scattering occurs. These magnetic resonant behaviors are due to electric multipole transitions and the sensitivity to the magnetization results from exchange. The resonant increase with polarization dependence can be explained in terms of electric quadrupole ($E2$) transitions to $4f$ levels and electric dipole ($E1$) transitions to $5d$ levels. The exclusion principle allows only transitions to unoccupied orbitals, causing an “exchange interaction” sensitive to the magnetization of the f and d bands [10]. Resonant scattering process may be explained as, (1) the absorption of an incident photon, (2) the creation of a short lived intermediate (excited) state, and (3) decay of that state back into the ground state through the emission of an elastically scattered photon [11] as illustrated in Fig. 1.2(b).

Exploiting the polarization dependence, magnetic materials can be studied with absorption x-ray techniques through dichroic effect. The term “dichroism” in optics refers to the property of certain materials of having different absorption coefficients for polarized light in different directions. Because one color of light can be absorbed preferentially, the material appears to have two different colors for the two different light directions. Similarly, magnetic dichroism refers to the phenomena that the absorption depends on the polarization (circular or linear) of the beam and the magnetic state of sample [Fig. 1.2(c)].

The magnetic sensitivity and polarization dependence in the scattering and absorption processes can be expressed in the resonant scattering amplitude. The resonant contribution to atomic scattering amplitude for dipole resonances can be written

as [10],

$$(1.1) \quad f(\hat{\epsilon}'^*, \hat{\epsilon}) = f_c(\hat{\epsilon}'^* \cdot \hat{\epsilon}) + i f_m(\hat{\epsilon}'^* \times \hat{\epsilon}) \cdot \hat{m} + f_l(\hat{\epsilon}'^* \cdot \hat{m})(\hat{\epsilon}^* \cdot \hat{m}),$$

where $\hat{\epsilon}$, $\hat{\epsilon}'$ are the polarization vectors of incoming and scattered radiation, and \hat{m} is the local moment direction of the ion. f_c is an anomalous charge scattering amplitude, and f_m , f_l are circular and linear dichroism terms. The circular dichroism term is proportional to the moment, and this term can be isolated by reversing the direction of \hat{m} (or reversing incoming polarization) and by measuring the difference in scattering or absorption. While the circular dichroism term is sensitive to the magnetization components parallel to the beam, the linear dichroism term is sensitive to the transverse components (Fig. 1.3). The magnetic contrast can be measured by monitoring the difference in signal between the two opposite polarizations of the incoming x-ray [Figs. 1.3(b),(d)] or between the two opposite orientations of the sample magnetization [Figs. 1.3(a),(c)].

For ferro- or ferrimagnetic materials, structures are commonly studied with circularly-polarized radiation. In absorption channel, x-ray magnetic circular dichroism results in contrast between parallel and antiparallel alignments of x-ray helicity and sample magnetization [12, 13]. Contrast in diffraction can also be used to study ferro- or ferrimagnetic materials, and this contrast in diffraction is due to charge-magnetic interference scattering. The charge-magnetic interference is sensitive to direction and amplitudes of magnetic moments, as well as chemical structures.

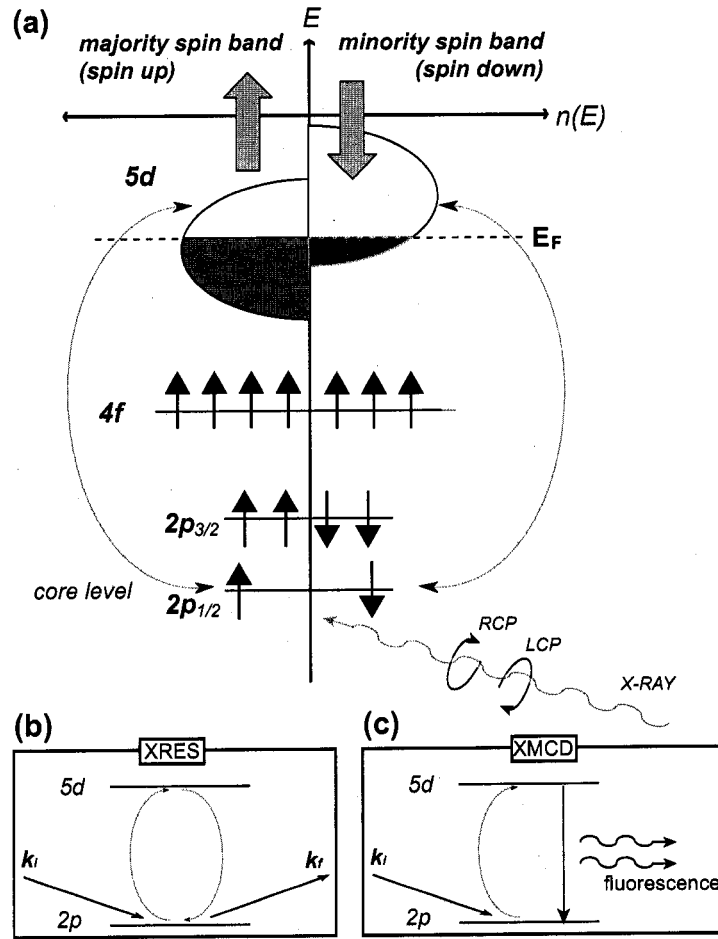


Figure 1.2. (a) Illustration of x-ray resonant scattering and absorption processes used in characterization of ferromagnetic materials. Example is given for dipole transition in Gadolinium. With circularly polarized (CP) incident x rays (right- and left-CP), the transition probabilities to spin-up and spin-down states are different and this difference contributes magnetic sensitivity. For two dimensional systems, such as a ferromagnetic monolayer of Co [13], the out-of-plane density of states can be significantly modified compared with the in-plane density of state. However, this two dimensional effect is not considered in this thesis since only in-plane magnetic properties are studied and the systems studied are typically much thicker than a monolayer. (b) Resonant scattering process (x-ray resonance exchange scattering). (c) Absorption process (x-ray magnetic circular dichroism).

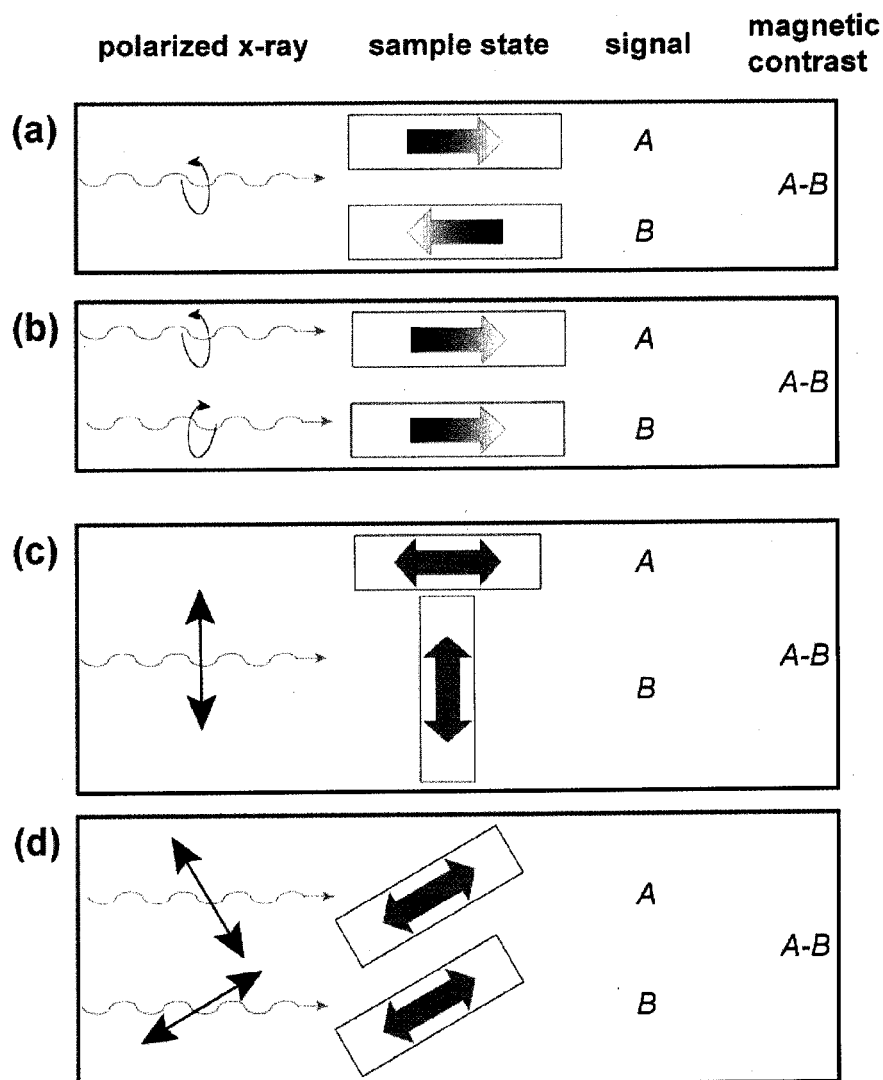


Figure 1.3. Schematic of magnetic dichroic signal measurements. For magnetic circular dichroism measurements, either the sample magnetization can be changed by reversing the applied field direction as in (a) or the polarization of the incoming x-ray can be reversed as in (b). The same method can be used for magnetic linear dichroism measurements as shown in (c)-(d).

CHAPTER 2

Structural and Magnetic Characterization of Antiferromagnetically Coupled Fe/Gd Multilayers

2.1. Background

When rare-earth and transition metals are brought in contact, an antiparallel magnetic coupling arises between the rare-earth $4f$ and $5d$ spin moment and the $3d$ moment of the transition metal. Fe/Gd multilayers is an example with antiferromagnetic coupling at the Fe/Gd interface. Fe and Gd are both ferromagnets with different Curie temperatures (1024 and 293 K, respectively), and the theoretical temperature dependence of the saturation moments of bulk Fe and Gd are shown in Fig. 2.1.

Due to the antiferromagnetic coupling and the different temperature dependence, the Fe/Gd multilayers exhibit complicated magnetic phases, and thus the Fe/Gd multilayers have been a model system for fundamental magnetism studies. Depending on the thickness ratio, temperature, and applied field, the Fe/Ge multilayers can be in different magnetic states. The main driving forces causing the Fe/Gd multilayers to undergo these different magnetic states are the competition between exchange and Zeeman interactions and a finite size effect. In the competition between the exchange and Zeeman interactions, the antiferromagnetically coupled Fe/Gd multilayers can be in Gd-aligned, Fe-aligned, and surface/bulk twisted states [14, 15] as shown in Fig. 2.2.

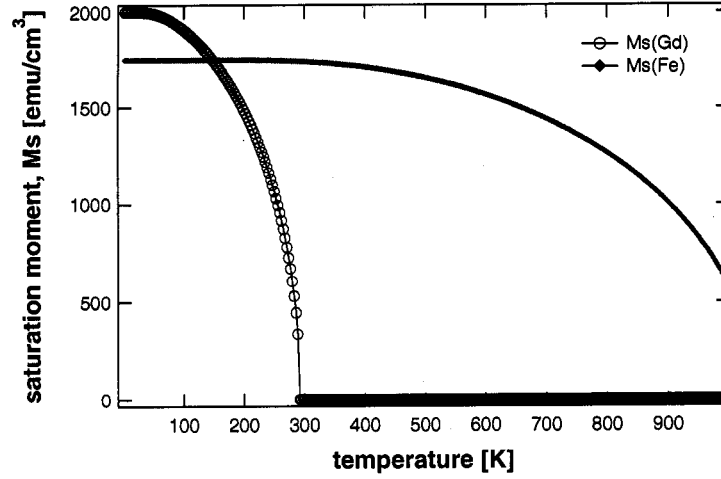


Figure 2.1. Theoretical saturation moments of bulk Gd (open circles) and Fe (solid circles) are plotted as a function of temperature. Magnetic moments per unit volume is plotted at each temperature. The temperature dependence was calculated using the Brillouin function. Up to 300 K, $M_S(\text{Fe})$ goes through a negligible decrease while $M_S(\text{Gd})$ changes significantly.

At low temperatures, the net magnetic moment in the Gd layers is larger than that of the Fe layers so that the Gd layer magnetizations are aligned with the applied field direction while the Fe layer magnetizations are antiparallel to the field. As the temperature is increased, the Gd moment is reduced and reaches a ferrimagnetic compensation point where the net magnetization from the multilayer becomes nearly zero since the Gd and Fe layer magnetizations are equal in magnitude but opposite in direction. Above this compensation temperature, the Fe-aligned state occurs where the Fe layers are magnetized parallel to the field and the Gd layers are antiparallel since the net Fe moment is dominant. Near the compensation point, the magnitudes of the net moments become comparable to each other, and due to strong competition between exchange and Zeeman energy, the twisted state can occur in which the Gd

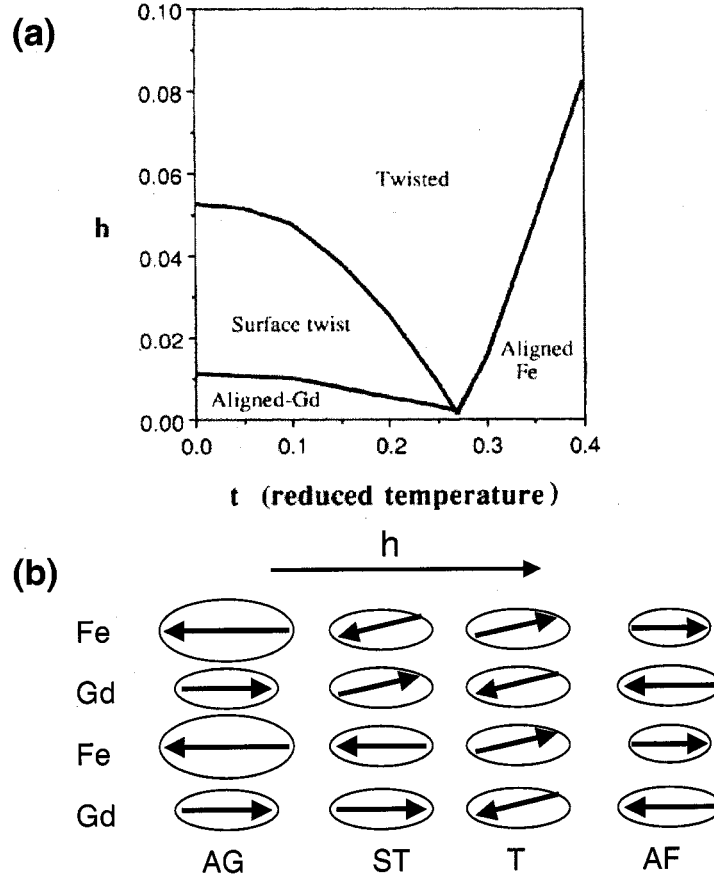


Figure 2.2. (a) Phase diagram of magnetic phases of a Fe/Gd multilayer (from Ref. [18]). h represents the applied field, and $h=0.01$ corresponds to 7.3 kOe, and t represents the reduced temperature $t=T/T_C(\text{Fe})$. (b) Illustrations of each phase. AG: aligned-Gd, ST: surface-twist, T: twisted, and AF: aligned Fe.

and Fe spins are not fully collinear with the field. Depending on where this twisting starts within multilayers, the twisted state can be categorized into bulk twisted and surface twisted states.

In this chapter, the temperature evolution of the magnetization depth profile in the Gd layers of a strongly coupled $[\text{Fe}(15 \text{ \AA})/\text{Gd}(50 \text{ \AA})]_{15}$ multilayer is studied using

x-ray resonant magnetic scattering (XRMS) and x-ray magnetic circular dichroism (XMCD). This multilayer is in the Gd-aligned state throughout the temperatures studied here, and an enhanced magnetic ordering in the Gd layers near the Fe/Gd interface was studied.

In the following chapter, surface twisted spin states of antiferromagnetically coupled $[\text{Fe}(35 \text{ \AA})/\text{Gd}(50 \text{ \AA})]_{15}$ multilayers are investigated using x-ray magnetic circular dichroism (XMCD) technique in a surface-to-bulk sensitive way. Two multilayers with a different top layer (Gd or Fe) are investigated to study a termination effect. These multilayers are in the Gd-aligned state at low temperatures and in the Fe-aligned state in high temperatures. The surface twisted state occurs when the top layer is magnetized opposite to the field direction. As the field is increased, the spins in the top layer begin to rotate toward the field direction, and the rotation of the surface layer magnetization drives the magnetization profile of the multilayer to be inhomogeneous.

2.2. Interfacial Magnetism Study on Antiferromagnetically Coupled Fe/Gd Multilayers using X-ray Resonant Magnetic Scattering

Interfaces play a fundamental role in determining the properties of thin film magnetic devices. Examples include interfacial roughness effects on the giant magnetoresistance (GMR) of spin-valve structures [1], spin transport across interfaces [16], and exchange biasing [2] at the interface between an antiferromagnet and a ferromagnet which can yield enhancement of magnetic ordering temperature due to the proximity

effect [17]. Interfaces and surfaces can also act as nucleation centers for inhomogeneous magnetization depth profiles [6, 18, 19] and can be responsible for chirality in some magnetic structures [20].

Magnetic behavior at surfaces and interfaces often differs from the bulk behavior. For example, on Gd surface layers, an enhanced magnetic ordering temperature and magnetization were observed [21, 22, 23]. On multilayers of Gd and nonmagnetic Y, a reduced Gd-magnetic moment near interfaces was also reported [24, 25]. In Gd/Fe multilayers, the strong coupling between Gd and Fe at the interfaces causes the Gd magnetization to persist above the Curie temperature of bulk Gd. This enhancement of the Gd layer magnetization near the interfaces was observed by spin-polarized Auger-electron spectroscopy [26] and by x-ray resonant techniques [27, 28].

The temperature evolution of the magnetization depth profile in the Gd layers of a strongly coupled $[\text{Gd}(50 \text{ \AA})/\text{Fe}(15 \text{ \AA})]_{15}$ multilayer was studied with a focus on the enhanced magnetic ordering near the Gd/Fe interface. To obtain element-specific magnetic information from the interfacial Gd layers, resonant x-ray techniques were performed, taking an advantage of element-specificity and enhanced magnetic sensitivity.

2.2.1. Experiments

The multilayer used in this study was sputtered in vacuum onto a Si substrate with Nb buffer (100 Å) and cap (30 Å) layers. The multilayer ($[\text{Gd}(50 \text{ \AA})/\text{Fe}(15 \text{ \AA})]_{15}$) has 15 bilayers and an extra Gd layer at the top, i.e., Gd termination at both ends. The sample was grown by Dr. J. S. Jiang from Materials Science Division at Argonne

National Laboratory. The layers were deposited alternatively from individual sources at 1-2 Å/Sec. The base pressure was approximately 2×10^{-8} Torr. The sample was unheated, and the sample holder temperature stayed near room temperature during the growth. Based on previous growth experiences at this condition, it was expected that the layers were polycrystalline and that the Fe layers were likely to be (110) textured. This polycrystallinity of the layers is likely to cause reduced magnetic anisotropy and exchange coupling, compared with single crystal layers. The current study is focused on the overall temperature behavior of the interfacial layers, and even with the reduced anisotropy and exchange coupling effect the overall trend in the temperature dependence is not expected to be significantly different between single- and poly-crystalline multilayer films.

It has been observed in Fe/Gd multilayers, that surface/bulk twisting of magnetization can occur near the ferrimagnetic compensation temperature and that this twisting of magnetization is more pronounced near the interface. For the Fe/Gd sample studied here, the Fe layer thickness was less than the Gd layer thickness so that the compensation point occurs at a higher temperature. SQUID (Superconducting QUantum Interference Device) magnetometry measurements in Figure 2.3 reveal that up to 350 K the multilayer is in the Gd-aligned state at moderate fields, where the Gd magnetization is parallel to the applied field direction and the Fe magnetization is antiparallel. Up to 350 K, Figure 2.3-b does not show a compensation point above which the net moment would increase again. In typical SQUID measurements, the sample moves through a system of superconducting detection coils. As the sample moves, the magnetic moment of the sample induces an electric current in the detection

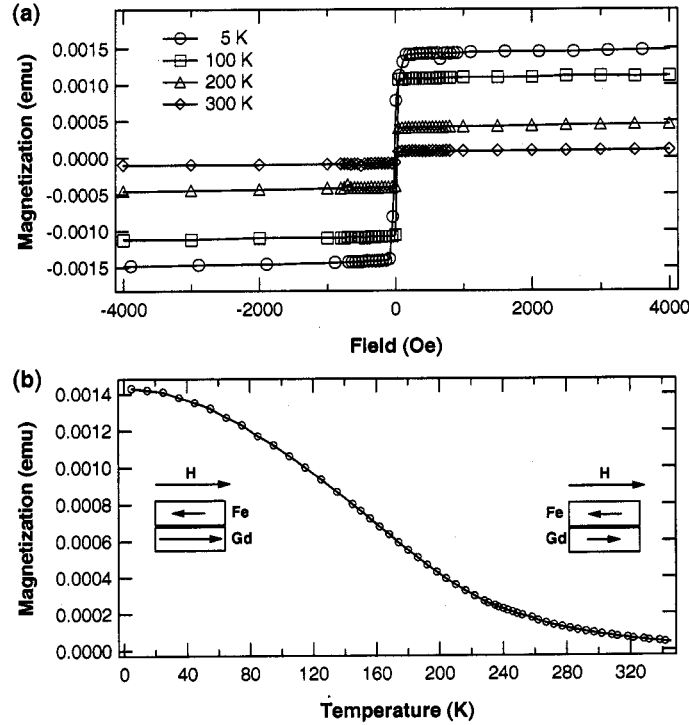


Figure 2.3. SQUID magnetometry measurements on the Fe/Gd multilayer. (a) Magnetization as a function of field at temperatures 20, 100, 200, and 300 K. (b) Magnetization as a function of temperature under 1000 Oe field. The two schematics show the relative orientation of the Gd and Fe spins with respect to the field direction H .

coils, and the output voltage converted from this current is proportional to the sample magnetic moment. For the current Fe/Gd multilayer sample, what is measured by the SQUID is the net moment from the Gd and Fe layer contributions.

X-ray measurements were performed at the 4-ID-D beamline of the Advanced Photon Source at Argonne National Laboratory. The experimental setup shown in Fig. 2.4 is discussed in detail in **Appendix B**. Undulator radiation was passed through double crystal Si (111) monochromator to select photons with a particular

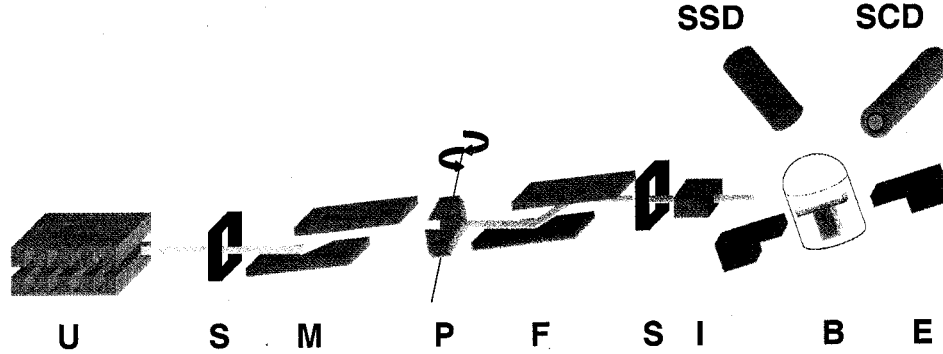


Figure 2.4. Experimental setup at beamline 4ID of APS at ANL. The letters represent: undulator (*U*), slits (*S*), monochromator (*M*), phase retarder (*P*), focusing optics (*F*), ion chamber (*I*), sample inside Be-dome and cryostat (*B*), electromagnet (or permanent magnet) (*E*), solid-state detector (*SSD*), and scintillation detector (*SCD*).

wavelength, and a diamond (111) quarter-wave phase plate operated in Bragg transmission geometry was used to produce the circularly polarized x rays [29]. The 2.1 kOe field of a permanent magnet was applied parallel to the sample surface and in the scattering plane in order to align the Gd moment parallel to the applied field at all temperatures considered. Fig. 2.5 shows the scattering geometry and the applied field direction. The sample and the magnet were placed inside a closed-cycle He refrigerator mounted on a diffractometer.

The XRMS measurements were performed in reflectivity mode. The incident photon energy was tuned to near the Gd L_2 absorption edge (7929 eV), and the reflected intensities were measured as a function of the incident angle while flipping the helicity of the circularly polarized incident x rays. For the reflectivity measurements, I^+ and I^- refer to the reflected intensities for opposite helicities. The XMCD measurements were performed in fluorescence mode by monitoring the intensity of Gd $L\beta$ radiation while alternating the helicity at each energy through the Gd L_2 absorption edge. For

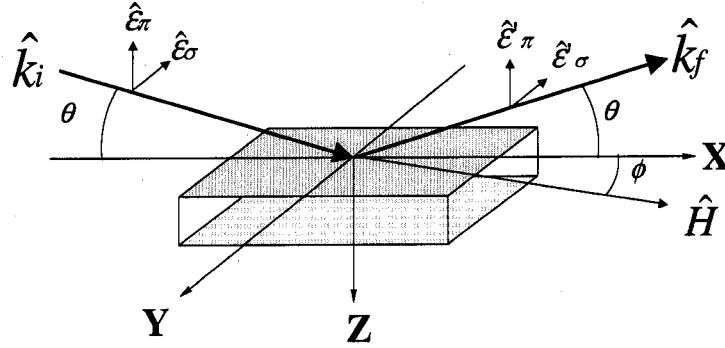


Figure 2.5. Scattering geometry. The magnetic field, \hat{H} , is applied along the X-axis ($\phi = 0, 180^\circ$). The wave vectors of the incident and scattered x rays are \hat{k}_i and \hat{k}_f , respectively, $\hat{\epsilon}'$ and $\hat{\epsilon}$ are the polarization vectors, and θ is the incident and scattered angle.

the XMCD measurements, I^+ and I^- refer to $L\beta$ fluorescence intensities for the two opposite helicities. The incident angle was 10° , for which the x-ray penetration depth is much larger than the multilayer thickness.

Resonant scattering factors of Gd atoms were obtained from absorption measurements through the L_2 absorption edge and through differential Kramers-Kronig transforms (described in detailed in **Appendix C**)

To eliminate any experimental artifacts in the dichroic signals, absorption and scattering measurements were taken with the applied fields parallel and antiparallel to the photon wave vector. At each temperature, two measurements were performed at $\phi = 0$ and 180° where ϕ is defined as the angle between the incoming x-ray beam and the applied field as shown in Fig. 2.5. Figure 2.6 shows absorption measurements across the Gd L_2 absorption edge. The dichroic process leads to complete sign reversal for opposite orientations of \hat{k}_i and \hat{H} . Incomplete reversal is due to systematic errors. These errors were only a few percent in these measurements and were subtracted from

the data before integrating the XMCD signal to obtain average magnetization in Gd layers.

Figure 2.6 shows the XMCD signal at temperatures from 20 to 300 K. The integrated area under these peaks were interpreted as the relative magnetization of Gd layers at each temperature. The sign of XMCD signal does not change between 20 and 300 K, and this indicates that, at least up to 300 K, the Gd/Fe multilayer does not go through a compensation point above which the Gd XMCD signal would reverse its sign.

As mentioned earlier, SQUID measurements indicate that for the moderate field of $H=2.1$ kOe the Gd/Fe multilayer is in the Gd-aligned state (Fig. 2.3). This implies that there is no magnetic component perpendicular to the applied field direction. Since the difference cross section measures the magnetic component in the scattering plane, an aligned state will result in zero difference signal if the field is applied perpendicular to this plane. This is shown in Fig. 2.7, where the sample and magnet assembly were rotated by 90° ($\phi = 90^\circ$), yielding a negligible difference between the scattered intensities for the two helicities.

Figure 2.8 shows x-ray specular reflectivity curves from the $[\text{Gd}(50 \text{ \AA})/\text{Fe}(15 \text{ \AA})]_{15}$ multilayer with the incident photon energy at 7929 eV. The measurements were done at four different temperatures, 20, 100, 200, and 300 K. The charge specular reflectivity curve [Fig. 2.8(a)] was obtained by adding scattering intensities for opposite helicities ($I^+ + I^-$), and the magnetic sensitive reflectivity curves [Figs. 2.8(b)-(e)] were obtained by taking the difference between the two intensities ($I^+ - I^-$). Changes

in the charge specular reflectivity curves at different temperatures were negligible, indicating negligible structural change. However, in the difference signal, significant changes occur due to temperature-dependent changes in the magnetization depth profile of the Gd layers.

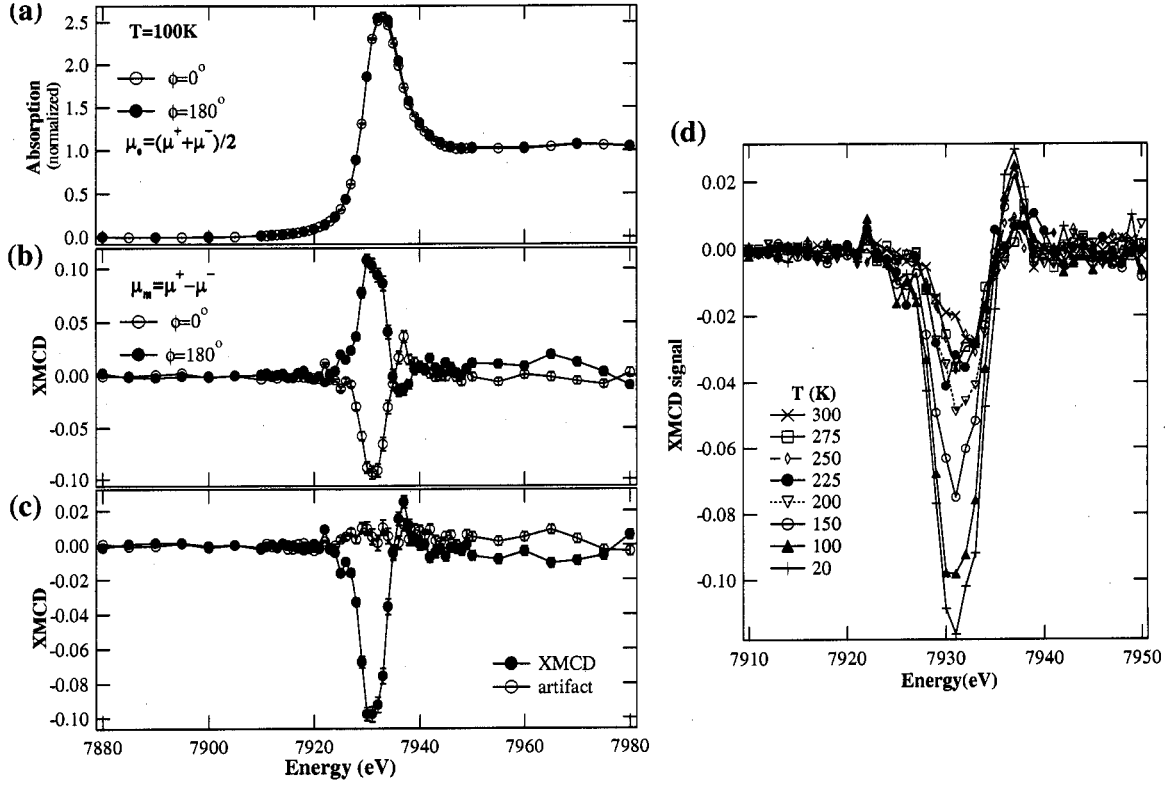


Figure 2.6. The XMCD measurements on the Fe/Gd multilayer for opposite orientations of photon wave vector and sample magnetization. The angle between the incoming beam and the applied field, 2.1 kOe, is ϕ . (a) Polarization-independent absorption coefficients obtained from the sum of fluorescence intensities for opposite helicities of the incoming radiation. (b) The differences in absorption coefficients for opposite x-ray helicities. (c) The XMCD signal is $(\mu_m(\phi = 0^\circ) - \mu_m(\phi = 180^\circ))/2$, and non-magnetic artifact is $(\mu_m(\phi = 0^\circ) + \mu_m(\phi = 180^\circ))/2$. (d) XMCD signals at temperatures between 20 and 300 K with 2.1 kOe applied field. The integrated areas under the curves were used to obtain relative magnetization of the Gd layers at each temperature.

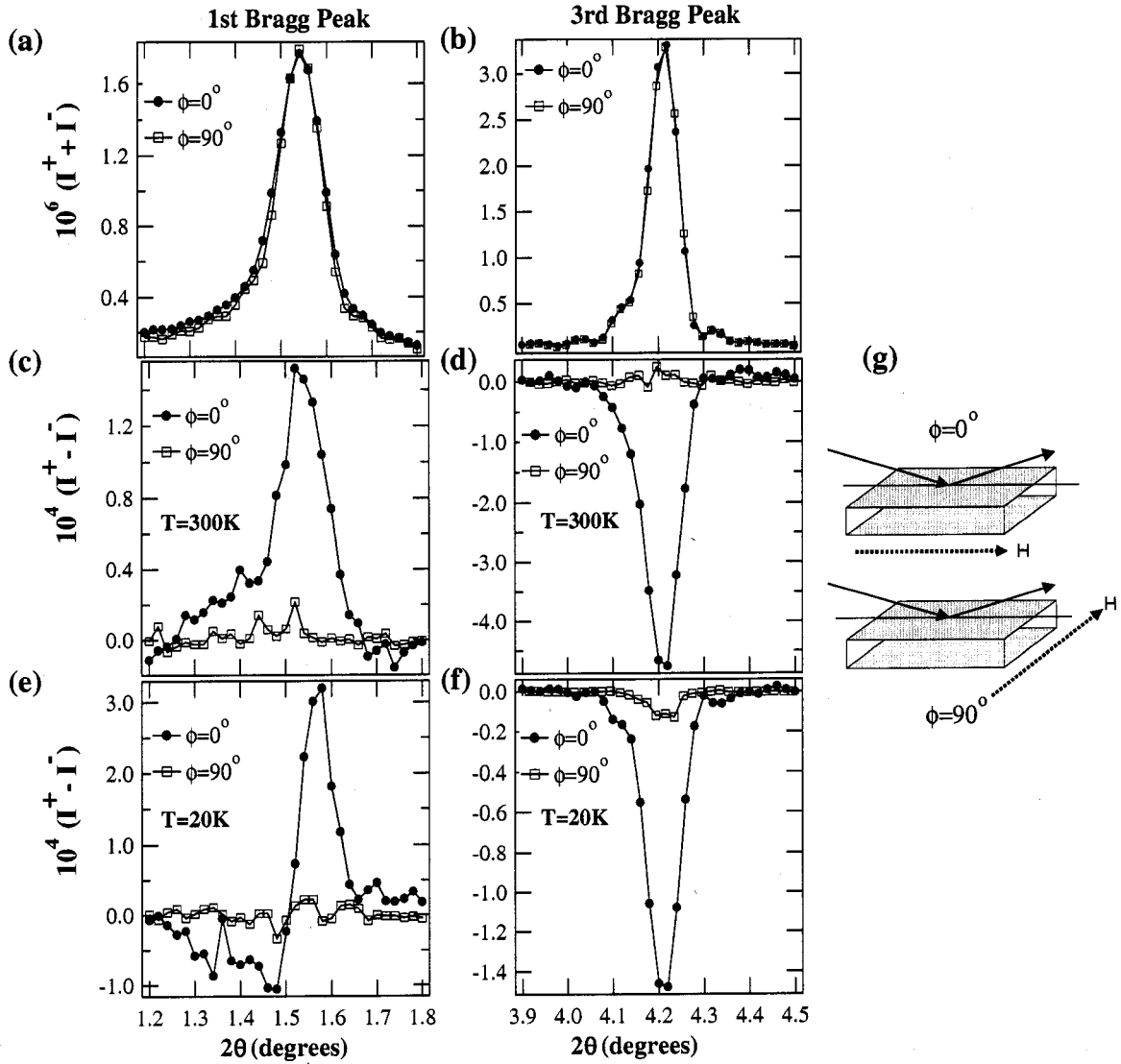


Figure 2.7. The XRMS measurements at $\phi = 0^\circ$ and 90° where ϕ is the angle between the applied field H and the beam direction as shown in (g). (a) and (b) are charge peaks, and (c)-(f) are charge-magnetic peaks for the 1st and 3rd multilayer Bragg peak. (c)-(f) show that there is no magnetization component perpendicular to the applied field direction.

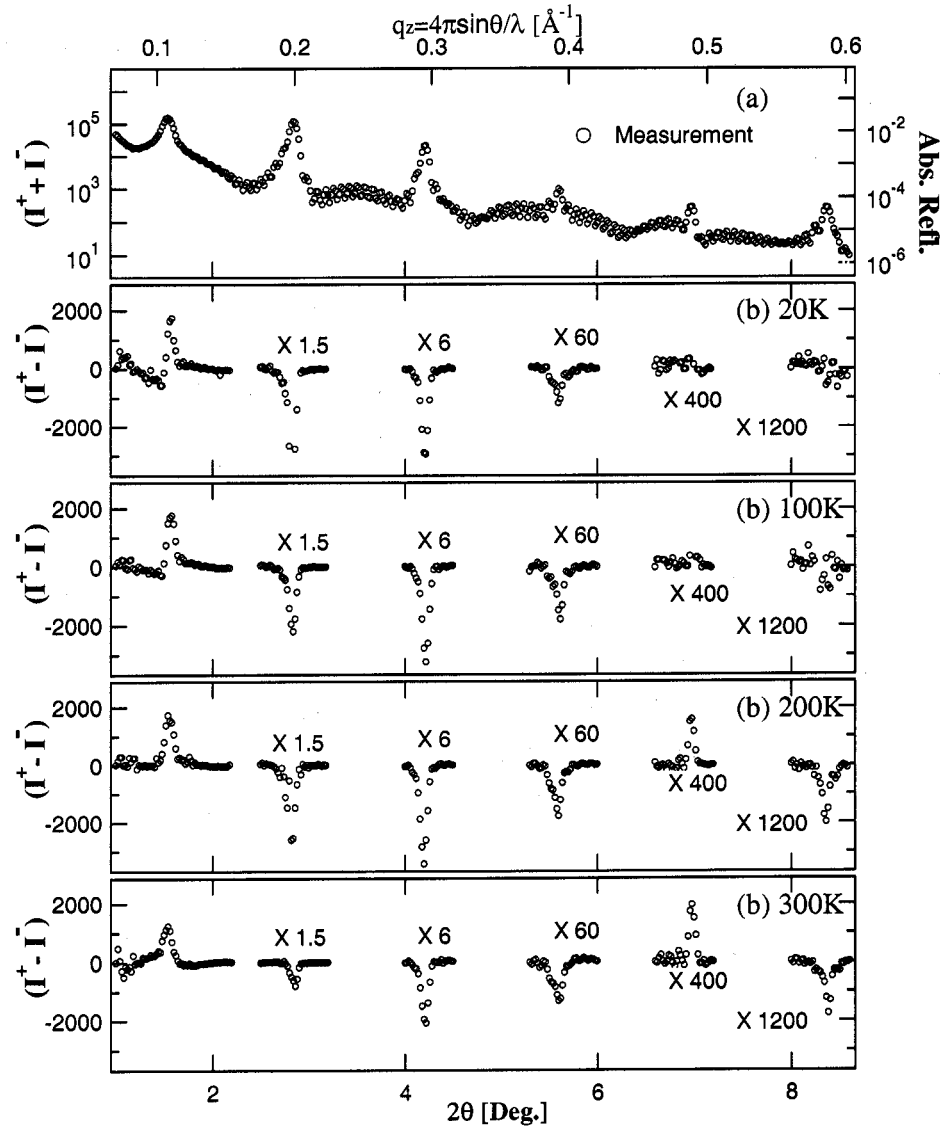


Figure 2.8. Charge-magnetic reflectivity measurements at temperatures 20, 100, 200, and 300 K. The incident x-ray energy was 7929 eV with an applied field of 2.1 kOe. (a) Charge specular reflectivity for the Fe/Gd multilayer at 300 K. (b)-(e) Charge-magnetic reflectivity curves at the indicated temperatures. The numbers above the peaks indicate scaling factors used for clarity. While the charge reflectivity is sensitive to the structural parameters of films, the charge-magnetic reflectivity is related to the structural parameters and the Gd layer magnetic parameters.

2.2.2. Analysis of X-ray Resonant Magnetic Scattering Data

Assuming negligible nonresonant magnetic scattering and using the electric dipole approximation, the resonant elastic scattering length for a Gd ion can be written as [10],

$$(2.1) \quad f = (f_0 + f_e)(\hat{\epsilon}'^* \cdot \hat{\epsilon}) + if_m(\hat{\epsilon}'^* \times \hat{\epsilon}) \cdot \hat{m},$$

where $f_0 = -Zr_e$, r_e is the classical electron radius, f_e and f_m are anomalous charge and magnetic scattering amplitudes, $\hat{\epsilon}$, $\hat{\epsilon}'$ are the polarization vectors of incoming, scattered radiation, \hat{m} is the local moment direction. A linear dichroic term, f_l , is ignored in this expression since f_l is generally much smaller than f_m at lanthanide L edges and since the polarization vectors are nearly perpendicular to \hat{m} for our scattering geometry. The scattering cross section obtained from Eq. 2.1 includes pure charge, pure magnetic, and charge-magnetic interference terms [30].

Since only dipole transitions at the $L_{2,3}$ edges are considered, the magnetization profiles from charge-magnetic specular reflectivity fittings represent the profiles of Gd $5d$ moments. These are assumed to mimic the profiles of their $4f$ counterparts due to the strong ($4f - 5d$) intra-atomic exchange coupling that contributes to the spin polarization of the Gd $5d$ band.

To simplify the calculations, each Gd layer was divided into three sublayers. Equivalence of Gd/Fe and Fe/Gd interfaces was assumed so that the two outer sublayers near the Fe layers have the same magnetization. Charge specular reflectivity curves were fitted with the distorted wave Born approximation (DWBA) [31, 32],

which yields the same calculated reflectivity curves as the ones using Parratt's recursive formalism [33, 34]. In the DWBA, the actual rough surface/interface is treated as a small perturbation from the smooth surface/interface. For small incident angles, the reflectivity calculation based on the DWBA can give better results than the calculations based on the Born approximation. In the Born approximation, multiple scattering and x-ray refraction is not fully accounted, and thus at low incident angles, the calculations based on the Born approximation fail to explain features in x-ray reflectivity.

The fitted structural parameters from the charge specular reflectivity curves were then incorporated into the charge-magnetic specular reflectivity fittings using the DWBA [32]. For the different temperatures, each Gd layer (total 16 Gd layers) was divided into three sublayers. The middle sublayer thickness was a fitting parameter, while that of the equivalent outer sublayer was constrained by the total layer thickness fitted from the charge specular data. Other fitting parameters are the magnetic roughness between the layers and the relative magnetization in the three Gd sublayers. These charge and magnetic parameters were used to calculate the charge and charge-magnetic reflectivity curves using the BA (Born approximation).

The edge-jump normalized (i.e. per atom) Gd XMCD peak signal at 10 K is $\mu_m/\mu_e = 0.051(3)$, in agreement with bulk Gd. In addition to full saturation, this indicates that the Gd magnetic moment is not reduced relative to its bulk value. The experimentally determined value of f_m at 10 K therefore sets the scale for quantitative determination of depth resolved magnetization profiles on an absolute scale. A scaling of f_m was used in modeling the local Gd magnetization at each temperature.

2.2.3. First Born approximation model for calculation of charge-magnetic specular reflectivity

Using the Born approximation, the differential cross section is written:

$$(2.2) \quad \frac{d\sigma}{d\Omega} = |n_e(f_0 + f_e)\hat{\epsilon}'^* \cdot \hat{\epsilon} \int \int \int_{V_{charge}} e^{i\hat{q} \cdot \hat{r}} d^3r + in_e f_m (\hat{\epsilon}'^* \times \hat{\epsilon}) \cdot \hat{m} \int \int \int_{V_{mag}} e^{i\hat{q} \cdot \hat{r}} d^3r|^2,$$

where n_e is the scatterer's number density, and the integrals are over the charge and magnetic volume. After squaring the sum of the charge and magnetic terms, the cross section has a pure charge term, a pure magnetic term, and a charge-magnetic interference term. Only the latter depends on the orientation of magnetization (or helicity). Therefore, the difference in the scattering intensities between the two opposite helicities, $I^+ - I^-$, is due to the charge-magnetic interference contribution only. The charge-magnetic interference term of the scattering cross section includes the products of the charge and magnetic contrasts at the interfaces. Adding charge and magnetic roughnesses at the interfaces, the charge-magnetic cross section for specular reflectivity becomes [28, 30, 31],

$$(2.3) \quad \begin{aligned} \left(\frac{d\sigma}{d\Omega} \right)_{charge-mag} &= \frac{4\pi^2 L_x L_y \delta(q_x) \delta(q_y)}{q_z^2} P_c [\cos 2\theta (\hat{k}_i \cdot \hat{m}) + (\hat{k}_f \cdot \hat{m})] \times \sum_{a,b}^N e^{iq_z(z_a - z_b)} \\ &\quad [\Delta \rho_{e,a}^* \Delta \rho_{m,b} e^{-\frac{q_z^2}{2}(\sigma_{e,a}^2 + \sigma_{m,b}^2)} + \Delta \rho_{e,b} \Delta \rho_{m,a}^* e^{-\frac{q_z^2}{2}(\sigma_{e,b}^2 + \sigma_{m,a}^2)}], \\ \Delta \rho_{e,a}^* &= n_e^{a+1} (f_0 + f_e^*)^{a+1} - n_e^a (f_0 + f_e^*)^a, \\ \Delta \rho_{m,b} &= n_e^{b+1} s_m^{b+1} f_m^{b+1} - n_e^b s_m^b f_m^b. \end{aligned}$$

Here, q_z , θ_{eff} , δ_{eff} , and β_{eff} are defined as

$$\begin{aligned}
 q_z &= \frac{4\pi \sin \theta_{eff}}{\lambda}, \\
 \theta_{eff} &= \sqrt{\theta^2 - 2\delta_{eff} - i2\beta_{eff}}, \\
 \delta_{eff} &= \frac{d_{Fe}}{d_{Fe} + d_{Gd}} \delta_{Fe} + \frac{d_{Gd}}{d_{Fe} + d_{Gd}} \delta_{Gd}, \\
 \beta_{eff} &= \frac{d_{Fe}}{d_{Fe} + d_{Gd}} \beta_{Fe} + \frac{d_{Gd}}{d_{Fe} + d_{Gd}} \beta_{Gd}.
 \end{aligned}
 \tag{2.4}$$

The charge and magnetic density contrasts across interfaces a, b are $\Delta\rho_{e,a}^*$ and $\Delta\rho_{m,b}$, respectively. The degree of circular polarization is P_c ; n_e is the atomic number density; s_m is a scaling factor for the magnetization; $\hat{k}_{i,f}$ are the wave vectors of the incident and scattered radiation. Height fluctuations about the average positions of the charge and magnetic interfaces are assumed to be Gaussian, and thus $\langle [\delta z_{e,m}(x, y)]^2 \rangle = \sigma_{e,m}^2$. Orientational disorder contributions to the magnetic roughness are not explicitly considered, i.e., they are folded into an *effective* magnetic roughness σ_m .

The polarization dependence in Eq. 2.3 was calculated using the matrix formalism of Blume and Gibbs [35] for the case where no polarization analysis of the scattered beam is performed. It involves taking traces over matrix products of the form $\langle \hat{\epsilon}'^* \cdot \hat{\epsilon} \rangle \rho \langle [(\hat{\epsilon}'^* \times \hat{\epsilon}) \cdot \hat{m}]^* \rangle$, where ρ is the (2×2) density matrix of a beam with circular polarization in the (σ, π) basis. From Eq. 2.3, the charge-magnetic cross section is only sensitive to the component of the magnetization density in the scattering plane $[(\hat{k}_i \cdot \hat{m}), (\hat{k}_f \cdot \hat{m}) \text{ terms}]$.

2.2.4. Distorted-Wave Born approximation model for fitting of charge-magnetic specular reflectivity

The DWBA calculations for the magnetic reflectivity are based on the formalism developed recently by Lee *et al.* for magnetic multilayers with rough interfaces [32]. This formalism includes structural and magnetic interfaces to represent actual interfaces. Nevot-Croce formula for specular reflectivity was generalized for the case of a single rough magnetic interface using self-consistent method. This single rough magnetic interface was then generalized for multiple interfaces.

For specular condition, the differential cross section for scattering by the rough surface can be written as [31, 32],

$$(2.5) \quad \frac{d\sigma}{d\Omega} = \frac{1}{16\pi^2} |\langle T^{fi} \rangle|^2.$$

$T^{fi} = \langle \hat{k}_f, \nu | T | \hat{k}_i, \mu \rangle$ is the scattering matrix element. $k_{i,f}$ are wavevectors of incident and scattered radiation, and μ and ν are polarization vectors. The scattering matrix element is expressed as,

$$(2.6) \quad \begin{aligned} \langle k_f, \nu | T | k_i, \mu \rangle &= k_0^2 \langle -k_f^t, \nu | \chi^{(0)} | E_\mu^i(r) \rangle \\ &+ k_0^2 \langle -k_f^t, \nu | \Delta^e | k_i, \mu \rangle + k_0^2 \langle -k_f^t, \nu | \Delta^m | k_i, \mu \rangle, \end{aligned}$$

$E_\mu^i(r)$ is the incident wave and $|-k_f^t, \nu\rangle$ is the time-reversed function corresponding to a wave incident on the interface. $\chi^{(0)}$ denotes an ideal system with a smooth interface, and Δ^e and Δ^m are structural and magnetic perturbations on $\chi^{(0)}$ due to non-ideal rough interface.

For specular condition, Eq. 2.6 can be rewritten as

$$(2.7) \quad \mathbf{R}_{\nu\mu} = \mathbf{R}_{\nu\mu}^{(0)} + \mathbf{U}_{\nu\mu} + \sum_{\lambda} \mathbf{V}_{\nu\lambda} \mathbf{R}_{\lambda\mu}^{(0)}.$$

$R_{\nu\mu}, R_{\nu\mu}^{(0)}$ are reflection coefficients for rough and smooth ideal interface, respectively. $R_{\nu\mu}^{(0)}$ can be expressed in terms of 2×2 matrices using the polarization bases for the incident and reflected waves. For the waves in the nonmagnetic medium, the polarization base is given by $(\hat{e}_\sigma, \hat{e}_\pi)$. In the magnetic resonant medium, the polarization base is expressed by two circular polarizations, $(\hat{e}^{(1)}, \hat{e}^{(2)})$, where $\hat{e}^{(1)} = \hat{e}_\sigma + i\hat{e}_\pi$ and $\hat{e}^{(2)} = \hat{e}_\sigma - i\hat{e}_\pi$. $U, V_{\nu\mu}$ are the correlation terms due to the roughness in the reflection coefficients containing structural and magnetic roughness (σ_c and σ_m). A self-consistent matrix can be written as,

$$(2.8) \quad \mathbf{R} = \mathbf{R}^{(0)} + \mathbf{U} + \mathbf{V}\mathbf{R},$$

where its solution is,

$$(2.9) \quad \mathbf{R} = (1 - \mathbf{V})^{-1}(\mathbf{R}^{(0)} + \mathbf{U}).$$

Reflection coefficients are expressed as three different functions for nonmagnetic-magnetic (nonresonant-resonant), magnetic-nonmagnetic (resonant-nonresonant), and magnetic-magnetic interfaces (resonant-resonant). These reflectivity coefficients can be expressed as a function of the refracted angles u_\pm , the wave vector k_o , the roughness $\sigma_{e,m}$, and the dielectric susceptibility. Here, u_\pm are non-trivial solutions of Maxwell's wave equation for $M \parallel X$ (the magnetization vector is aligned along the sample surface in the scattering plane). u_\pm are refracted angles inside media, defined as, $u_\pm = \sqrt{\theta_i^2 + \chi_1 \pm B'}$. In a resonant magnetic medium the dielectric susceptibility is

a tensor. χ_1 and B' are a diagonal and off-diagonal terms in the dielectric susceptibility of a resonant magnetic medium for the case $M \parallel X$. The off-diagonal term is related to x-ray magneto-optics effects. For a non-resonant medium, the off-diagonal term B' is vanishing, and thus $u_+ = u_- = \sqrt{\theta_i^2 + \chi_1}$. For the interface between two non-magnetic layers, the reflection coefficient is reduced to the familiar Nevot-Croce form [33, 34],

$$(2.10) \quad R = R^{(0)} e^{2|k_z||k_z^i|\sigma_c^2}.$$

The reflection coefficients for the other two cases can be obtained with similar approach, and they are described in detail elsewhere [32].

The reflection coefficients \mathbf{R} are for the single interface. For multiple interfaces, this approach can be generalized by calculating a reflection coefficient for each interface. The specular reflectivity from magnetic multilayer can be calculated using the (2×2) recursive matrix algorithm for scattering matrices of individual layers. This recursion relation was originally developed by Stepanov and Sinha [36] for resonant specular reflectivity from magnetic multilayers with smooth interfaces, but here the recursion relation was modified to include interface roughness [32].

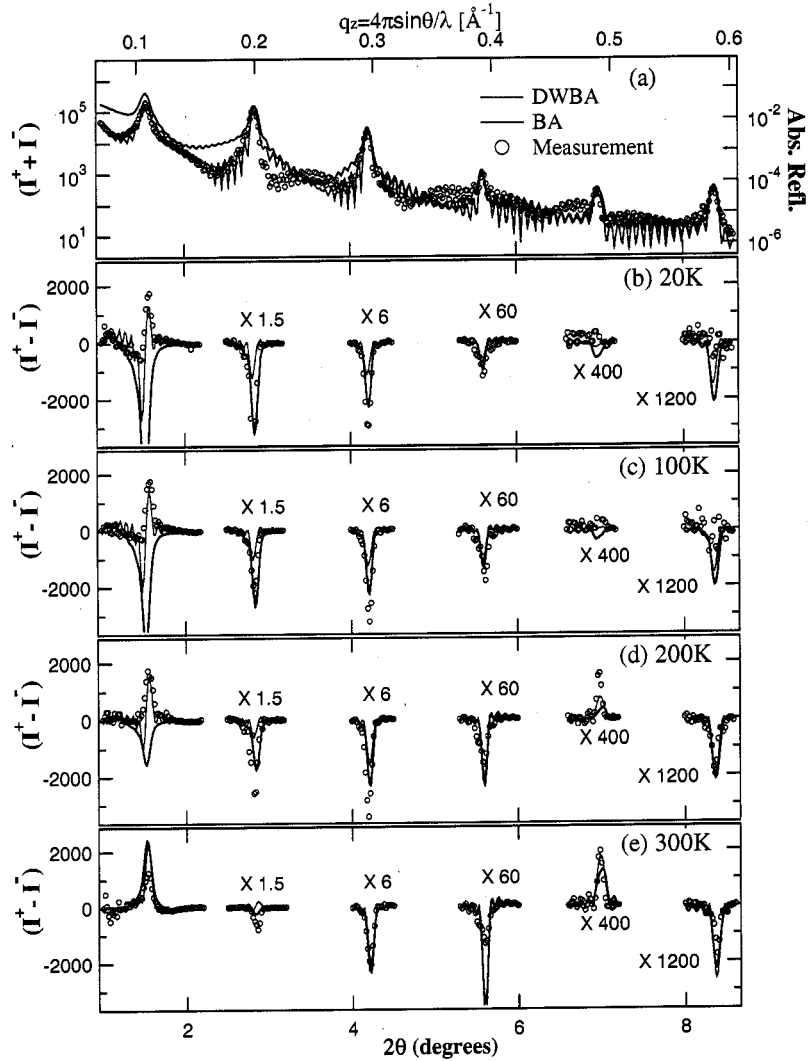


Figure 2.9. Specular reflectivity measurements from Fig. 2.8(symbols), the DWBA calculation (red lines), the BA calculation (blue lines). The incident x-ray energy was 7929 eV with an applied field of 2.1 kOe. The measured reflectivity curves were fitted with the DWBA theory, and the parameters obtained from this fitting were used for the BA calculation. (a) Charge specular reflectivity for Gd/Fe multilayer at 300 K. The root-mean-squared roughness of the Gd/Fe chemical interface was 3.0 ± 1.1 Å, and the densities of Gd and Fe layers were 93% of their bulk values. (b)-(e) Charge-magnetic reflectivity curves at the indicated temperatures with fits using the BA and DWBA theories.

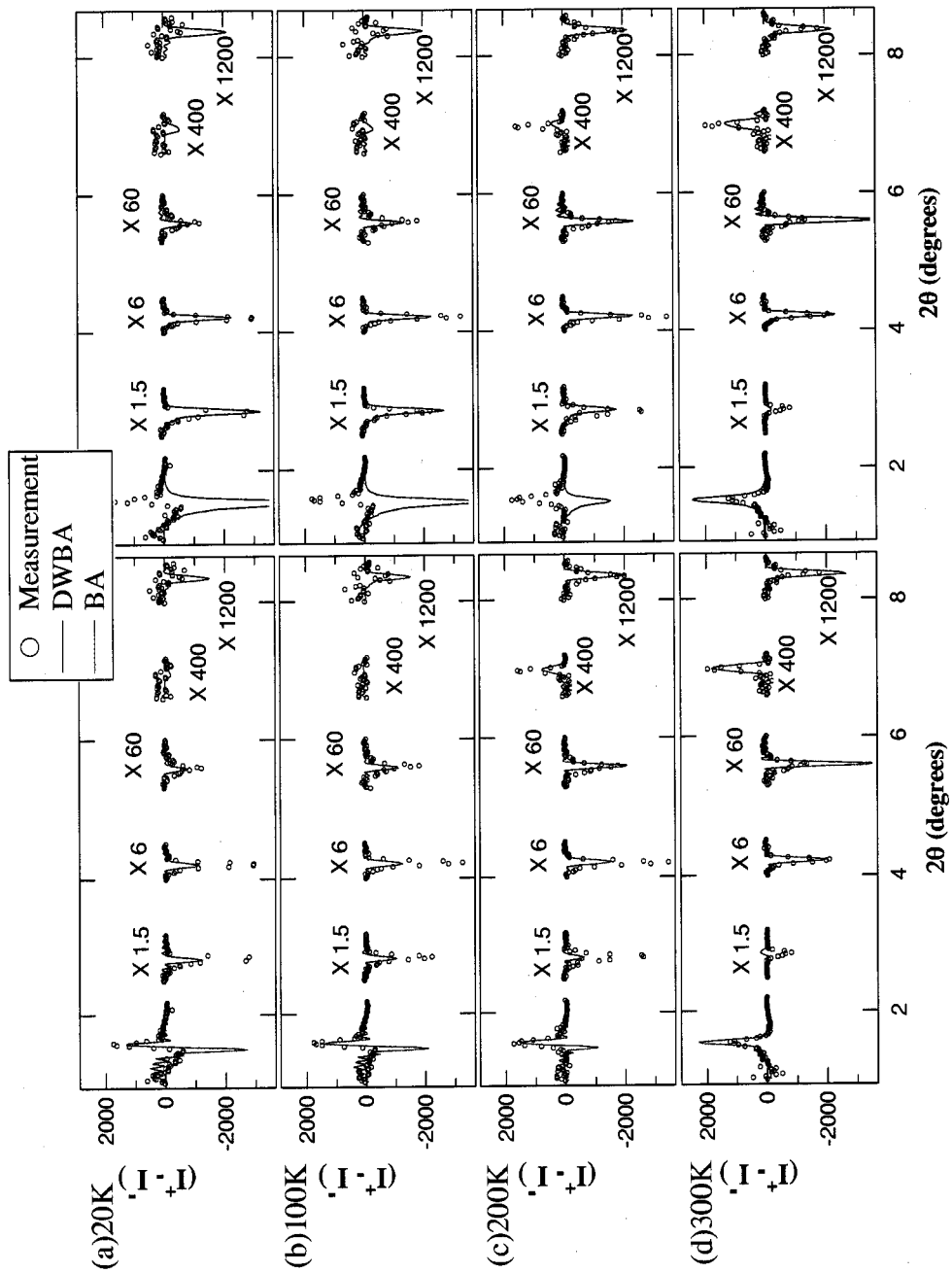


Figure 2.10. Charge-magnetic reflectivity curves in Fig. 2.9 are re-plotted, and the BA and DWBA calculations are plotted separately. The symbols represent the measured data, the red curves (in left panels) are from the DWBA calculation, and the blue curves (in right panels) are from the BA calculation.

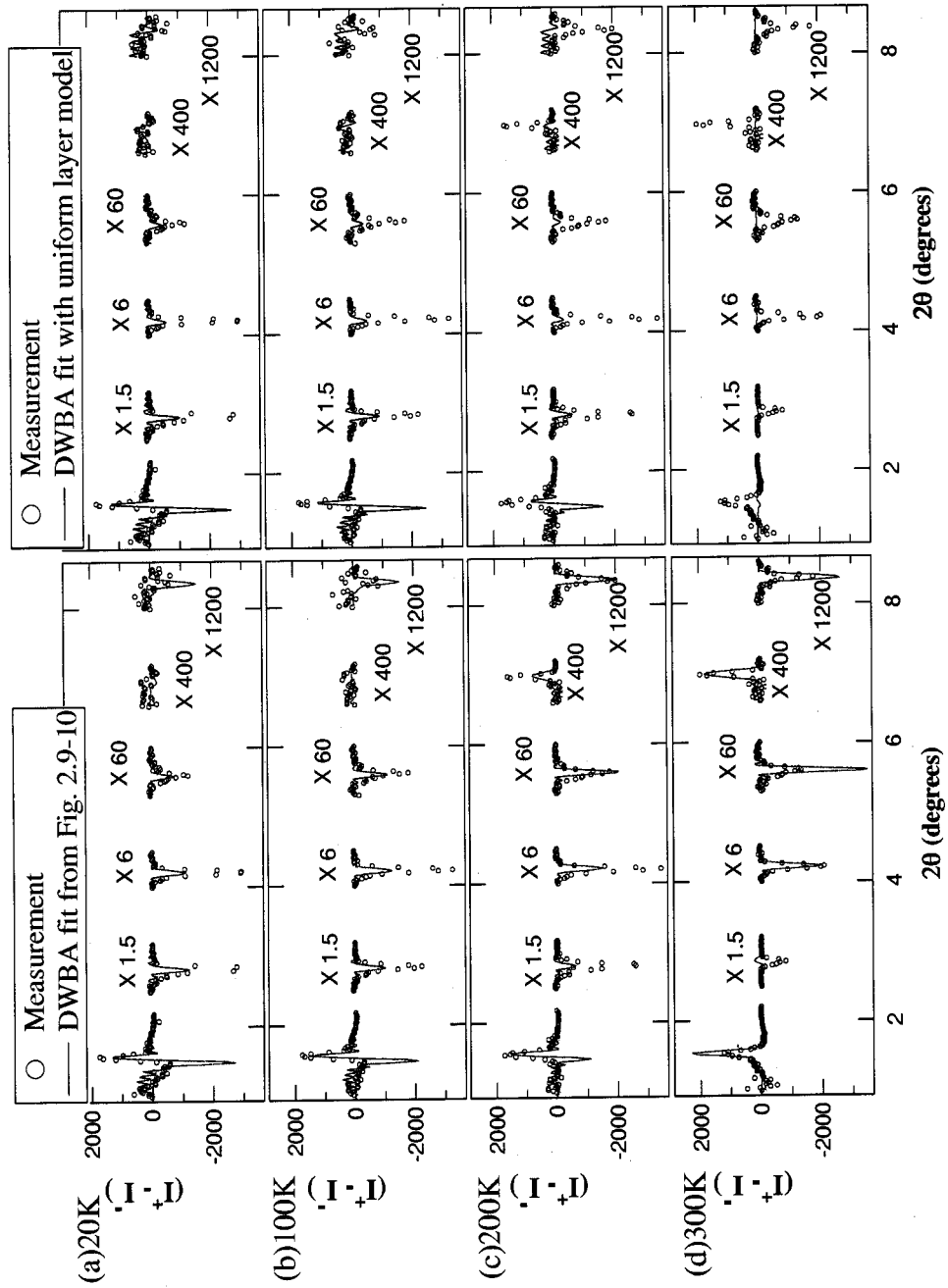


Figure 2.11. DWBA fitting results with a uniform Gd-layer magnetization model (blue lines, right) was compared with the DWBA fitting results (red lines, left) from Fig. 2.9.

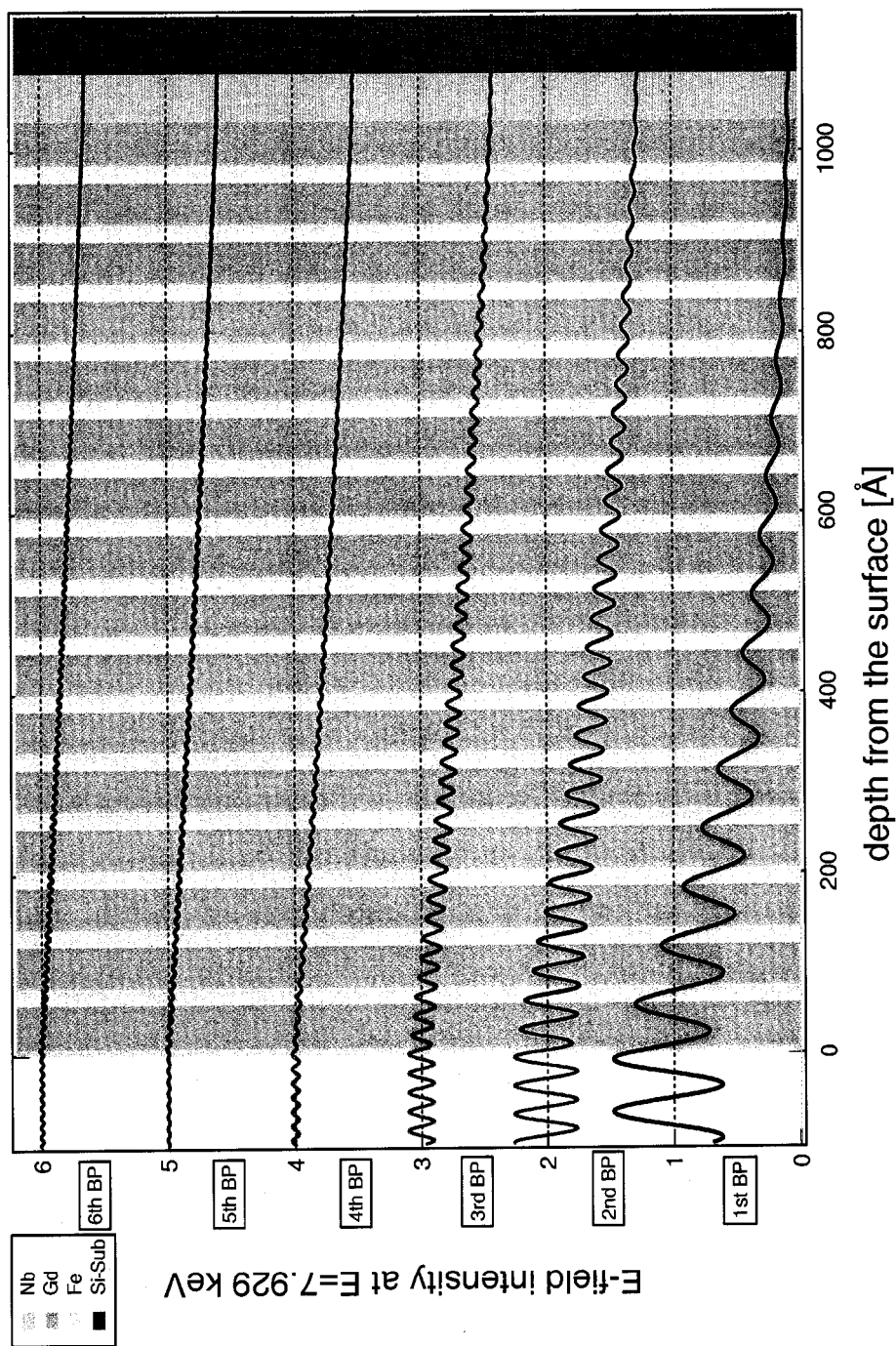


Figure 2.12. Calculated electric field intensity profiles as a function of depth are shown for the six Bragg peak angles. The incident x-ray energy was 7929 eV, and the incident angles were 0.77, 1.42, 2.11, 2.8, 3.49, and 4.18° for the 1st, 2nd, 3rd, 4th, 5th, and 6th Bragg peaks, respectively. For clarity, the e-field intensity profiles for the 2nd-6th Bragg peaks were shifted up by 1 to 5.

2.3. Discussion

The parameters obtained by fitting the measured reflectivity curves with the DWBA model are shown in Table 2.1. The fitted charge-magnetic specular curves simulated with these parameters are shown as red lines in Figs. 2.9(b)-(e). It is assumed that there is no charge roughness between the Gd-sublayers ($\sigma_{e,\text{GdGd}} = 0$).

With these parameters, the charge-magnetic specular reflectivity curves were calculated using the BA model [Figs. 2.9(b)-(e) blue lines]. The two calculated results are replotted separately in Fig. 2.10. Overall, both models are in agreement with the data except near the first multilayer Bragg peak (Fig. 2.10). In the low q_z region near the critical angle for total external reflection, the BA model does not explain the charge-magnetic specular reflectivity accurately because it neglects multiple scattering and only approximates the x-ray refraction, both of which are strong near total external reflection. The DWBA is a dynamical calculation taking account of the multiple scattering and thus gives a better description in this region, as also found in non-magnetic cases [31]. Since both the BA and the DWBA models give consistent magnetic parameters in the fits, however, the BA model can be used provided a large q_z range of data is available. An extended q_z range is a prerequisite for refinements of magnetization density profiles with high spatial resolution. Furthermore, since the BA model is a kinematical calculation wherein each interface acts as an independent scatterer, it is conceptually more straightforward than the DWBA model, which needs a recursive approach to treat multiple interfaces.

Table 2.1. Parameters derived from fits to the charge-magnetic specular reflectivity data for the indicated temperatures. The relative magnetization of the Gd sublayers are M_{int} and M_{mid} . For all temperatures, $\sigma_{e,GdFe} = 3.0 \pm 1.1$ Å, $\sigma_{e,GdGd} = 0$ Å. The fitted thickness of Gd-sublayers adjacent to the Fe layers is $d_{int} = 3.94 \pm 0.09$ Å at all temperatures.

$T(K)$	M_{int}	M_{mid}	$\sigma_{m,GdFe}$ (Å)	$\sigma_{m,GdGd}$ (Å)
300	1.00 ± 0.12	0.00 ± 0.00	4.21 ± 0.23	3.18 ± 0.06
200	1.00 ± 0.13	0.46 ± 0.04	3.89 ± 0.14	3.26 ± 0.13
100	1.00 ± 0.13	0.74 ± 0.04	3.76 ± 0.09	3.61 ± 0.23
20	1.00 ± 0.13	0.91 ± 0.03	3.66 ± 0.06	3.44 ± 0.31

As shown in Table I, the Gd moment of the interfacial regions are enhanced relative to that of the interior regions. While the Gd moment of the interior regions decreases as the temperature increases, the enhanced moment in the interfacial regions does not change. The width of these magnetized region is 3.94 ± 0.09 Å, almost independent of temperature. The fitted magnetic roughnesses ($\sigma_{m,GdFe}$, $\sigma_{m,GdGd}$) do not change noticeably as the temperature changes. However, it can be noted that the magnetic roughness between Fe and Gd layers ($\sigma_{m,GdFe}$) slightly increases as the temperature increases.

The experimental data and fitting results shown in Fig. 2.9 show reasonably good agreement. However, in some areas the fitting results could not reproduce the features in the experimental data. The discrepancy between the experimental and fitting results may be due to possible systemic errors in the experimental data, errors in the DWBA and BA theory, and the model dependency of the calculated curves.

For comparison, the DWBA fitting results with the model used above is shown together with the results with a uniform Gd-layer magnetization model in Fig. 2.11.

In this uniform magnetization model, the Gd magnetization was kept uniform across each Gd layer. The uniform magnetization model works well for 20 K. At this temperature, the magnetization contrast between the interfacial and interior Gd layers is small so that the uniform layer magnetization model is as good as the three layer model used above. However, as the temperature is increased the DWBA fitting results based on this model fails to reproduce the features in the difference ($I^+ - I^-$) peaks.

In Fig. 2.9, it is noticeable that the experimental data and fitting results do not match well for the low order Bragg peaks. This may be due to the fact that at low incident angles the near surface layer contribution is over-emphasized compared with the contribution from the interior. The electric field intensity profiles inside the multilayer were calculated as shown in Fig. 2.12. These electric field intensity profiles were calculated based on the recursive relation calculation with reflection and transmission coefficients [33, 37]. The electric field intensity profiles show that for the low order Bragg peaks, the near surface Gd layer contribution is much larger than the contributions of the layers below. The model used in the DWBA fitting assumes that all 15 Gd layers in this multilayer film are equivalent, and if the near surface Gd layers are slightly different from the rest of the Gd layers, the contribution from this difference would be over-emphasized at the low angles in the reflectivity measurements.

The theoretical Gd magnetization profile at each temperature was calculated for the sample structure within a mean-field approach considering nearest-neighbor interactions only [14, 38]. The mean-field calculation results were provided by Professor

R. E. Camley from Department of Physics, University of Colorado. The results of these mean-field calculations at each temperature are shown in Fig. 2.13 along with the profiles derived from fits to the charge-magnetic specular reflectivity curves. The key parameters used in the mean-field calculation are: applied field = 2.1 kOe; 20 Gd atomic layers per unit cell; 8 Fe atomic layers per unit cell; 15 unit cells with Gd on the outside at both ends; Gd moment = $7.0 \mu_B$; Fe moment = $2.2 \mu_B$. An initial estimate of the exchange-coupling parameters is made from the bulk Curie temperatures of Fe and Gd, where $T_C = J_{\text{tot}} S(S+1)/3$. The exchange constant J_{tot} is expressed in Kelvins and is a measure of the total effective exchange field acting on an individual spin; it includes in-plane contributions as well as exchange fields from one plane acting on a neighboring plane. In the final calculations, the values for the exchange constants are $J_{\text{Gd/Fe}} = -200$ K; $J_{\text{Gd}} = 13.7$ K and $J_{\text{Fe}} = 529.3$ K. It is expected that the exchange coupling within a plane will be the same as that between planes, so $J_{\text{tot-Fe}} = 3 J_{\text{Fe}}$, for example. To obtain the best agreement with the data, a reduction factor of 0.9 was introduced for the Gd moments, and a reduction factor of 0.93 was included for the Fe moments.

As shown in Fig. 2.13 the profiles obtained from the mean-field calculation and those from the fitted parameters are consistent. Both theoretical and experimental results show that the Gd layers near Fe are fully magnetized at all temperatures considered while the magnetization in the interior decreases with increasing temperature.

One possible origin of the enhanced Gd magnetization (as observed in the experiments and in the mean-field calculations) is proximity to magnetized Fe ($T_C=1024$ K) to which the Gd magnetization couples by a strong antiferromagnetic exchange

interaction. This interlayer exchange interaction is short-ranged, and therefore the enhancement in the Gd magnetization is limited to the region near the Gd/Fe interfaces. This scenario is supported by the results of mean-field calculations, which yield very similar magnetization profiles by assuming strong interlayer antiferromagnetic coupling across sharp interfaces. It is known that, in rare-earth (RE) transition-metal (TM) intermetallics, a strong coupling between TM and RE ions exists through strong hybridization between the RE $5d$ and TM $3d$ bands. Since Fe has a much higher ordering temperature than Gd, it induces spin polarization in the Gd $5d$ band through hybridization. The Gd $5d$ bands play a role in mediating the indirect coupling between localized Gd $4f$ moments [39, 40].

It can also be argued that the enhancement in the Gd magnetization near Gd/Fe interfaces is due to alloying between Gd and Fe. To address this question, off-specular, longitudinal, diffuse scattering measurements were performed on the same Gd/Fe sample. Since specular reflectivity yields a density profile averaged over a illuminated lateral area, specular reflectivity measurements cannot distinguish roughness effect from interdiffusion effect. However, these two effects can be distinguished by measuring diffuse scattering. A rough interface would cause off-specular diffuse scattering, while a laterally homogenous interface with interdiffusion would not give rise to diffuse scattering. The off-specular diffuse scattering data shown in Fig. 2.14(a) shows Bragg peaks corresponding to the Gd/Fe bilayer period, and these strong diffuse peaks indicates that the roughnesses at the Gd/Fe interfaces are conformal and correlated in the normal direction [41]. This supports the presence of well-defined interfaces with

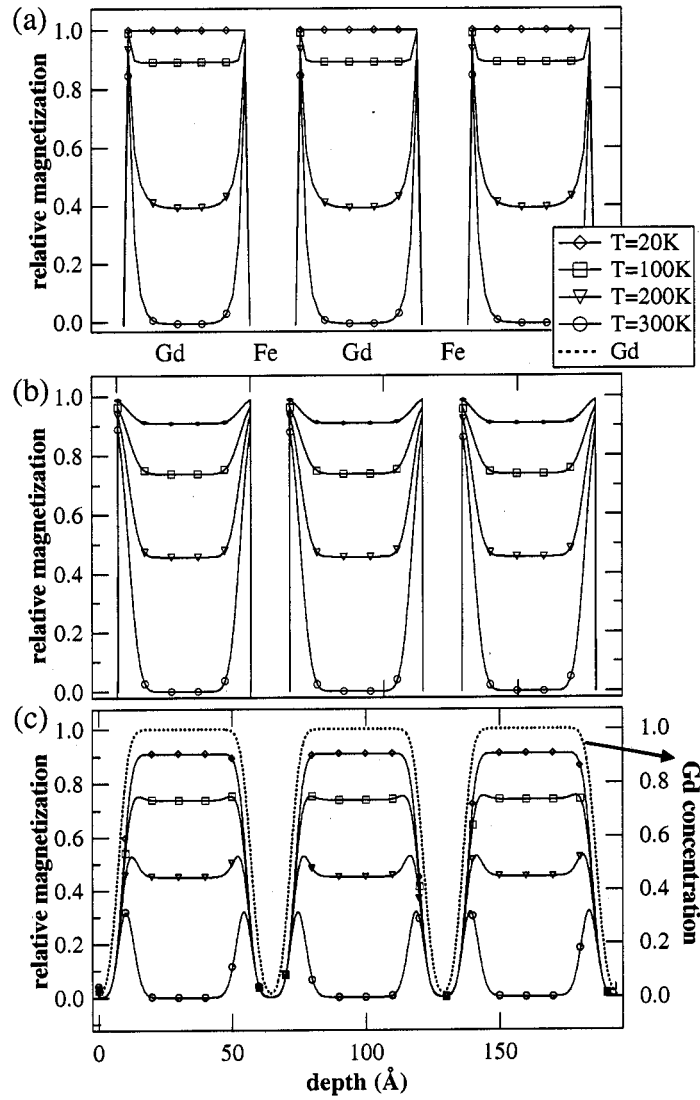


Figure 2.13. (a) Gd magnetization profile obtained by mean field calculations, assuming perfect interfaces. (b) Gd magnetization profile used in fitting the charge-magnetic reflectivity data at the different temperatures. For comparison with (a), charge and magnetic roughnesses between Gd/Fe layers are not included in this plot. (c) As in (b), but with structural and magnetic roughness included. The dash line represents Gd concentration obtained from charge reflectivity fitting. Each profile shows the relative magnetization within the Gd layer, which is the product of Gd concentration and the average magnetic moment within each Gd sublayer [24].

pure roughnesses [Fig. 2.14(b)] as opposed to the structureless interfaces expected from pure intermixing [Fig. 2.14(c)].

The question remains whether structural roughness is needed to drive the interface magnetic ordering of Gd. Our theoretical calculations, which yield similar enhancements by assuming sharp interfaces, indicate that the strong antiferromagnetic coupling is the key ingredient. However, the spatial extent of the magnetized region is likely to be determined by a combination of structural roughness and the range of antiferromagnetic interaction between Gd and Fe. In this particular case, since the *rms* roughness is comparable to the extent of the magnetized Gd layer, the roughness sets an upper limit for the extent of such antiferromagnetic coupling.

Further evidence for the absence of significant intermixing comes from the XMCD measurements. We do not observe significant changes in XMCD line shape between 20 and 300 K, despite the latter probing the enhanced interfacial region only. Significant changes in local chemical environment associated with strong intermixing would have resulted in an altered line shape, which is not observed.

The integrated area under the fitted magnetization profile (from the fitted parameters in Table I) is calculated to obtain the average magnetization of Gd layers for each temperature. In Fig. 2.15, these values are compared with similar averages obtained from the result of the mean-field calculations and with those obtained by integrating the XMCD data in Fig. 2.6(d). The figure shows that the mean-field calculation and the integrated moment calculation from the reflectivity fittings are in agreement. Assuming that each Gd layer has interfacial and interior regions with the same saturation magnetization M_0 but different T_C values, the average magnetization

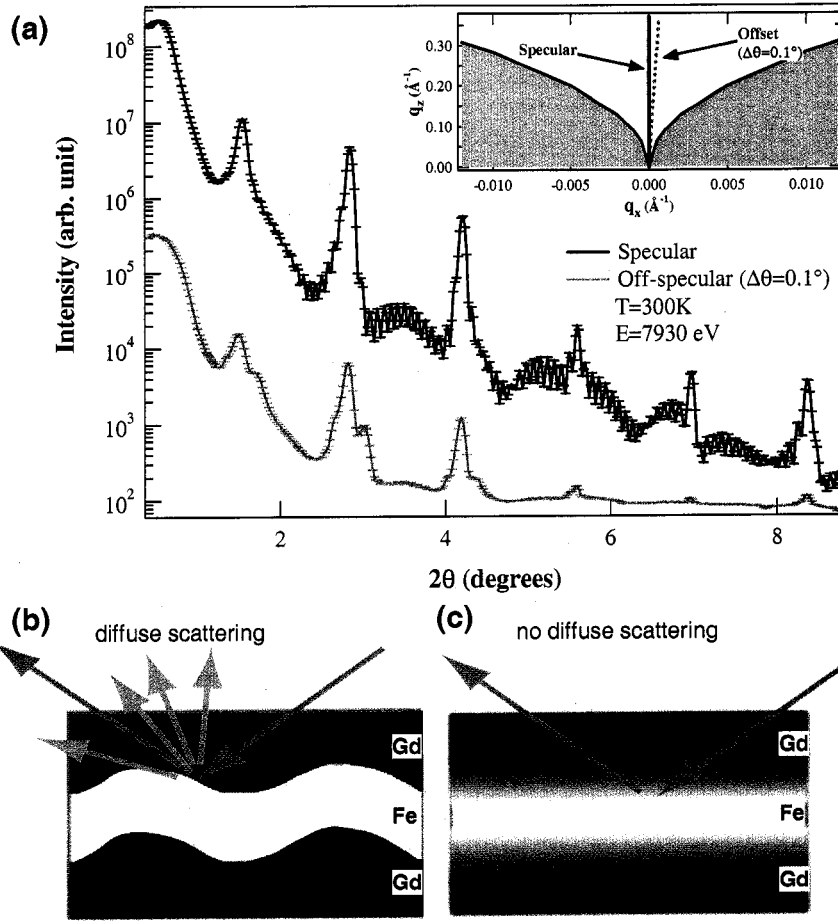


Figure 2.14. (a) Specular reflectivity (dark) and off-specular reflectivity (gray) measurements. The offset angle is 0.1° for the off-specular measurement. The inset shows the wave-vector transfer in the reciprocal plane. (b) interfaces with roughness. (c) interfaces with intermixing.

from the XMCD data was fitted using a superposition of two different $M(T)$ curves corresponding to interior and near-interface Gd volumes. The following equation was used to describe the temperature-dependent magnetization:[42]

$$(2.11) \quad \frac{M(T)}{M_0} = \int_{T_C} \left(\frac{T_C - T}{T_C} \right)^\beta \theta(T_C - T) \cdot \rho(T_C) dT_C,$$

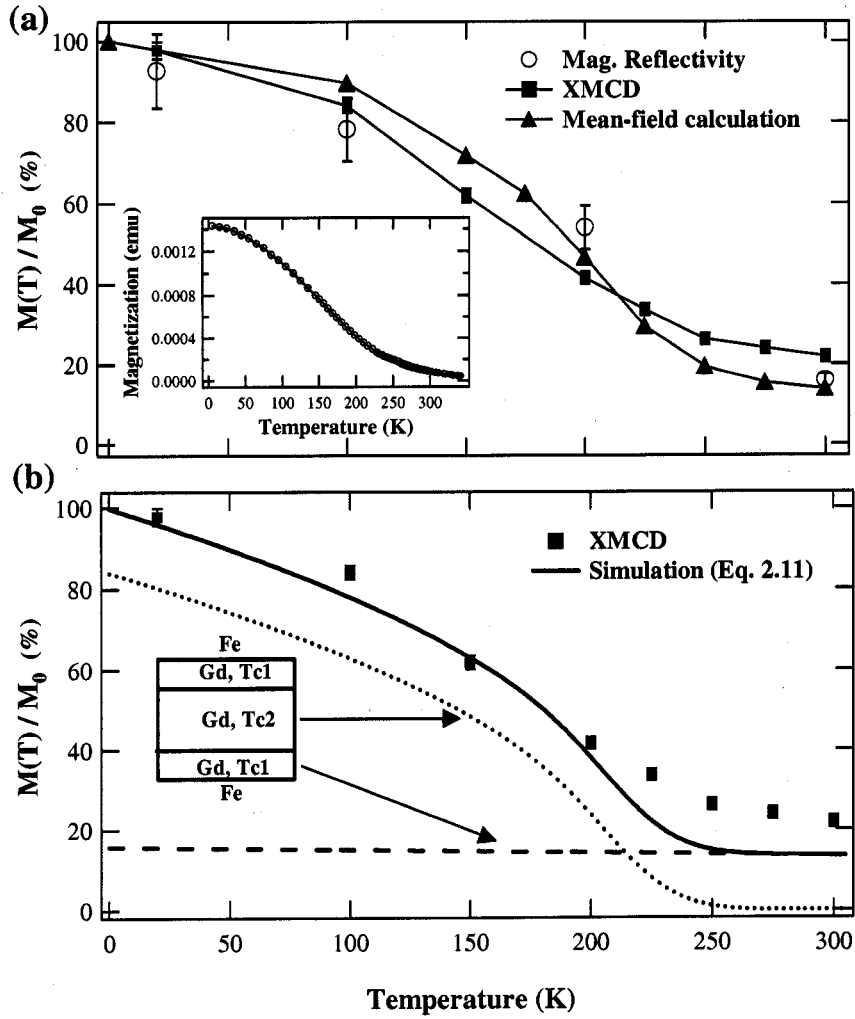


Figure 2.15. Average Gd layer magnetization at each temperature. (a) XMCD result (rectangles) is obtained from temperature-dependent XMCD measurements by integrating the area under Gd L_2 absorption edge [Fig. 2.6(d)]. Mean field calculation result (triangles) and charge-magnetic reflectivity result (circles) are calculated by integrating the area under Gd magnetization profile curves [Figs. 2.13(a),(b) respectively]. The inset shows SQUID magnetometry result on the Gd/Fe multilayer (Fig. 2.3). Lines are guide to the eye. (b) Magnetization for the interfacial (dashed line) and middle (dotted line) regions were calculated using Eq. 2.11 with different T_C values. The two values were added with the thickness ratio included (solid line).

where $\theta(x)$ is the Heavyside function, and $\rho(T_C)$ is a Gaussian distribution function with a 20 K distribution width in order to account for disorder in the sputtered sample. The XMCD average magnetization result was reproduced best with $\beta = 0.47 \pm 0.09$. The contributions from the two regions were added as $M(T) = (2r)M_{int}(T) + (1 - 2r)M_{bulk}(T)$, where r is the ratio of interfacial region thickness over total Gd layer thickness ($r=0.079$) obtained from XRMS measurements. The T_C value of the middle region is estimated to be 220 K that is lower than that for bulk Gd ($T_C \approx 293$ K), consistent with other reports [27]. The T_C value of the interfacial regions is estimated to be 1050 K that is comparable to the T_C value of bulk Fe. It should be noted that the moment of the interfacial regions are almost independent of temperature between 20 and 300 K, and this is consistent with the results from the reflectivity fitting (Table I). The large $J_{Gd/Fe}$ compared to J_{Gd} effectively decouples the Gd interfacial and bulk regions giving justification to the two-component system modeling in Fig. 2.15. Further support for this uncoupled behavior is found in the work of Binder and Hohenberg [43], where decoupling of surface and bulk magnetic orderings is found when $J_{surface} \geq 1.6J_{bulk}$.

2.4. Conclusion

The temperature evolution of the magnetization in the Gd layers of a strongly coupled Gd/Fe multilayer was studied using element-specific magnetization probes. Spatially resolved magnetization profiles were obtained from fits of XRMS reflectivity data using dynamic (DWBA) calculation of the asymmetry in the reflected intensity of opposite helicities of incoming circularly polarized x rays. With the fitted parameters,

kinematic calculation (BA) was then used to calculate the asymmetry in the reflected intensity. Both approximations include the effect of chemical and magnetic roughness on the scattered intensity, allowing for quantitative determination of magnetization profiles. The refined profiles are inhomogeneous throughout the 20-300 K temperature interval, wherein the magnitude (but not the direction) of the Gd magnetization varies throughout the Gd layer thickness. Different origins for the enhanced Gd magnetic ordering near Fe were discussed, including strong antiferromagnetic coupling at Gd/Fe interfaces, intermixing, and the role of roughness. Theoretical calculations within a mean-field approach show that a strong interlayer antiferromagnetic coupling at Gd/Fe interfaces can account for the observed profiles even in the absence of chemical roughness. While the enhanced ordering of Gd at Gd/Fe interfaces does not require roughness, these enhanced regions can extend past the very short range of antiferromagnetic interactions in the presence of roughness.

CHAPTER 3

Spin reorientations and surface effects in Fe/Gd magnetic films

3.1. Background

Magnetic multilayers have been the topic of intense research recently as they exhibit a myriad of novel magnetic phenomena arising from direct exchange across interfaces or indirect layer coupling through nominally non-magnetic spacers. One of the most well known phenomena due to the magnetic coupling is exchange bias between ferromagnetic-antiferromagnetic layers, which causes a field shift in the hysteresis loop of ferromagnetic layers [2]. In some antiferromagnetic multilayers, the competition between the exchange, Zeeman, and anisotropy interactions can lead to a spin flop transition, resulting in a canting of sublattice magnetization [5]. In these antiferromagnets, surface effects play an important role on the spin flop transitions. The surface spin flop transition was observed to occur at lower fields than the bulk transition. In addition, the surface spin flop depends on the number of layers [6].

Fe/Gd multilayers have antiferromagnetic coupling at the Fe/Gd interface, and at temperatures where the Gd and Fe layer net moments are comparable to each other, the Fe/Gd multilayers exhibit a canting of sublattice magnetization similar to the spin flop in antiferromagnetic multilayers. Ferromagnetic Fe and Gd have different Curie temperatures (1024 and 293 K, respectively), as shown in the previous chapter

(Fig. 2.1). As temperature changes, the system goes through different magnetic states due to the antiferromagnetic coupling and the different temperature dependence.

Due to the competition between exchange and Zeeman interactions, the antiferromagnetically coupled Fe/Gd multilayers can be in Gd-aligned, Fe-aligned, and surface/bulk twisted states [14, 15] as illustrated in Fig. 3.1. The Gd-aligned state occurs at low temperatures, the twisted states occur near the ferrimagnetic compensation point T_{Comp} , and the Fe-aligned state occurs above T_{Comp} . Unlike in the Fe- and Gd-aligned states, in the twisted states the Gd and Fe spins are not fully collinear with the field. Depending on where this twisting starts within multilayers, the twisted states can be categorized into either a bulk twisted or a surface twisted state. While away from T_{Comp} , the magnetic phase diagram is determined by the competition between Zeeman and exchange energies, right near T_{Comp} Zeeman energy contributions are reduced and the magnetic ground state becomes more susceptible to other small interactions.

Twisted state of spins in Fe/Gd multilayers have been observed with magnetoresistive measurements [16], polarized neutron scattering [44, 45], x-ray resonant magnetic scattering [27], MOKE [45], and magnetometry measurements [16, 27, 44, 45, 46]. Direct experimental observation of the surface twisted state is not trivial due to the difficulty in probing surface and bulk states in the same measurements.

Previously the surface twisted state on a Fe-terminated Fe/Gd multilayer was reported by using x-ray magnetic circular dichroism (XMCD) technique with varying penetration depth in order to separate surface and bulk magnetic contributions [19]. The surface twisted state was observed on the Fe-terminated sample but not on a

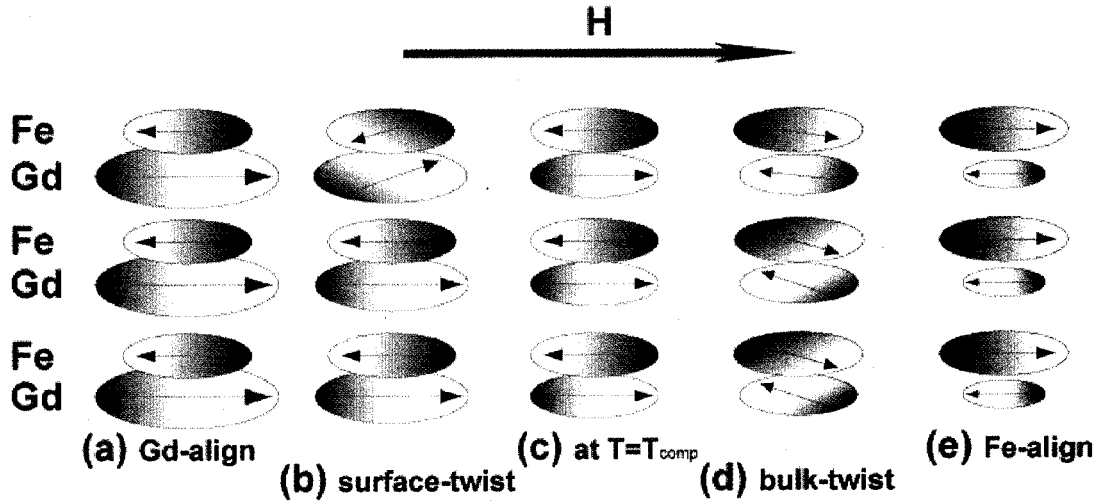


Figure 3.1. Possible magnetic states of a ferrimagnetic (Fe/Gd) multilayer depending on temperature, applied field, and layer thickness. The relative size of ellipses and arrows represents the relative magnetic moment of each layer.

Gd-terminated sample. The nucleation of an inhomogeneous surface magnetic state was observed at a temperature below the compensation point. As the temperature approached the compensation point, the inhomogeneous magnetic state penetrated more into bulk, and temperatures far below and above the compensation point, the magnetic state became homogenous. However, due to the choice of capping layer (Nb), x-ray penetration through the Nb layer became problematic for the Fe surface measurement, and Fe surface magnetic state could not be measured. Here, similar Fe/Gd multilayers with a different capping layer (Al) are studied so that both of Fe and Gd surface layers can be probed along with bulk layers. Two multilayers with different termination layers are studied in this paper since the transition from the Gd- and Fe-aligned to the twisted state can be modified by the termination layers (surface and bottom) of the stacking. XMCD measurements were done with different

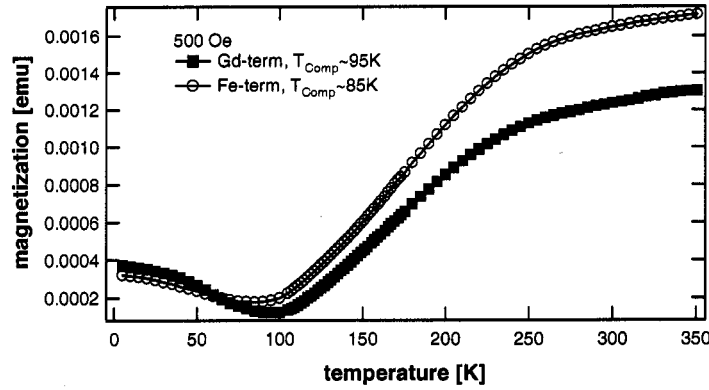


Figure 3.2. SQUID measurements on the Fe-terminated and Gd-terminated [Fe/Gd] multilayers. The compensation temperatures are 85 and 95 K, respectively, for the Fe- and Gd-terminated samples. The applied field is 500 Oe.

incident angles of x rays to probe different film depths, and experimental results were confirmed by micromagnetic simulation results.

3.2. Measurement of inhomogeneous magnetization using surface-to-bulk sensitive XMCD

3.2.1. Experiments

Two multilayer films that were studied were prepared in vacuum by sputtering Fe and Gd onto a Si substrate with Al buffer (100 Å) and cap (50 Å) layers. A Fe-terminated multilayer sample has Fe layer at top and bottom, ([Fe(35 Å)/Gd(50 Å)]₁₅/Fe(35 Å)), and a Gd-terminated multilayer has Gd layer at top and bottom, ([Gd(50 Å)/Fe(35 Å)]₁₅/Gd(50 Å)).

SQUID measurements were performed as a function of temperature (Fig. 3.2). In contrast to the sample studied in the previous Chapter (Fig. 2.3), the samples here

exhibit minima between 10~350 K in SQUID measurements. The minima in Fig. 3.2 correspond to compensation temperatures where the net magnetization becomes close to zero since Gd and Fe magnetization become equal in magnitude but opposite in direction. The Fe-terminated sample has one less Gd layer than the Gd-terminated does, and thus the compensation temperature is lower for the Fe-terminated than for the Gd-terminated.

X-ray measurements were performed at the 4-ID-D beamline of the Advanced Photon Source at Argonne National Laboratory. For XMCD measurements, a diamond (111) quarter-wave plate operated in Bragg transmission geometry was used to produce the circularly polarized x-rays. The sample was placed inside a closed-cycle He refrigerator mounted on a diffractometer. An electromagnet was mounted externally to the cryostat to apply a magnetic field parallel to the sample surface and in the scattering plane (described in detail in **Appendix B**).

X-ray reflectivity measurements were performed on the Fe- and Gd-terminated multilayers in order to determine structural parameters for micromagnetic simulations. For each multilayer, the reflectivity measurements were conducted at a non-resonant (7 keV) and a resonant energy (7.245 keV, near Gd L_3 edge), as shown in Fig. 3.3. The contrast in optical constants between Gd and Fe is low at a non-resonant energy as shown in Tab. 3.1, and thus the reflectivity measurements were repeated at a resonant energy where the contrast becomes larger due to an enhanced sensitivity to resonant atoms. The atomic scattering factors of Gd near Gd L_3 edge were obtained through Kramers-Kronig transform [47] of Gd absorption spectra measured on the samples. From these atomic scattering factors of Gd, the optical constants of

Table 3.1. Optical constants of Gd and Fe at a non-resonant (7.0 keV) and a resonant energy of Gd (7.245 keV).

$E(\text{keV})$	$\delta(\text{Gd})$	$\delta(\text{Fe})$	$\beta(\text{Gd})$	$\beta(\text{Fe})$
7.000	2.2705×10^{-5}	2.6287×10^{-5}	1.8296×10^{-6}	5.9163×10^{-7}
7.245	1.5077×10^{-5}	2.5057×10^{-5}	7.872×10^{-6}	4.1865×10^{-6}

Table 3.2. Parameters from the X-ray reflectivity fits for the measured reflectivity on the two multilayers. t , ρ , and σ each represents the layer thickness, density relative to its bulk value, and interface roughness, respectively.

Fe-Term		Gd-Term	
$t(\text{Fe})$	$40.38 \pm 0.31 \text{ \AA}$	$t(\text{Fe})$	$39.96 \pm 0.14 \text{ \AA}$
$t(\text{Gd})$	$45.31 \pm 0.31 \text{ \AA}$	$t(\text{Gd})$	$45.64 \pm 0.14 \text{ \AA}$
$\rho(\text{Fe})$	1.06 ± 0.01	$\rho(\text{Fe})$	1.07 ± 0.01
$\rho(\text{Gd})$	1.11 ± 0.01	$\rho(\text{Gd})$	0.93 ± 0.01
σ_{AlFe}	$3.452 \pm 0.04 \text{ \AA}$	σ_{AlGd}	$7.22 \pm 0.31 \text{ \AA}$
σ_{FeGd}	$8.06 \pm 0.22 \text{ \AA}$	σ_{FeGd}	$5.23 \pm 0.17 \text{ \AA}$
σ_{GdFe}	$4.81 \pm 0.06 \text{ \AA}$	σ_{GdFe}	$3.95 \pm 0.06 \text{ \AA}$

Gd at the L_3 resonant energy was calculated as described in **Appendix C**. Other non-resonant optical constants are obtained from the tabulated values [48].

For each multilayer, the two reflectivity curves measured at two different energies were fitted simultaneously with one set of parameters using Parratt's recursive formula for x-ray reflectivity [33, 34]. X-ray reflectivity theory with Parratt's recursive is described in detail in **Appendix A**. The parameters from the x-ray reflectivity fitting are shown in Tab. 3.2. The x-ray reflectivity fitting confirmed that the fitted parameters did not significantly deviate from the nominal structural parameters ($[\text{Fe}(35 \text{ \AA})/\text{Gd}(50 \text{ \AA})]_{15}/\text{Fe}(35 \text{ \AA}), [\text{Gd}(50 \text{ \AA})/\text{Fe}(35 \text{ \AA})]_{15}/\text{Gd}(50 \text{ \AA})$), and therefore the nominal parameters were later used in micromagnetic simulations.

To study the magnetization of Gd and Fe layers separately, element-specific hysteresis measurements were performed by recording XMCD signals at the Fe K edge and Gd L_3 edge as a function of the applied field. The XMCD measurements were performed in fluorescence geometry. A cylindrically bent Laue analyzer crystal [49] was placed in front of a fluorescence detector in order to remove undesired scatter and fluorescence background. The term *XMCD signal* is defined as the asymmetry ratio, $(I^+ - I^-)/(I^+ + I^-)$ where $I^{+,-}$ are the fluorescence intensities for the two opposite helicities of the incoming x-ray. XMCD-hysteresis loops obtained at the Fe(Gd) resonant energy are directly related to the Fe(Gd) layer magnetization. For each multilayer, the Fe-layer XMCD-hysteresis loops were measured with x-ray energy at 7.112 keV (Fe K edge) and the Gd-layer XMCD-hysteresis loops at 7.247 keV (Gd L_3 edge). The selected energies are where the maximum magnetic circular dichroic effects were observed across the absorption edges as shown in Fig. 3.4. The sample was cooled down to 10 K with zero field, and the XMCD-hysteresis loop measurements were performed at the temperatures ranging from 10 to 250 K. The spin to orbital magnetic moments ratio was assumed to be not changing at different temperatures, and thus the measured XMCD signal is directly proportional to the magnetic moment of Fe(Gd) along the x-ray beam direction.

For surface-vs-bulk layer sensitivity, XMCD-hysteresis measurements were conducted at two different x-ray incident angles. At each energy, the first set of measurements were performed at a grazing incident angle ($\theta = 0.355^\circ$), and the second set was performed at a high incident angle ($\theta = 5^\circ$). At the high angle, the incoming x rays penetrate through the entire layers, and thus the measurements serves as a probe

of the bulk magnetic properties. At the low angle, the x rays would penetrate only the near surface layers and thus serve as a “surface” sensitive magnetization probe.

Figure 3.5 represents the electric field intensity profiles inside the multilayers at two incident x-ray energies, $E=7.112$ and 7.247 keV. The electric field intensity profiles were calculated based on the Parratt’s recursive relation calculation with reflection and transmission coefficients [33, 37] with experimentally obtained optical constants (δ , β). The atomic scattering factors of Gd and Fe were obtained from absorption measurements, and these experimentally obtained atomic scattering factors were converted into the optical constants (described in **Appendix C**). From this calculation, the attenuation length is less than 1.5 bilayers at the incident angle, $\theta \sim 0.355^\circ$, for all cases considered here (two energies and two samples). From Fig. 3.5, the integrated electric field intensity for each layer can be calculated, and the integrated intensity from the first Fe(Gd) layer was 3.84(5.56) times larger than that from the second Fe(Gd) layer. Based on this calculation, it is concluded that the measured Gd L - and Fe K -fluorescence radiation at $\theta=0.355^\circ$ is mainly from the first Fe/Gd (or Gd/Fe) bilayer. At the two resonant energies, the critical angles $\theta_C(\text{Fe})$ and $\theta_C(\text{Gd})$ were compared with the incident angle $\theta=0.355^\circ$ in Tab. 3.3. With incident energy $E=7.112$ keV, $\theta_C(\text{Fe})=0.335^\circ$ and $\theta_C(\text{Gd})=0.374^\circ$ so that $\theta_C(\text{Fe}) < \theta < \theta_C(\text{Gd})$. However, with $E=7.247$ keV, $\theta_C(\text{Fe})=0.406^\circ$ and $\theta_C(\text{Gd})=0.306^\circ$ so that $\theta_C(\text{Gd}) < \theta < \theta_C(\text{Fe})$.

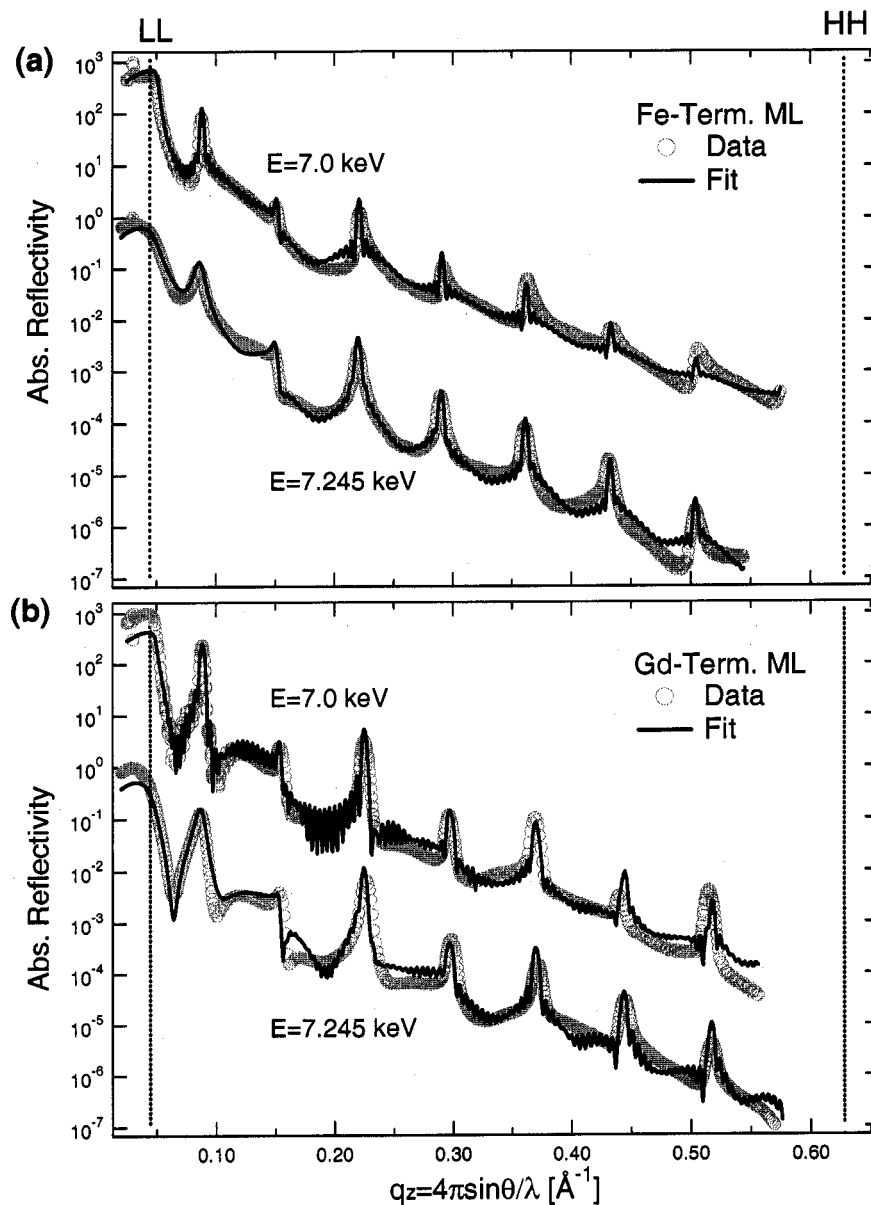


Figure 3.3. X-ray reflectivity curves measurements on Fe/Gd multilayers at 7.0 and 7.245 keV. The circles represent experimental data, and the solid lines show fitting results using Parratt's recursive formula. For clarity, $E=7.0$ keV curves (data and fits) are shifted up by a factor of 10^3 . (a) Fe-terminated multilayer. (b) Gd-terminated multilayer. The two vertical lines roughly indicate where XMCD measurements are performed at a low angle (LL) and a high angle (HH).

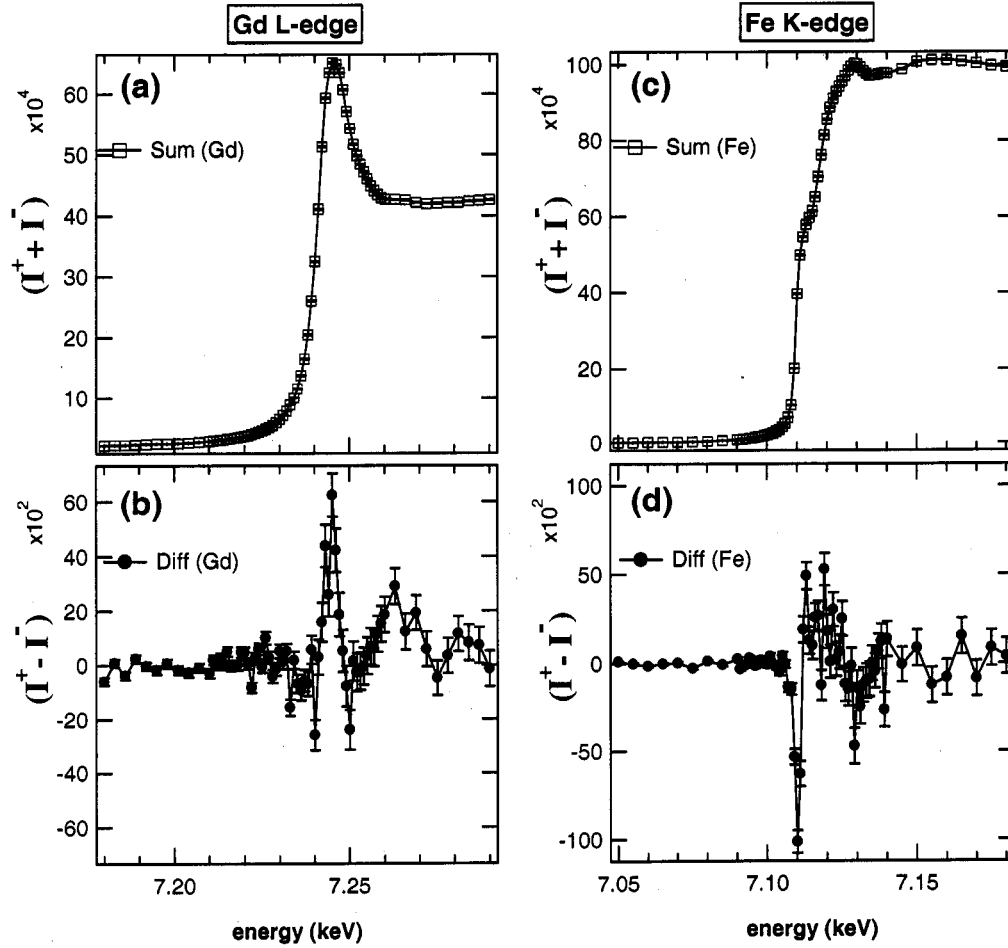


Figure 3.4. XMCD measurements on the Fe/Gd multilayer across the Gd L_3 and the Fe K absorption edges. $I^{+,-}$ are the fluorescence intensities for the two opposite helicities of the incoming x-ray. Lines are drawn to guide the eye. (a) Absorption measurements across the Gd L_3 edge. (b) Near the Gd L_3 edge, the dichroic contrast between the two opposite helicities are shown. (c) Absorption measurements across the Fe K edge. (d) Near the Fe K edge, the dichroic contrast between the two opposite helicities are shown. XMCD-hysteresis loops were measured with the x-ray energy 7.247 (Gd L_3 -edge) and 7.112 keV (Fe K-edge) where the maximum dichroic signals were observed in (b) and (d).

Table 3.3. Critical angles θ_C for Gd and Fe layers at 7.112 (Fe K) and 7.247 (Gd L_3) keV. For the surface layer sensitive XMCD measurements, the incident angle θ was 0.355° .

	7.112 keV, Fe K	7.247 keV, Gd L_3
$\theta_C(\text{Gd})$	0.374°	0.306°
$\theta_C(\text{Fe})$	0.335°	0.406°

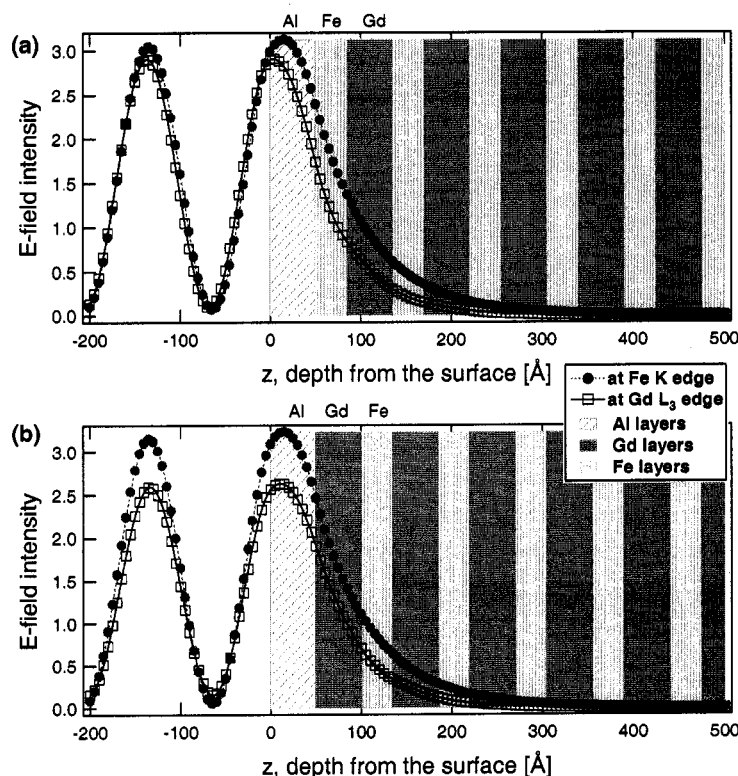


Figure 3.5. Calculated electric field intensity inside the multilayers at a grazing incident angle, 0.355° . This incident angle is near the critical angles θ_C as shown in Tab. 3.3. At $E=7.112$ keV, $\theta_C(\text{Fe})=0.335^\circ$ and $\theta_C(\text{Gd})=0.374^\circ$. At $E=7.247$ keV, $\theta_C(\text{Fe})=0.406^\circ$ and $\theta_C(\text{Gd})=0.306^\circ$. The depth from the surface is z . Positive z corresponds to inside the multilayers and the negative z corresponds to air. The first 50 \AA corresponds to the Al capping layer. The incoming x-ray energies are 7.112 (Fe K) and 7.247 (Gd L_3) keV. Lines are drawn to guide the eye. (a) Fe-terminated sample and (b) Gd-terminated sample.

3.2.2. Micromagnetic Simulation

The spin configurations in the Fe/Gd multilayers were modeled using LLG micromagnetics simulator [50]. For a ferromagnetic system, a magnetic ground state with the minimum energy can be obtained by micromagnetic calculations. The continuous magnetization distribution of a ferromagnetic system is approximated by a discrete magnetization distribution consisting of equally sized cells with a constant saturation magnetization M_S . Only the magnetization directions of the cells are varied until a minimum energy configuration is reached, and the configuration is found by solving the Landau-Lifshitz-Gilbert equation in the following form [51, 52, 53].

$$(3.1) \quad \frac{\partial \mathbf{M}}{\partial t} = -\frac{1}{1 + \alpha^2} \left[\gamma \mathbf{M} \times \mathbf{M}_{eff} + \frac{\gamma \alpha}{M_S} \mathbf{M} \times (\mathbf{M} \times \mathbf{H}_{eff}) \right]$$

γ is the gyromagnetic frequency, α is the damping factor, \mathbf{H}_{eff} is the effective field, and \mathbf{M} is the sample magnetization. The effective magnetic field includes all the effects from exchange, anisotropy, external fields and demagnetizing fields (described in detail in **Appendix D**).

The Fe-terminated and the Gd-terminated samples were modeled separately in micromagnetic simulations to see the termination effect. For the Fe-terminated sample ($[\text{Fe}(35 \text{ \AA})/\text{Gd}(50 \text{ \AA})]_{15}/\text{Fe}(35 \text{ \AA})$), the total simulation volume was $50 \times 50 \times 0.131 \mu\text{m}$. The simulation cell size was $50 \times 50 \times 0.0005 \mu\text{m}$, and each Fe and Gd layer were sliced into 7 and 10 sublayers, respectively. The same cell size was used for the Gd-terminated sample ($[\text{Gd}(50 \text{ \AA})/\text{Fe}(35 \text{ \AA})]_{15}/\text{Gd}(50 \text{ \AA})$) with $50 \times 50 \times 0.1325 \mu\text{m}$ total simulation volume. An equilibrium configuration was assumed when the maximum

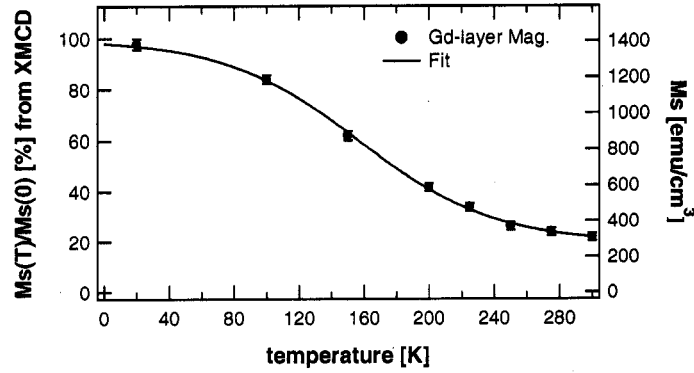


Figure 3.6. Gd layer magnetization at temperatures between 20 and 300 K. The symbols are from XMCD measurements on a similarly grown $([\text{Gd}(50 \text{ \AA})/\text{Fe}(15 \text{ \AA})]_{15})$ multilayer in which Gd and Fe moments are collinear with the applied field up to 300 K, and the line is a fit to the XMCD data. For the simulation, the saturation moment of Gd at 0 K was reduced by 30% from the bulk value of $M_0 = 2020 \text{ emu/cm}^3$.

change in $|M/M_S|$ was less than 10^{-9} , and making the convergence criteria more strict did not affect the simulation output.

For the Fe layers, the saturation moment M_S was 1700 emu/cm^3 and the layer exchange J_{Fe} was $2.1 \text{ } \mu\text{erg/cm}$. It was assumed that the changes in these Fe magnetic parameters were negligible from 20 to 300 K since the temperatures within this range are well below $T_C(\text{Fe})=1024 \text{ K}$. While the anisotropy in the Gd layers was assumed to be negligible, a uniaxial magnetic anisotropy was included for the Fe layers. Later, in order to match the simulation data with the experimental results, the magnitude and direction of the Fe anisotropy were varied. For Gd, J_{Gd} was calculated relative to J_{Fe} , assuming 3D Heisenberg model, $J=3k_B T_C/2zS(S+1)$ with reduced $T_C(\text{Gd})=220 \text{ K}$. $T_C(\text{Gd})$ was determined experimentally by XMCD measurements on a similarly grown $([\text{Gd}(50 \text{ \AA})/\text{Fe}(15 \text{ \AA})]_{15})$ multilayer (Fig. 3.6) [54]. J_{Gd} was calculated to be $0.054 \text{ } \mu\text{erg/cm}$, and the antiferromagnetic coupling between Gd and Fe

was chosen to be $J_{Fe/Gd} = -(J_{Fe} + J_{Gd})/2 = -1.077 \text{ } \mu\text{erg/cm}$. The saturation moment of Gd at 0 K was reduced by 30% from its bulk value in order to reproduce the XMCD-hysteresis experimental results. Simulations for different temperatures were modeled by changing $M_S(Gd)$. It was assumed that the temperature dependence of Gd saturation moment is the same for the current samples and the above mentioned $[(\text{Gd}(50 \text{ } \text{\AA})/\text{Fe}(15 \text{ } \text{\AA}))_{15}]$ multilayer. The relative Gd magnetization values at different temperatures were calculated using the XMCD curve in Fig. 3.6 to get the Gd saturation moments.

3.3. Results and Discussion

3.3.1. Fe-terminated sample

XMCD-hysteresis loops measured on the Fe-terminated sample are shown in Fig. 3.7. The results in the first and the third columns were measured at the grazing incident angle for top layer sensitivity (labelled “surface”), and the other two columns show the measured results at the high angle (labelled “total”). At each temperature, the Gd and Fe XMCD signals have opposite signs indicating antiparallel alignment between the Gd and Fe moments. From the SQUID results (Fig. 2.3), the compensation point is around 85 K for this sample. In Fig. 3.7, the sign of hysteresis loops is reversed between 65 and 90 K in agreement with the SQUID results.

What is noticeable in Fig. 3.7 is that *surface* hysteresis loops are tilted at 45 K while their *total* counterparts are not. Since the XMCD signal is proportional to the moment projected along the applied field direction, this *tilting* indicates there

are some moments twisted away from the field direction at high fields. At low temperatures, the multilayer is in the Gd-aligned state where Fe (Gd) magnetization is antiparallel (parallel) to the field. The spins in the top Fe layer are coupled to the spins in Gd layer on only one side. Because of this reduced coupling effect, the top Fe layer spins start to twist away from the field direction. Meanwhile, the interior Fe layers are coupled to Gd layers on both sides and they remain antiparallel to the field direction. This *twisting* starts from the surface and it penetrates even to the first Gd layer, as shown in the first hysteresis loop in Fig. 3.7(b).

As the temperature is increased above the compensation temperature, the sample is in the Fe-aligned state and the situation is reversed. At 90 K, the top Fe layer is now aligned parallel to the field and the twisting does not occur at the surface. Instead, the twisting occurs at the middle layers (bulk twisted state), and the *total* hysteresis loops are tilted while the *surface* loops are not.

Near the compensation temperature, the XMCD loops at 80 K in Fig. 3.7 show interesting features. The *surface* loops at this temperature are shifted horizontally, and the *total* hysteresis loops do not change their magnetization directions even as the applied field is reversed. At this temperature, the Gd layer and the Fe layer magnetization contributions are comparable to each other, and an additional effect may play a role in tipping the balance, causing the observed features.

The spin configurations in the Fe-terminated sample were simulated using micro-magnetic calculation as shown in Fig. 3.8. The ground state configuration was found at each field value, and relative magnetization was calculated by projecting each sub-layer spin along the field direction. The first and the third columns in Fig. 3.8 were

obtained by averaging the projected magnetization of the sublayers in the first Fe or Gd layers, respectively. The second and the fourth columns were obtained by averaging magnetization values from all Fe or Gd sublayers, respectively.

Initially, no anisotropy was included in the simulated systems. Magnetic anisotropy contributions are often ignored in these Fe/Gd multilayers systems [14, 15] because Gd has very weak magnetic anisotropy and also because the multilayers studied are typically poly-crystalline. In this study, when no anisotropy was included, the micromagnetic simulation results were in good agreement with the XMCD experimental results except for near T_{Comp} . As discussed earlier, the XMCD measurements near T_{Comp} show distinctive features such as field-shifting and non-reversing of the loops, and these features could not be reproduced in the simulations as shown in Fig. 3.9. In order to check if the observed features are due to some anisotropy contributions, a uniaxial anisotropy was included in the Fe layers in the micromagnetic simulations. The magnitude and direction of this anisotropy were varied while comparing with the XMCD experimental results. When a uniaxial anisotropy of 4700 erg/cm^3 was included at 30° away from the applied field direction, the observed features in the XMCD measurements (field-shifting and non-reversing of the loops) were reproduced in the micromagnetic simulations with the anisotropy. This anisotropy \mathbf{K} corresponds to 10% of the nominal value of bulk Fe anisotropy. The corresponding anisotropy field is $H=2K/\mu_0 M_S=3.25 \text{ Oe}$. The anisotropy was relatively weak so that away from the T_{Comp} , two simulation sets (with and without the anisotropy) were not significantly different from each other as shown in Fig. 3.9(b). However, near T_{Comp} the difference between the two simulations is significant. The simulation results shown in Fig. 3.8

are based on the calculations with the above mentioned uniaxial anisotropy in the Fe layers.

Based on the simulation results, the spin configurations near T_{Comp} are visualized in Fig. 3.10, and the observed features in the XMCD measurements in Fig. 3.7 can be explained by these configurations. The XMCD results show that near T_{Comp} , the total XMCD signals are maximized at zero field and minimized at high fields. The Fe/Gd multilayer is aligned with anisotropy direction at remanence [Fig. 3.10(c)], and the Gd and Fe moments spread out across the M_X/M_S axis at high fields [Figs. 3.10(a),(e)]. This spreading out at high fields occurs in such a way that almost equal number of spins are in the $M_X/M_S > 0$ and $M_X/M_S < 0$ regions causing the Gd- and Fe-XMCD signals to be almost zero as shown in the third row in Fig. 3.7 [also re-plotted in Fig. 3.9(a)]. The XMCD measurement results also show that the Gd and Fe moments do not change signs even as the applied field is reversed. The simulation results in Fig. 3.10 agree with the XMCD results showing that the Gd spins are in the $M_X/M_S > 0$ region at $H = -80$ and $+80$ Oe while the Fe spins are in the opposite region [Figs. 3.10(b),(d)]. However, the direction of the “bulging” is different between the two opposite field values. The XMCD-hysteresis loops from the *surface* Fe and Gd layers exhibit a field shift as shown in Fig. 3.7, and the this field shift is also reproduced in the micromagnetic simulations. For the *surface* and center layers, Fe and Gd magnetizations are illustrated in Fig. 3.11. As the applied field is reversed from $H = -400$ Oe to $H = +400$ Oe, the Fe and Gd *surface* layer magnetizations does not change their signs until $H = +160$ Oe causing a field shift in hysteresis loops as if they were biased. The effect of the Fe anisotropy is evident here, and as the field

is reversed, a significant field ($\approx +160$ Oe) is required to cant away the Fe moments from the easy axis direction.

From the simulation results, T_{Comp} lies around 82 K. The micromagnetic simulation results follow the trend of the experimental data. Below T_{Comp} , the surface Fe and Gd layer hysteresis loops show *twisting* at moderate fields while the total Fe and Gd layers hysteresis loops show slight twisting only at high fields (Fig. 3.7-3.8). Figure 3.12 shows the spin configurations at four fields at 41 K. At remanence, the multilayer is in the Gd-aligned state [Fig. 3.12(a)] and the spins are aligned with the Fe-anisotropy direction \mathbf{K} . As the field is increased, the twist starts at the surface and progressively penetrates deeper into the film [Figs. 3.12(b)-(d)]. The fanning of spins within layers is more pronounced in the Gd layer because the exchange coupling of Gd, J_{GdGd} , is relatively weaker than that of Fe, J_{FeFe} . In the surface twisted state as shown in Fig. 3.12(d), the surface layers are magnetized almost perpendicular to the field while the center layers are magnetized almost collinear with the field. This is reminiscent of surface spin flop as illustrated in Fig. 3.11.

The experimental and simulation results show that at temperatures above T_{Comp} ($T=99$ K) *twisting* is more pronounced in the total Fe and Gd hysteresis loops than in the surface Fe and Gd loops (Figs. 3.7-3.8). This suggests that the spins are more twisted in the interior layers than in the surface layers. This can be visualized with the spin configuration plots as shown in Fig. 3.13. For $T > T_{Comp}$, the multilayer is in the Fe-aligned state [Figs. 3.13(a)-(b)] at low fields, and as the field is increased, the spins of the middle layers start to twist away from the field direction, and the twisting of Gd and Fe spins progresses up to near the surface layer [Figs. 3.13(c)-(d)]. In the

bulk twisted state as shown in Fig. 3.13(d), the magnetizations in the center layers are more twisted away from the field direction than the magnetizations in the surface layers. For the *surface* and center layers, Fe and Gd magnetizations are illustrated in Fig. 3.11.

The surface and interior magnetization directions are plotted in Fig. 3.11 for the three temperatures where the surface twist, near T_{Comp} , and the bulk twist states were observed in the simulation results. For the three cases, at zero field, the Fe and Gd magnetizations are collinear, but as the applied field is increased, the magnetization directions are canted away from the field direction in such a way that the Gd and Fe magnetizations are not collinear anymore. The antiferromagnetic coupling at the interfaces between the Fe and Gd layers wants to keep the two components collinear to minimize the exchange energy (since $E_{exchange} \sim C_1(1 - \mathbf{m}_{Fe} \cdot \mathbf{m}_{Gd})$ with $C_1 < 0$). As the field is increased, the Zeeman energy component becomes more dominating, and a net moment (Fe+Gd) along the field increases through this non-collinear canting toward the field between the Fe and Gd magnetizations, as illustrated in Fig. 3.11. The Zeeman energy reduction by the increased net moment (Gd+Fe) is compensated by the exchange energy gain due to the non-collinear alignment.

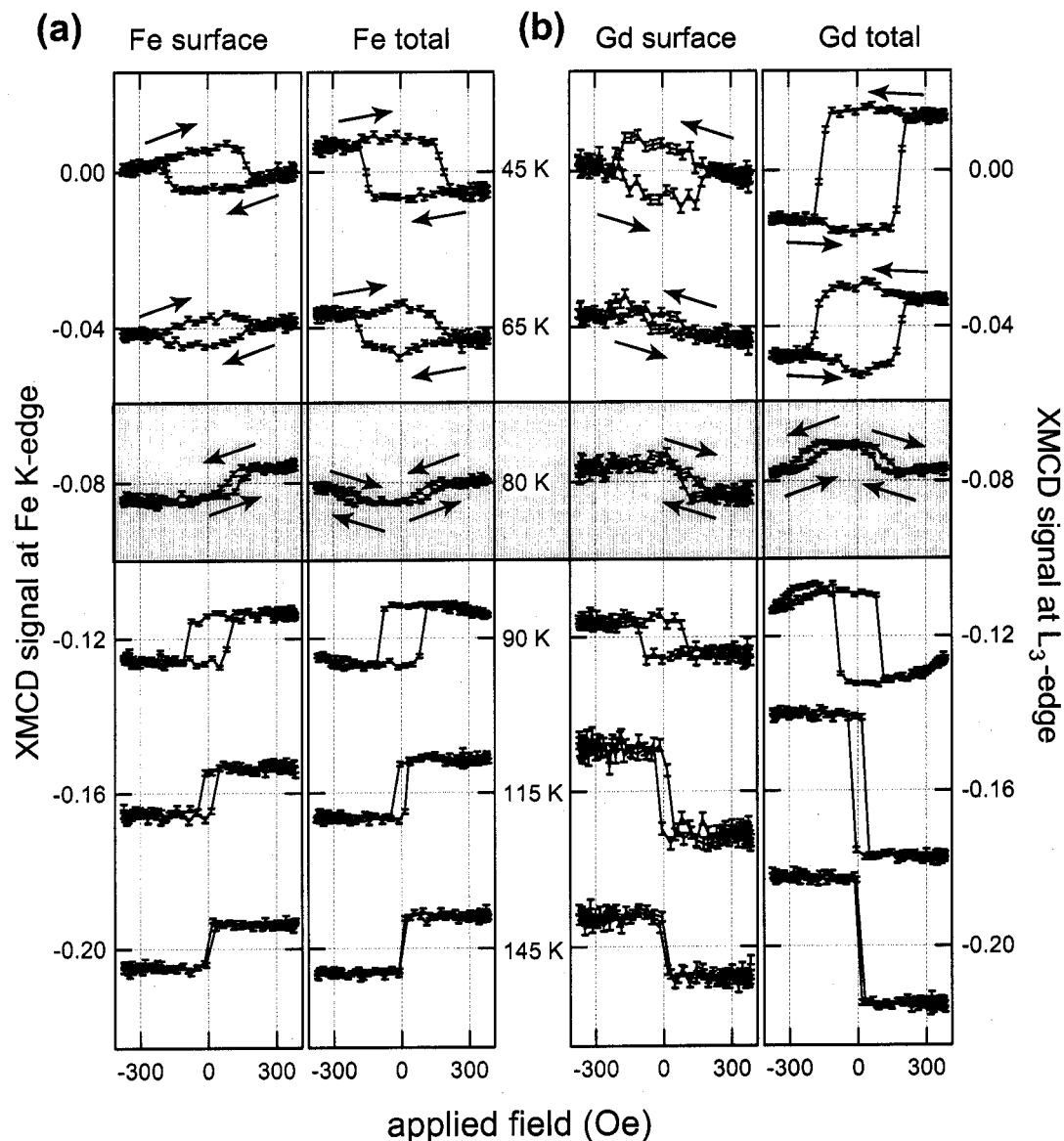


Figure 3.7. XMCD-hysteresis loops from the Fe-terminated sample at 45, 65, 80, 90, 115, and 145 K. The first column in each plot is for the top layers and the second column is for the total layers. The XMCD signals are proportional to the projected moments along the field. For clarity, the hysteresis loops are shifted down by multiples of 0.04 vertically. The Gd surface hysteresis loops are scaled up by a factor of 2. The loops at 80 K are shaded to indicate the temperature is near the compensation point. (a) Fe hysteresis loops. (b) Gd hysteresis loops.

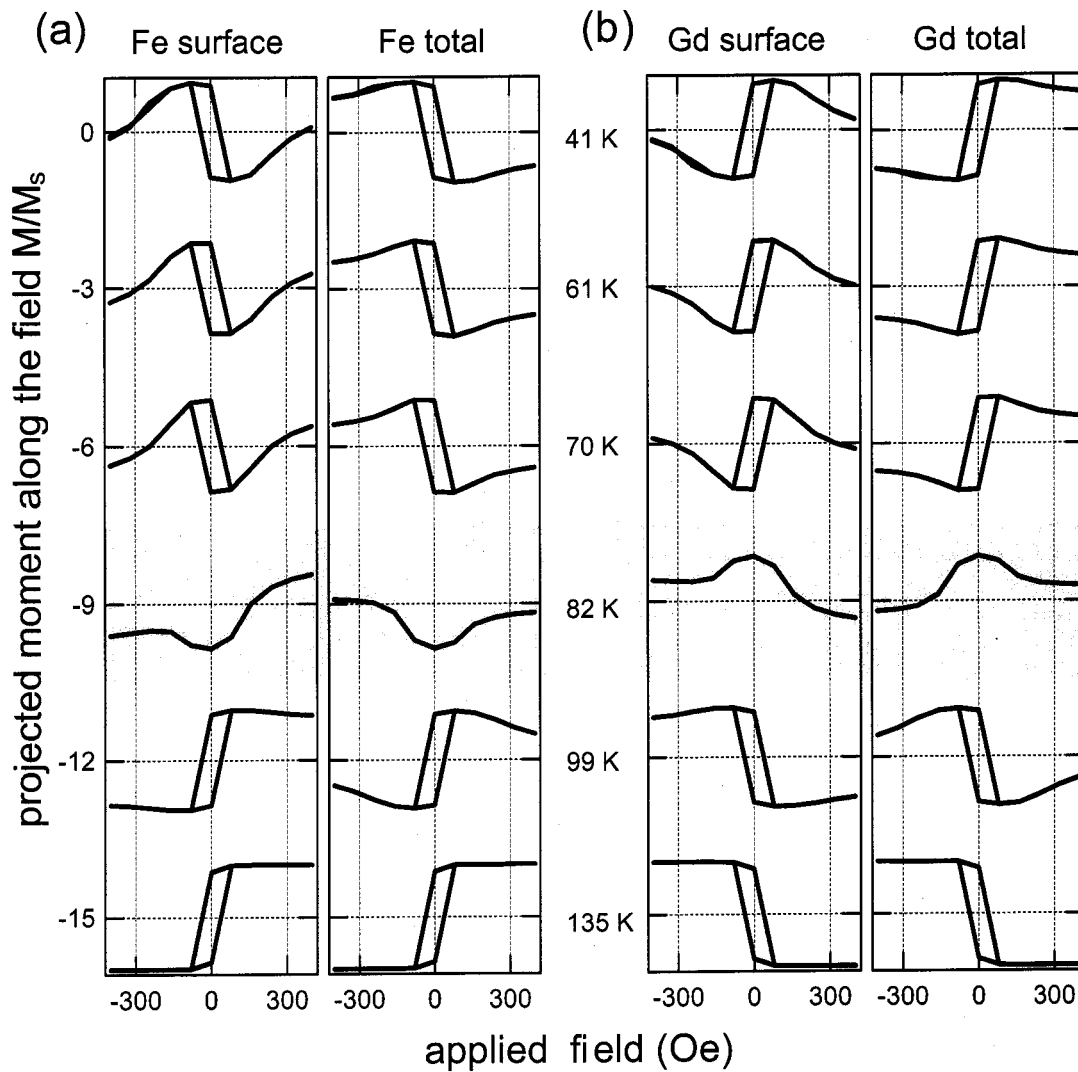


Figure 3.8. Micromagnetic simulations on the Fe-terminated multilayer. The values M/M_S in the y-axis are projected moments along the field normalized by the saturation moment M_S . The loops are shifted down by multiples of 3 vertically for clarity. The loops at 82 K are shaded to indicate the temperature is near the compensation point. (a) Fe hysteresis loops. (b) Gd hysteresis loops.

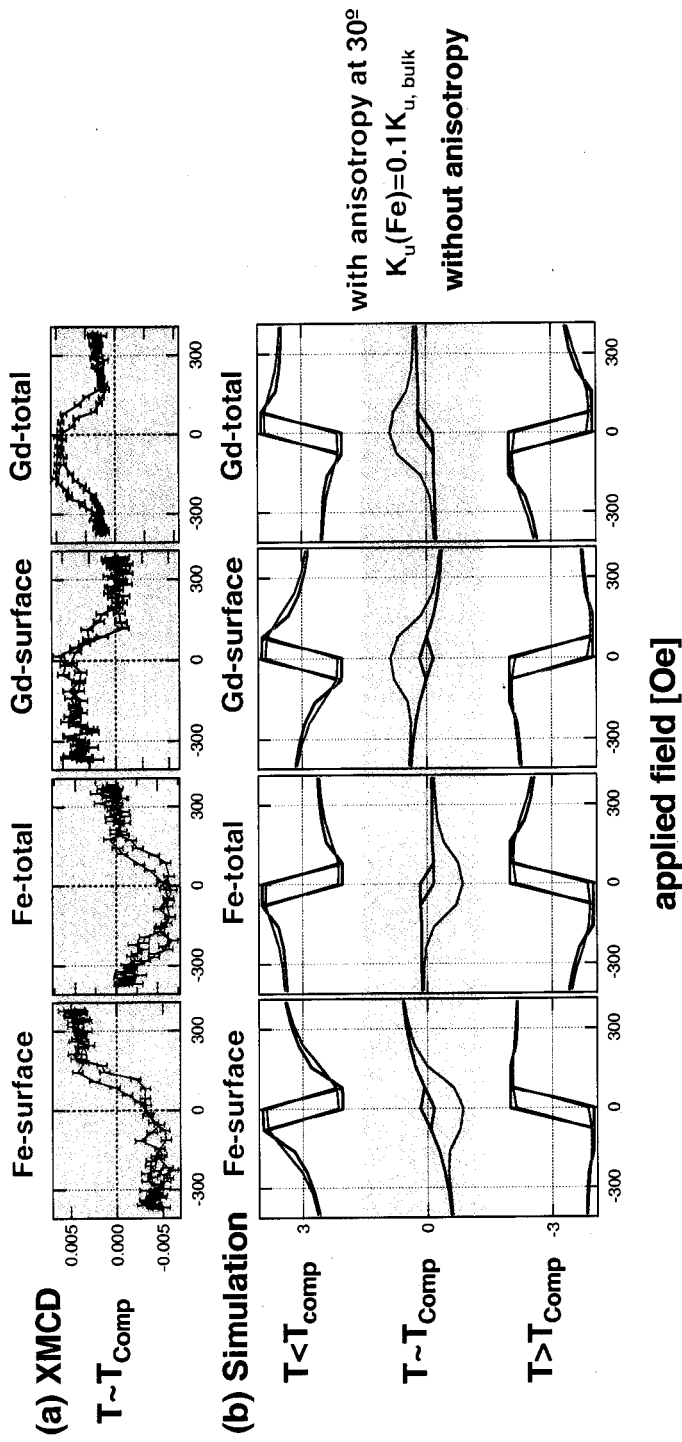


Figure 3.9. The effect of a weak anisotropy in the Fe layers. (a) XMCD-hysteresis loops near T_{Comp} . (b) Micromagnetic simulations at $T < T_{\text{Comp}}$, $T \sim T_{\text{Comp}}$, and $T > T_{\text{Comp}}$. The black lines represent simulation results without a Fe anisotropy, and the red lines represent simulation results with an uniaxial Fe anisotropy.

$$T \sim T_{\text{comp}}$$

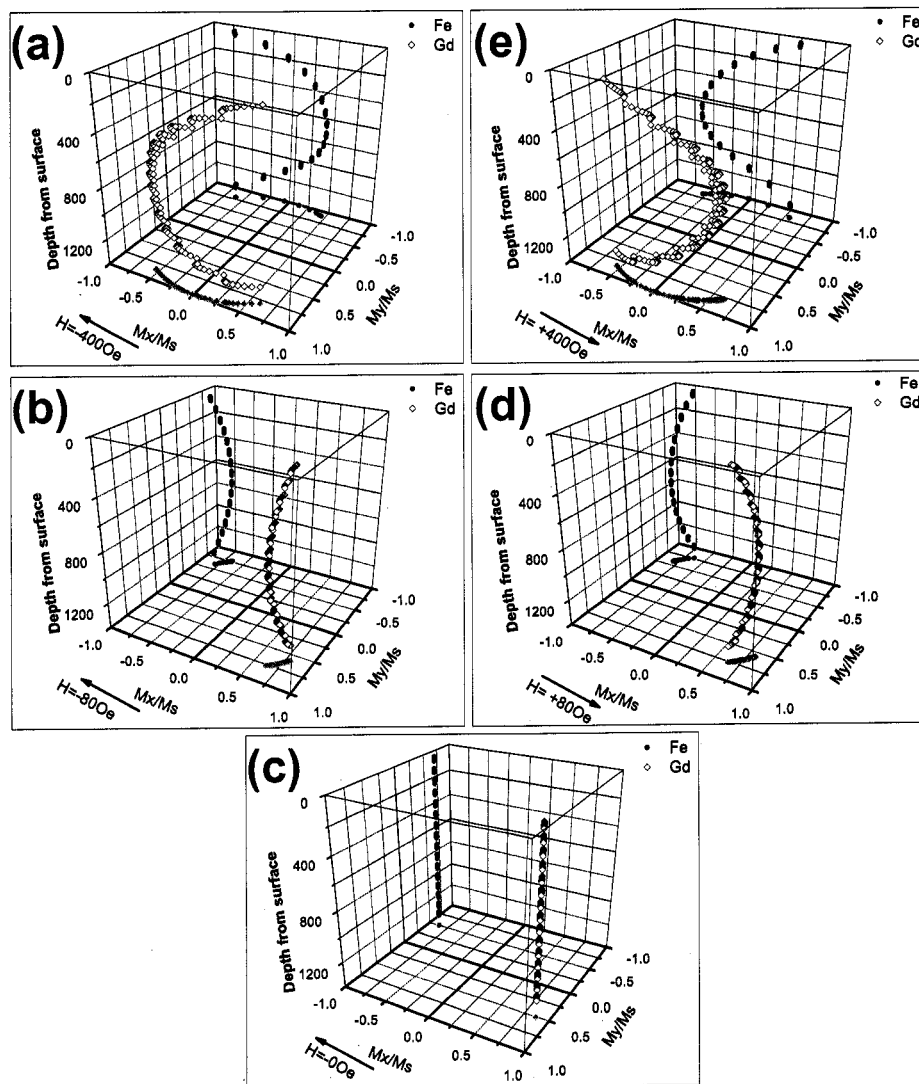


Figure 3.10. Spin configurations from the simulations for the Fe-terminated sample at a temperature near T_{Comp} at the selected field values as the field was swept as in Figure 3.8. The red solid circles represent the Fe moments, and the blue diamonds are for the Gd moments. The arrows indicate the applied field direction, and the projected spin directions onto the bottom M_X - M_Y plane are shown as the light-colored symbols. (a) At -400 Oe, (b) at -80 Oe (c) at remanence, (d) at +80 Oe, and (e) at +400 Oe.

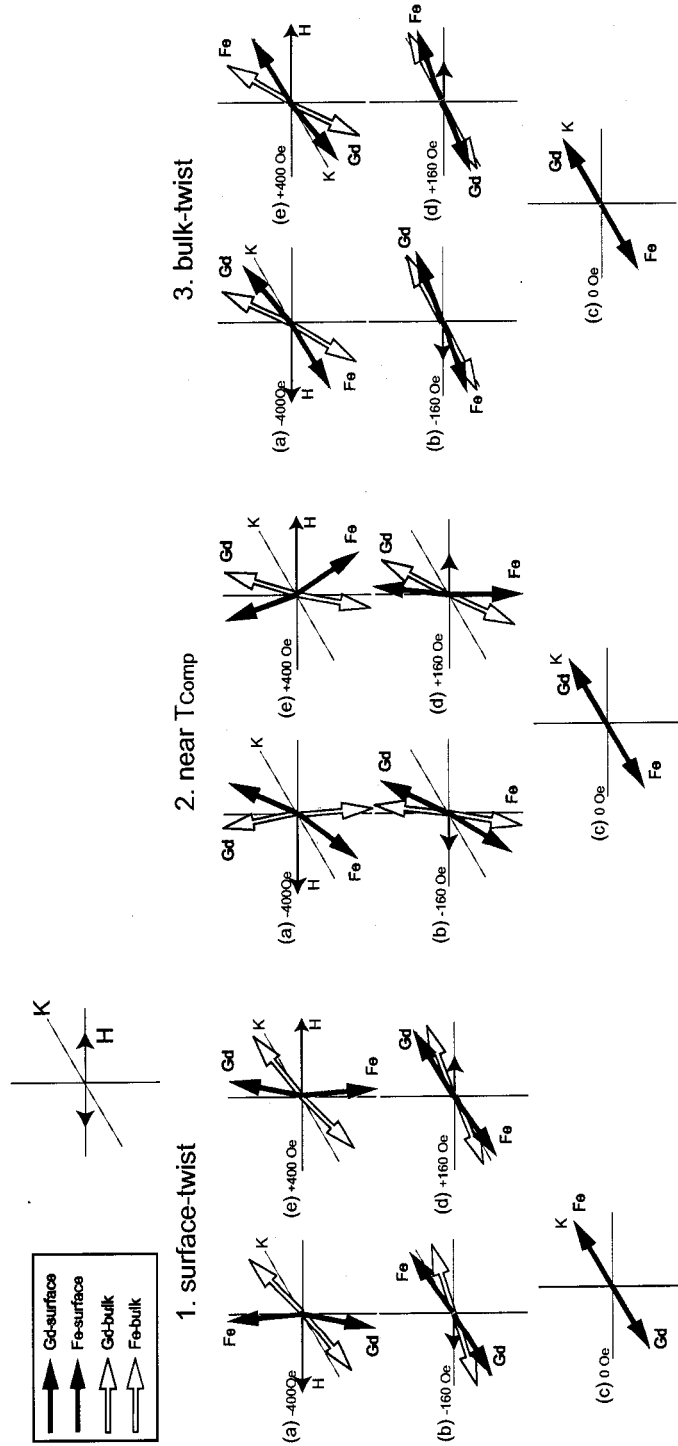


Figure 3.11. Surface and bulk magnetization directions at (1) surface twist state, (2) near T_{Comp} , and (3) bulk twisted state. The applied field is represented by H and the easy axis of the Fe layer anisotropy is represented by K . Gd magnetizations are represented by the blue arrows and Fe magnetizations are represented by the red arrows. The solid arrows are for surface layers, and the hollow arrows are for interior layers.

$$T < T_{\text{comp}}$$

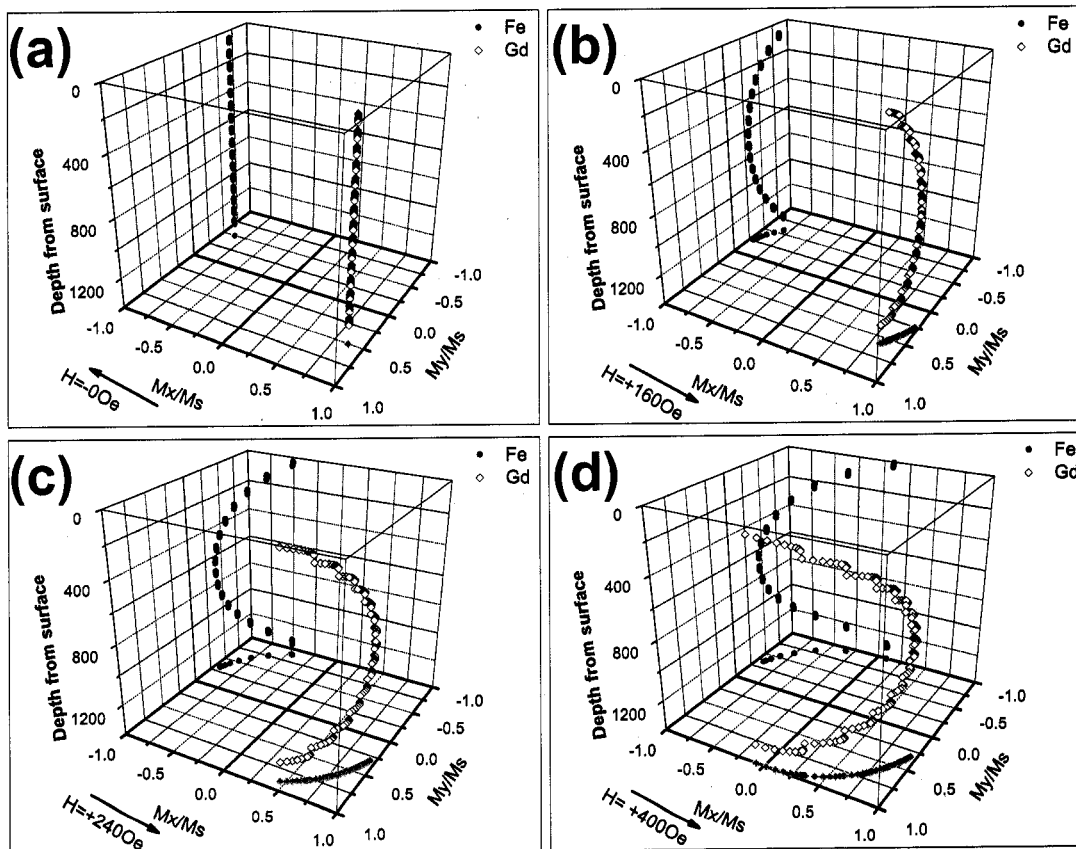


Figure 3.12. Spin configurations from the micromagnetic simulations are shown for the Fe-terminated sample at a temperature below T_{Comp} at the selected field values as the field was swept as in Figure 3.8. The spin orientation of each sublayer is plotted in the M_X - M_Y plane where the applied field direction is parallel to M_X . The red solid circles represent the Fe moments, and the blue diamonds are for the Gd moments. The arrows indicate the applied field direction, and the projected spin directions onto the bottom M_X - M_Y plane are shown as the light-colored symbols.

$$T > T_{\text{comp}}$$

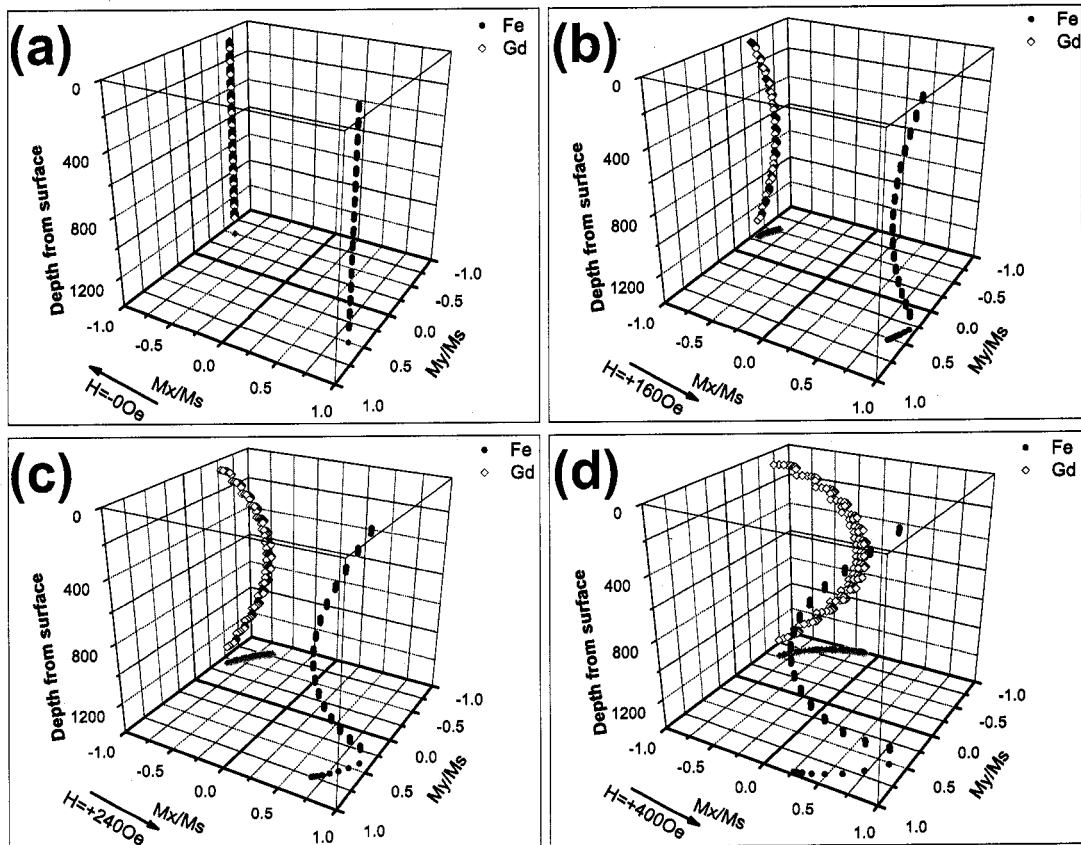


Figure 3.13. Spin configurations from the simulations for the Fe-terminated sample at a temperature above T_{Comp} at the selected field values as the field was swept as in Figure 3.8. The red solid circles represent the Fe moments, and the blue diamonds are for the Gd moments. The arrows indicate the applied field direction, and the projected spin directions onto the bottom M_x - M_y plane are shown as the light-colored symbols.

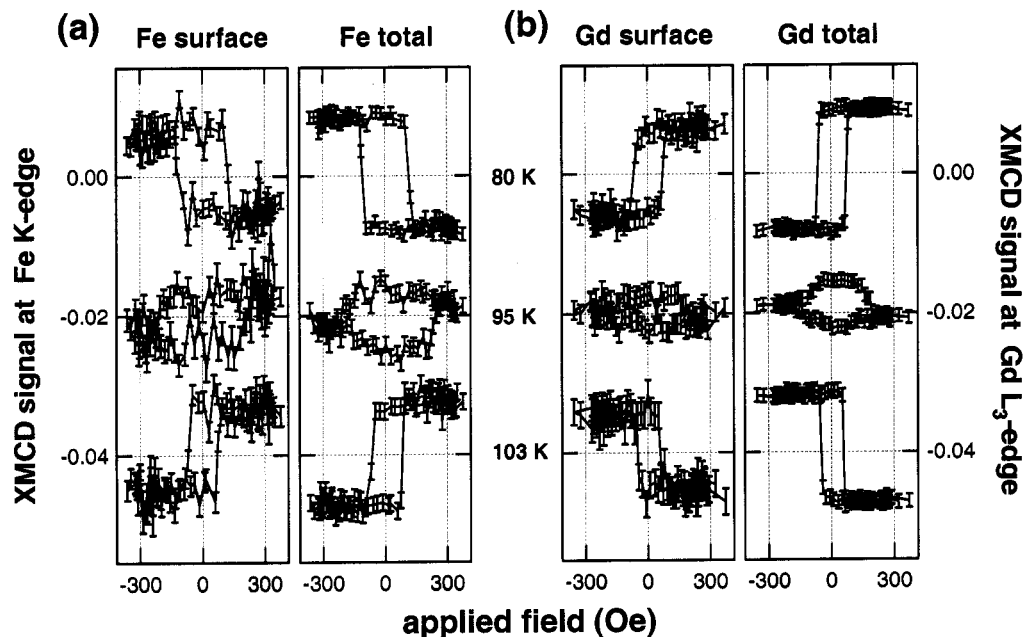


Figure 3.14. XMCD-hysteresis loops from the Gd-terminated sample at 80, 95, and 103 K. The first column in each plot is for the top layers and the second column is for the total layers. The plots are shifted vertically for clarity. The Gd surface hysteresis loops are scaled up by a factor of 2 (a) Fe hysteresis loops. (b) Gd hysteresis loops.

3.3.2. Gd-terminated sample

Similarly measured XMCD-hysteresis loops on the Gd-terminated sample are shown in Fig. 3.14. The compensation point for this sample is between 95 and 103 K above (below) which the sample is in Fe-aligned (Gd-aligned) state. The *twisting* at the surface layers is not observed at low temperature from this sample. The top-most layer is Gd in this case, and it is aligned parallel to the field at low temperatures. Thus the *twisting* does not occur in the first Gd layer. The Fe layer is below this first Gd layer, and since the Fe coupling is strong, it is too costly energetically to have Fe spins twisted away from the field direction. However, this situation is reversed above

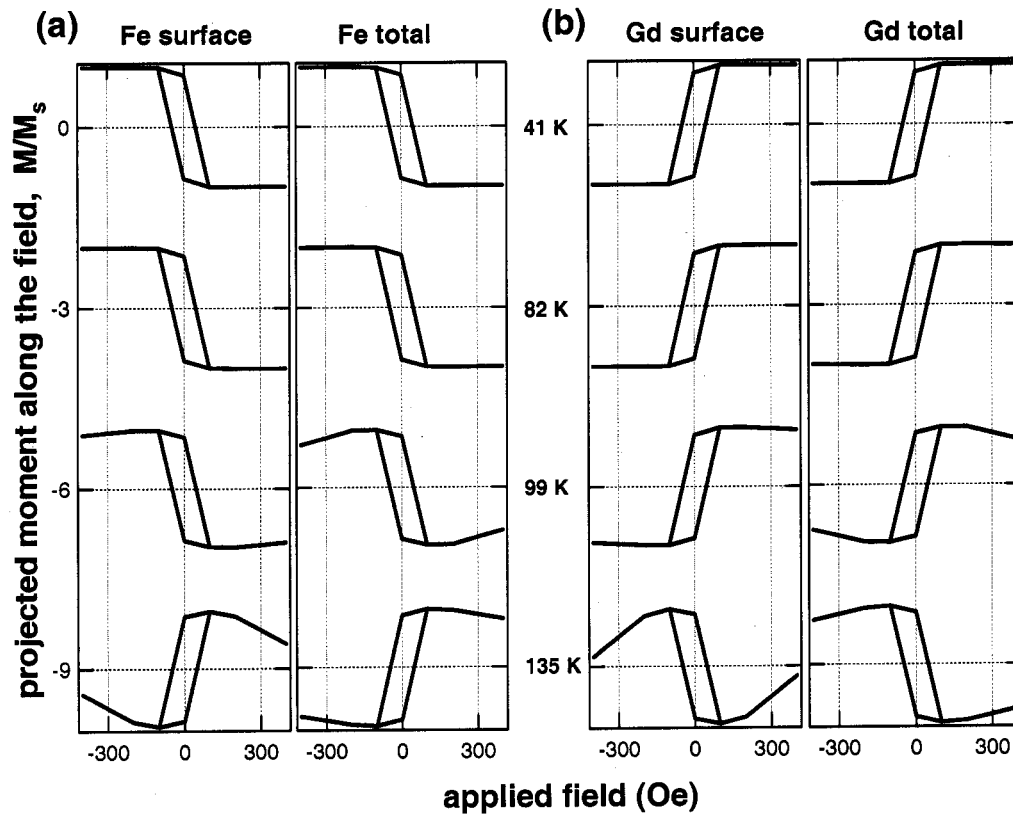


Figure 3.15. Micromagnetic simulations on the Gd-terminated multi-layer. The plots are shifted vertically for clarity. (a) Fe hysteresis loops. (b) Gd hysteresis loops.

the compensation temperature. Now, the sample is in the Fe aligned state with the top Gd layer magnetized antiparallel to the field direction, and *twisting* can occur in the first layer.

The spin configuration is simulated with the micromagnetic calculation as shown in Fig. 3.15. Compared with the case for the Fe-terminated sample (Fig. 3.8), it noticeable that the extent of twisting is less pronounced and that the *twisting* occurs

at higher fields. This may explain why bulk *twisting* below T_{Comp} and surface *twisting* above T_{Comp} were not observed experimentally in Fig. 3.14.

3.4. Conclusion

Using XMCD in a depth-sensitive way, surface and bulk twisted magnetic states were observed in a Fe/Gd multilayer. To probe near-surface layers, XMCD measurements are performed at a grazing incident angle, and to probe the total layers, XMCD measurements are repeated at a high incident angle. In the Fe-terminated multilayer the surface twisted state was observed at temperatures below the compensation point. Above the compensation point, the bulk twisted state was observed. To reconstruct the spin configurations, micromagnetic simulations were performed, and the observed features in the experiments were reproduced in the simulations. Near the compensation temperature of the Fe/Gd multilayer, field shift and non-reversing of XMCD-hysteresis loops were observed, and the observed phenomena were explained by the effect of weak Fe anisotropy.

The surface twisted state was not observed in the Gd-terminated sample at low temperatures. The twisted spin states were not observed at temperatures around the compensation temperature while the micromagnetic simulation results show the bulk twisting below the compensation point and the surface twisting above the compensation point. This may be due to the fact that the twist angle in the bulk twist is less pronounced and that the twisted states occur at higher field in the Gd terminated sample.

CHAPTER 4

Magnetic Domain Studies on Patterned Structures

Recent advances in lithographic and other fabrication techniques have led to the fabrication of a number of novel systems at the nanometer length scale. Periodic arrays of magnetic structures have received much attention recently because of their potential as high density magnetic storage media. From a fundamental point of view, because of reduced size and lateral confinement effects, the patterned structures show magnetic behaviors different from that of continuous film structures. Some of the important issues in patterned magnetic array structures are the switching mechanism during magnetization reversal, size effects, the uniformity among constituent individual structures, exchange coupling, and magnetostatic coupling [55]. In patterned particle arrays, the magnetization reversal is limited within a particle, and the reversal mode can be coherent or incoherent. Through a better understanding of these fundamental issues, future applications can take advantage of the novel properties, and thus leading to the development of magnetic systems with tailor-made properties.

Two examples of patterned magnetic structures were studied: hole arrays and pseudo-spin-valve structures. For these patterned samples, e-beam lithography was used to pattern PMMA resist coated on Si-substrates, and e-beam evaporation and lift-off processes were used as described in Fig. 4.1.

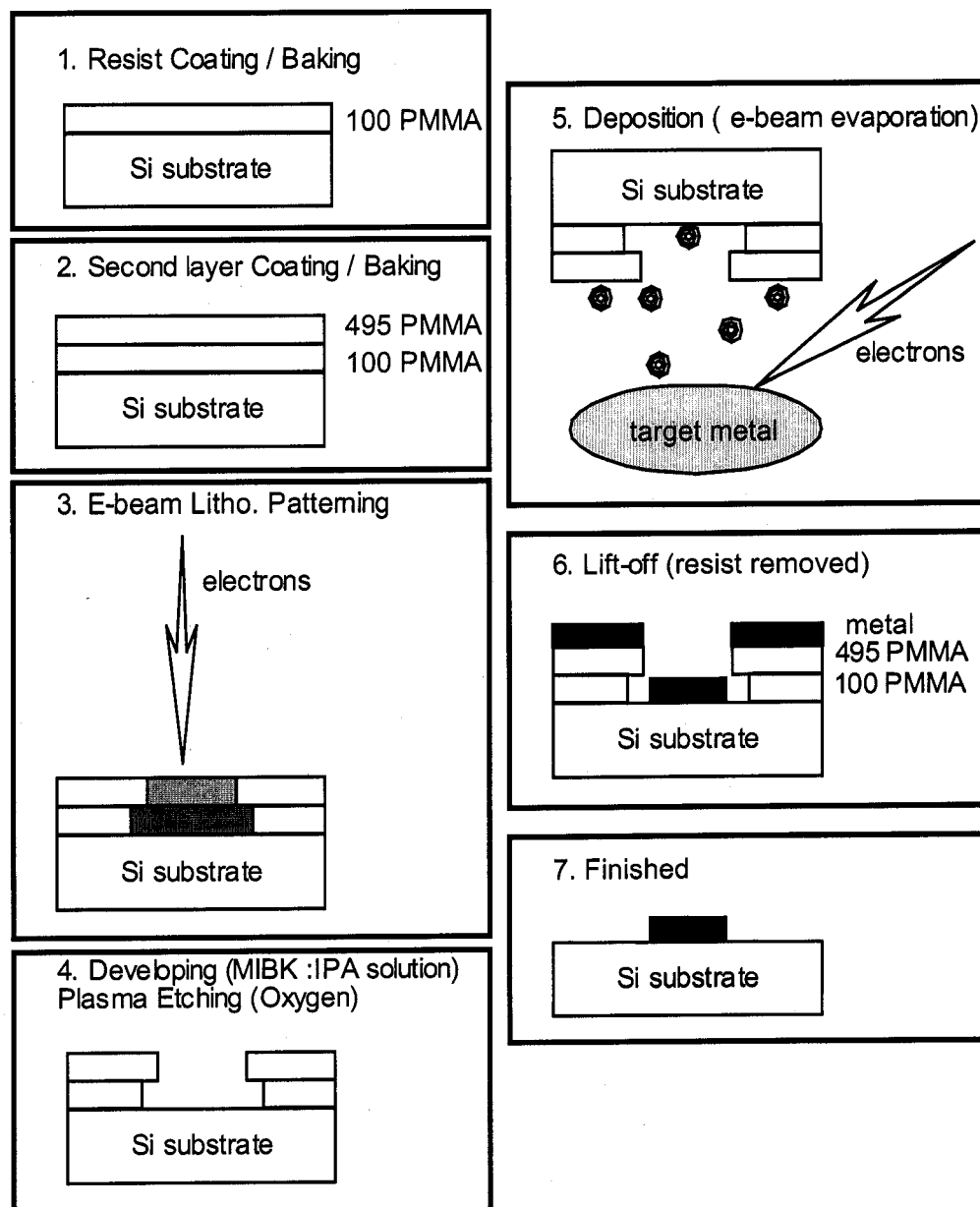


Figure 4.1. Patterning process. (1)-(2) E-beam resist layers are spin-coated. (3) Patterns are made on the resist layers by e-beam lithography. (4) With a developing solution, the resist area weakened by the e-beam is removed, and any residual is removed by etching. (5) Target metal is evaporated onto the developed pattern. (6) The resist is removed by lift-off process.

4.1. Magnetic Hole Arrays

Recently hole arrays have received much attention because of their possible application as magnetic data storage devices. Due to the patterning effect, hole arrays possess unique and desirable magnetic properties, such as shape-induced magnetic anisotropy and pinned magnetic domain structure [56]. Typically, hole arrays at remanence show three types of magnetic domains that behave as single domains during a magnetization reversal process.

For this work, circular holes in a square array on Fe/Gd multilayered films were studied. First, the hole array was patterned on PMMA covered Si-substrates using e-beam lithography, then $[\text{Fe}(3\text{ nm})/\text{Gd}(2\text{ nm})]_8$ films were prepared by evaporation and lift-off processes. The patterned area was about $10\text{ mm} \times 10\text{ mm}$. This system is chosen as a model heterogeneous system with constituent elements having very different Curie temperatures. Thus, at different temperatures, the magnetic contributions from the two layers can vary. The influence of interlayer coupling on domain formation and switching of Fe and Gd layers can also be studied. The focus here is on the Fe layers at room temperature where the layers are decoupled.

4.1.1. Initial characterization with magneto-optical Kerr effect measurement

With linearly polarized optical light, initial characterization of the hole array samples were performed using the magneto-optical Kerr effect (MOKE). Kerr effect and Faraday effect are magneto-optical effects that are based on the interaction of light with magnetized media; the linearly polarized light changes its polarization state after

the interaction with the magnetized media. The Faraday effect occurs when linearly polarized light is transmitted through a magnetized material, and the Kerr effect occurs when the light is reflected from the magnetized material. With optical light, the Kerr effect is more commonly used because the Faraday effect requires transparent media while the Kerr effect requires a magnetized sample with a sufficiently smooth surface. Depending on the measurement geometry, the magneto-optical Kerr effect can be categorized into longitudinal, transverse, and polar MOKE. As illustrated in Fig. 4.2(a), the longitudinal and transverse MOKE measures magnetization components in the film plane while the polar MOKE is sensitive to the component in the surface normal direction.

MOKE magnetization curves were measured in the transverse MOKE configuration [57] with π -polarized incident light emitted by a Ar-laser with $\lambda=51.5\text{nm}$. The MOKE setup used is shown in Fig. 4.2(b). With the external field normal to the scattering plane, the magnetization component parallel to the field direction is measured. In this setup, as the sample magnetization changes, only the reflected intensity changes while the reflected light remains linearly polarized [58]. This means that as the magnetization changes from $+M$ to $-M$, the reflected light intensity changes from $I+\Delta I$ to $I-\Delta I$, leaving the light polarization state unchanged.

MOKE magnetization curves are measured on both unpatterned and patterned films to determine the direction of an intrinsic uniaxial anisotropy. MOKE magnetization curve was obtained at one sample orientation, and the second data curve was obtained after the sample was rotated 90° while other experimental conditions were fixed. The two curves were not equivalent, indicating the magnetic anisotropy in the

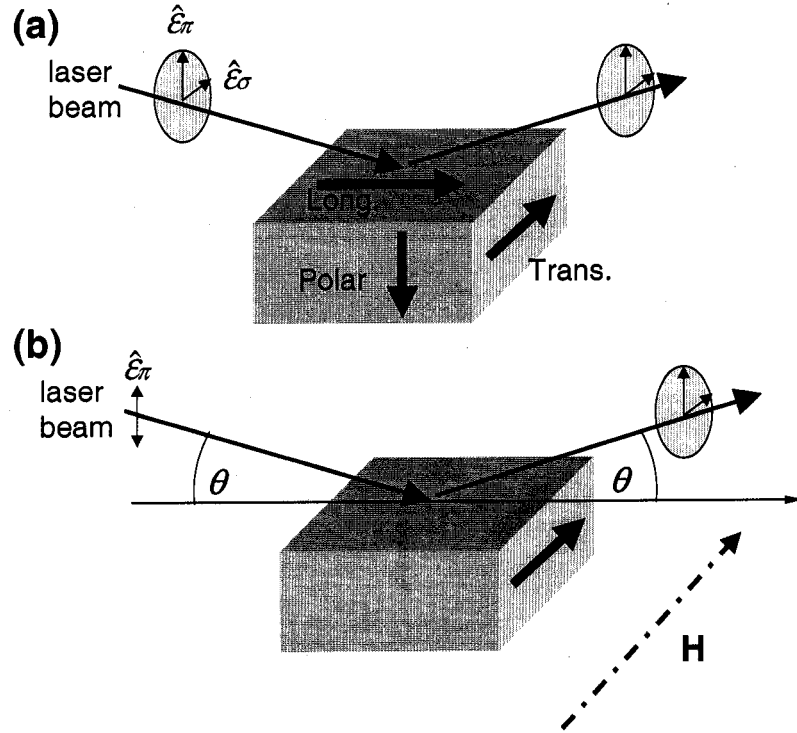


Figure 4.2. Experimental geometry for MOKE measurements. The inside arrows indicate sample magnetization components. (a) Depending on the geometry, MOKE measurements are categorized into longitudinal, transverse, and polar. (b) Transverse MOKE setup used to measure hysteresis loops on the unpatterned and hole-array patterned samples. H indicates an applied field direction, and the incident angle θ was approximately 45° .

film was not negligible. The observed “squareness” of the $\phi = 0^\circ$ loop (Fig. 4.3) indicates that an easy axis lies near $\phi = 0^\circ$ direction rather than $\phi = 90^\circ$. The unpatterned film was approximately square-shaped, and the asymmetry between the two directions was assumed to be originated intrinsically rather than originated from the overall shape of the sample. The measured anisotropy may be originated from the sample preparation process because the sputtering source was at an angle off from

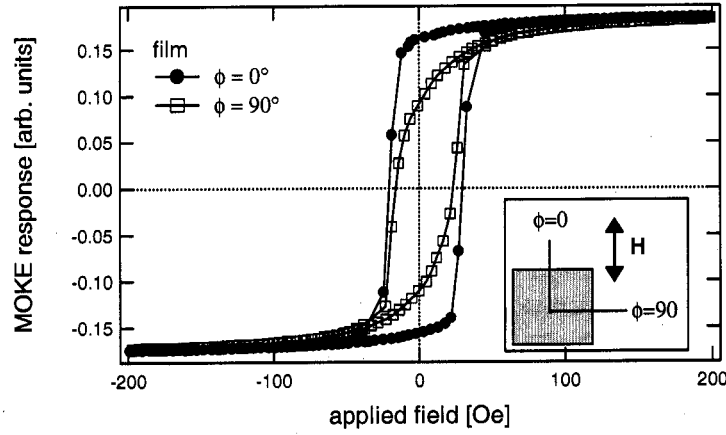


Figure 4.3. MOKE measurements on unpatterned film at $\phi=0$ and 90° where ϕ is the sample rotation angle with respect to the field \mathbf{H} . As the sample is rotated by ϕ , the incident laser and the field directions were fixed. In this geometry, the sample magnetization component parallel to the field direction is probed.

the surface normal direction. The measured intrinsic anisotropy plays an important role in the magnetic domain configuration of the hole arrays since the domain configuration is affected by the interplay between this intrinsic anisotropy and the shape anisotropy due to the patterning effect.

Since the unpatterned and the hole array patterned sample were grown simultaneously, the patterned hole array sample was expected to have similar intrinsic anisotropy. In order to determine the intrinsic anisotropy direction in the hole array, MOKE magnetization curves on the hole array were measured similarly at various sample orientations as summarized in Fig. 4.4. The shape anisotropy induced by the hole array pattern is expected to have its easy axis direction along the two equivalent diagonal directions, $\phi = 45^\circ$ and $\phi = 135^\circ$ (where square-shaped hysteresis loops would be measured). However, the measured loop at $\phi = 135^\circ$ has the most *square*

loop shape, indicating that the $\phi = 45^\circ$ and $\phi = 135^\circ$ directions are not equivalent due to the additional intrinsic anisotropy that was similarly observed in the unpatterned film (Fig. 4.3). The two hysteresis loops at $\phi=135$ and $\phi=90$ show more *squareness* than any others. From this result, it was concluded that an easy axis lies between $\phi=135$ and $\phi=90$ directions. Later, this information on the easy axis direction of the intrinsic anisotropy was incorporated in micromagnetic simulations.

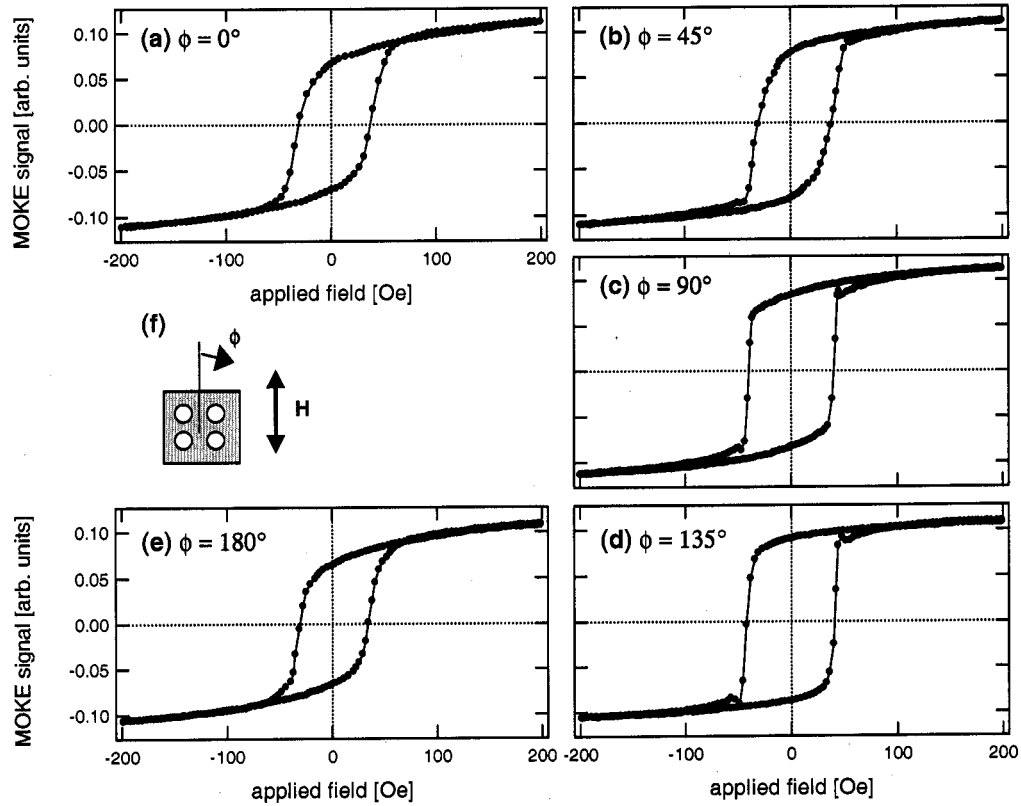


Figure 4.4. MOKE measurements on the patterned film at different ϕ angles. (a) $\phi = 0^\circ$. (b) $\phi = 45^\circ$. (c) $\phi = 90^\circ$. (d) $\phi = 135^\circ$. (e) $\phi = 180^\circ$. (f) Sample orientation with respect to the field H . The $\phi = 0^\circ$ result is equivalent to the $\phi = 180^\circ$, and the results for $\phi = 225^\circ$, 270° , and 315° were not shown here since they are equivalent to $\phi = 45^\circ$, 90° , and 135° , respectively. From this result, it was concluded that an easy axis lies between $\phi = 135^\circ$ and $\phi = 90^\circ$ directions.

4.1.2. Magnetization reversal study with x-ray techniques

Since the penetration depth of visible light in metals is typically small (≈ 20 nm), MOKE is sensitive only to the near surface layers. Subsequently, XMCD measurements on the hole array were done to study magnetization reversal process of the Fe layers. The XMCD measurements were performed as a vector magnetometry. The experimental geometry is shown in (Fig. 4.5). XMCD signal is proportional to the projection of the sample magnetization \mathbf{M} along the photon direction \mathbf{k} ($\text{XMCD} \propto \mathbf{k} \cdot \mathbf{M} \approx |\mathbf{M}| \cos \gamma \cos \alpha$), and this allows element-specific determination of the average magnetization and orientation. For the XMCD measurements, the x-ray incident angle α was 2° , and with a $2 \text{ mm} \times 2 \text{ mm}$ beam size, about 1000×5000 patterned holes were probed.

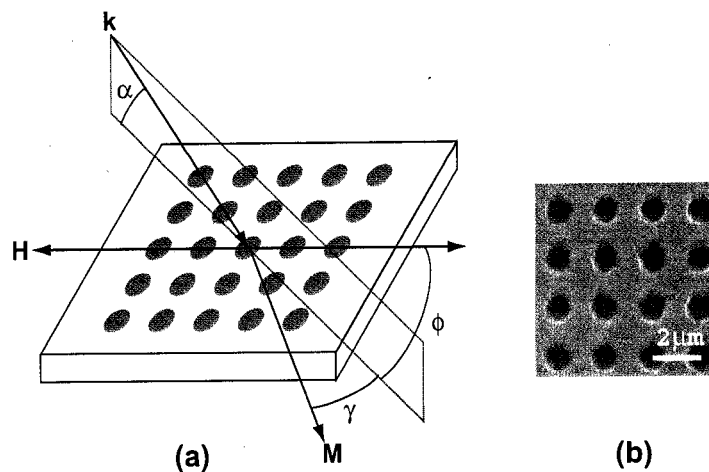


Figure 4.5. (a) Experimental geometry for XMCD vector magnetometry setup. \mathbf{k} , \mathbf{H} , \mathbf{M} represent the incoming photon momentum direction, the applied field, and the sample magnetization, respectively. α is the incident angle, γ is the angle between the magnetization and the photon direction, and ϕ is the angle between the applied field and the photon direction. (b) SEM image of the hole array.

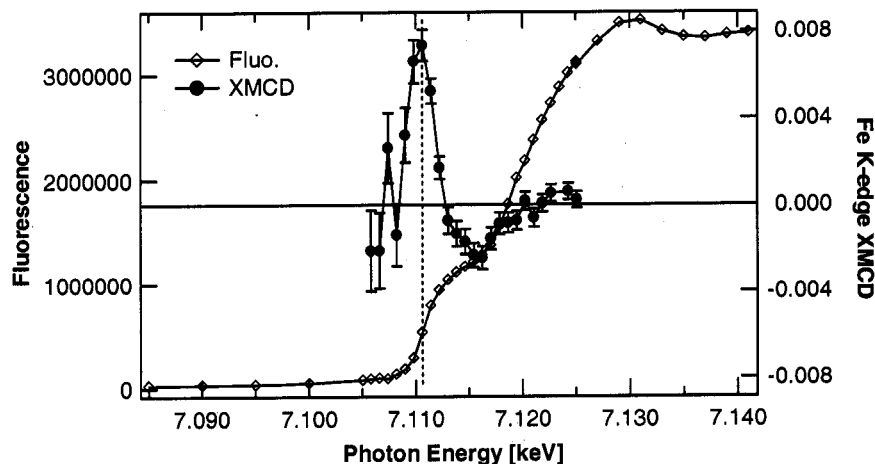


Figure 4.6. XMCD energy scan around the Fe K absorption edge. The vertical dotted line indicates where a maximum XMCD signal is observed (7.112 keV), and this energy was used for the rest of the experiments.

The XMCD measurements were performed at the 4ID-D beamline at the Advanced Photon Source. The XMCD signals were measured by monitoring fluorescence near the Fe *K* absorption edge (7.112 keV) while the helicity of the incident radiation was switched. A XMCD energy scan result is shown in Fig. 4.6. As defined in the previous chapter, the *XMCD signal* is the asymmetry ratio, $(I^+ - I^-)/(I^+ + I^-)$ where $I^{+,-}$ are the Fe- $K\alpha$ fluorescence intensities for the two opposite helicities of the incoming x-ray.

To obtain vector information on the average magnetizations from the sample, hysteresis loops were collected with more than two orthogonal incident photon directions for each field [59]. Magnetization hysteresis loops were measured at four different angles (ϕ) between the incident photon direction (\mathbf{k}) and the applied field direction

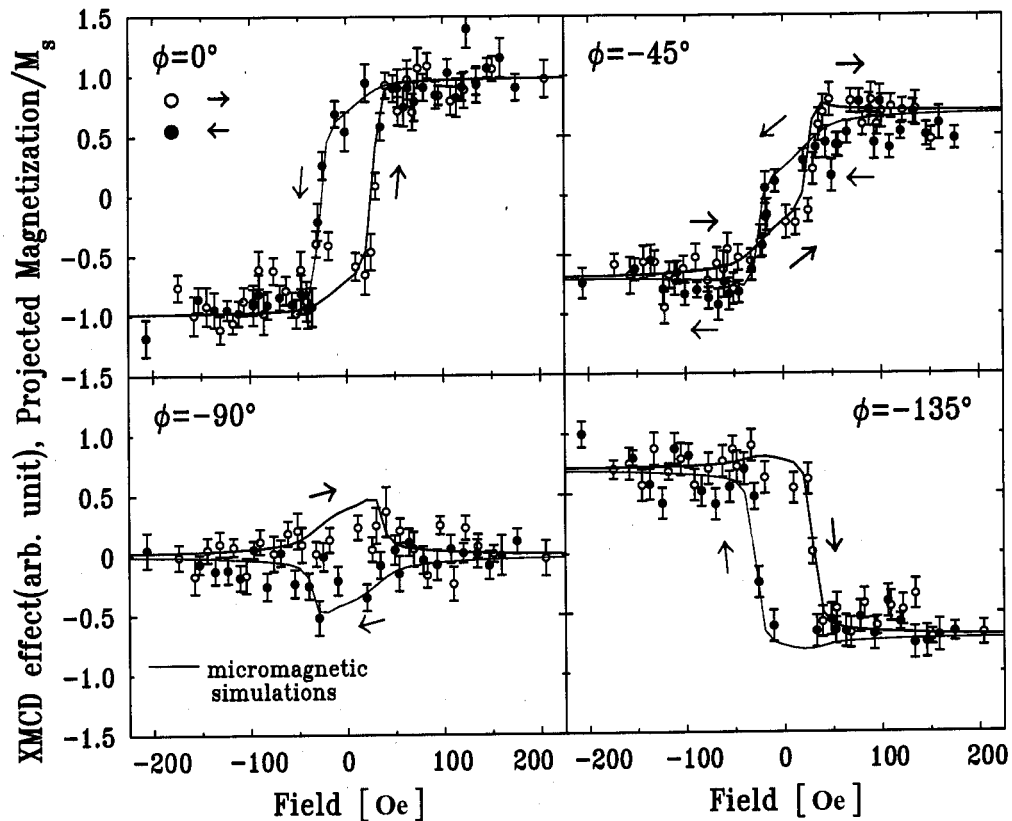


Figure 4.7. For the four different ϕ geometries, the XMCD experimental results are shown as the symbols, and the micromagnetic simulation results are shown as the lines. Micromagnetic simulation method is described in detail in **Appendix D**.

(H) as shown in Fig. 4.5. XMCD results for $\phi=0^\circ$, -45° , -90° , and -135° are shown in Fig. 4.7.

At $\phi=0^\circ$, -45° , -90° , and -135° , the alignment of the ϕ was checked by measuring θ -rocking curves from the hole arrays. The in-plane periodicity of the hole arrays can be calculated from the distance between the two satellite peaks in the rocking scans

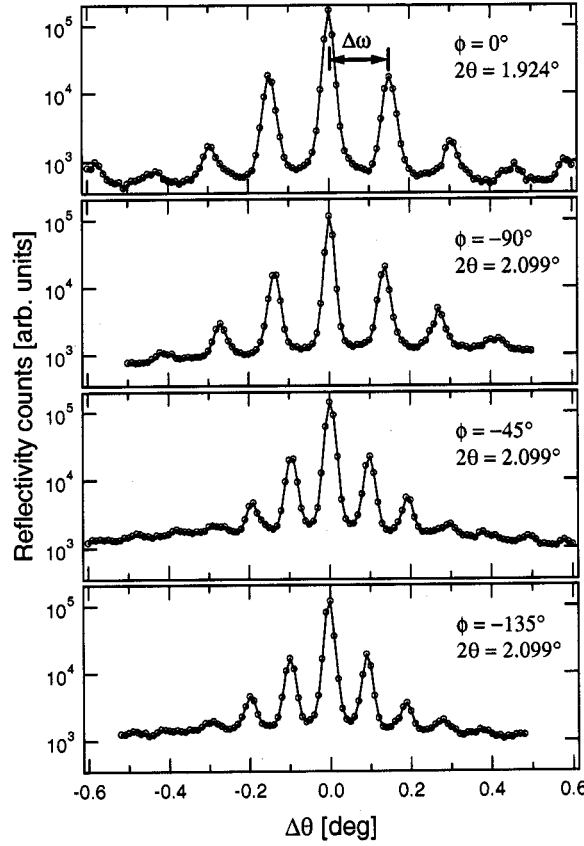


Figure 4.8. θ -rocking scans at $2\theta \approx 2^\circ$ with $\phi=0, -90, -45$, and -135° . $\Delta\theta = \theta - 2\theta/2$. The peaks in these rocking curves are due to the in-plane periodicity of the hole array.

as shown in Fig. 4.8. The periodicity was calculated using the equation [60],

$$(4.1) \quad d = \frac{2\pi}{\Delta q_x} = \frac{4\pi}{\lambda} \sin\left(\frac{2\theta}{2}\right) \sin \Delta\omega,$$

where $\Delta\omega$ is a satellite peak distance as shown in Fig. 4.8, and λ is the x-ray wavelength. Using $\Delta\omega$ values from Fig. 4.8, the periodicity d was 2.004, 2.003, 2.822, and 2.854 μm , for $\phi=0, -90, -45$, and -135° respectively. This calculation served as a check for the ϕ alignment since the in-plane periodicity depends on the ϕ angle. Since the

holes are in a square array, the in-plane periodicity would reach a maximum when $\phi=-45^\circ$ and -135° and reach a minimum when $\phi=0^\circ$ and -90° .

4.1.3. Micromagnetic simulation on the hole arrays

While XMCD measurements were used to obtain spatially averaged magnetization, micromagnetic simulations were performed to reconstruct microscopic magnetic domain configuration of the Fe layers. The simulations were performed using OOMMF program from NIST [61], and the same hole array geometry was used in these two-dimensional simulations. The hysteresis loops were calculated using micromagnetic simulations and were compared with the experimental data from the XMCD measurements.

The varied parameters in the simulations were the uniaxial anisotropy, exchange constant, and saturation magnetization. A uniaxial anisotropy constant $K_u=500$ J/m³ was used for the best fit to the XMCD measurements, and the bulk values are used for the saturation moment and the layer exchange constant so that $M_S(\text{Fe})=1700$ emu/cm³ and $J_{Fe}=2.1$ $\mu\text{erg}/\text{cm}$. The measured XMCD hysteresis loops were reproduced best with the easy axis of the anisotropy at 100° away from the applied field direction (the field direction is the probing direction in both of the MOKE and XMCD measurements). This angle is consistent with the results from the MOKE measurements (Fig. 4.4). The in-plane cell size was 20×20 nm², and the equilibrium configuration was assumed to be reached when the torque $|M \times H|/M_S^2 \leq 10^{-4}$. The thickness of the film was 3 nm, corresponding to the individual Fe layer instead of the total thickness of Fe layers. This suggests that the Fe layers are isolated from each

other by the neighboring Gd layers that are expected to be mostly paramagnetic at room temperature.

To compare with the XMCD hysteresis loops, the average magnetization values projected along the ϕ directions were calculated by averaging the projected magnetization of each cell, as $[\sum \mathbf{M}_{cell}(\mathbf{H}) \cdot \mathbf{k}_{Ph}(\phi)]/n$, where n is the number of cells. The simulation results are plotted along the XMCD experimental results in Fig. 4.7, and the both results are in good agreement.

The sensitivity of the anisotropy strength and thickness to the calculated hysteresis loops were investigated as shown in Fig. 4.9. For comparison, Fig. 4.7 was re-plotted in Fig. 4.9(d). For this simulation, the intrinsic uniaxial anisotropy was $K_u=500 \text{ J/m}^3$ and the thickness was 30 nm, as described before. Only one parameter was varied for these simulations while others were kept the same. The strength of the intrinsic anisotropy was varied to study how sensitive this parameter is to magnetization hysteresis loops of the hole array. If the intrinsic anisotropy is excluded, the magnetization component perpendicular to the field direction ($\phi = -90^\circ$) disappears as in Fig. 4.9(a). As the anisotropy is increased by an order of magnitude, the perpendicular component ($\phi = -90^\circ$) becomes too large and the tie points in ($\phi = -45^\circ$) cannot be reproduced in the simulation as illustrated in Fig. 4.9(b). In Fig. 4.9(c), a micromagnetic simulation result with increased film thickness is shown (40 nm instead of 30 nm). In this case, the switching field is too large so that most of features in the XMCD results are not reproduced.

Spin configuration obtained from the micromagnetic simulations are shown in Fig. 4.10 where the three characteristic domains, labelled as A , B , and, C are identifiable. Fig. 4.10(a) shows three spin configurations near remanence, and Fig. 4.10(b) shows the magnetization orientations of the three domains while the applied field changed from positive to negative values. While the domains B and C rotates coherently, the domain A is pinned showing a sudden change of orientation between 0~50 Oe. As the applied field decreases the domain C starts to orient toward 90° gradually, but the domain A stays pinned to the field direction.

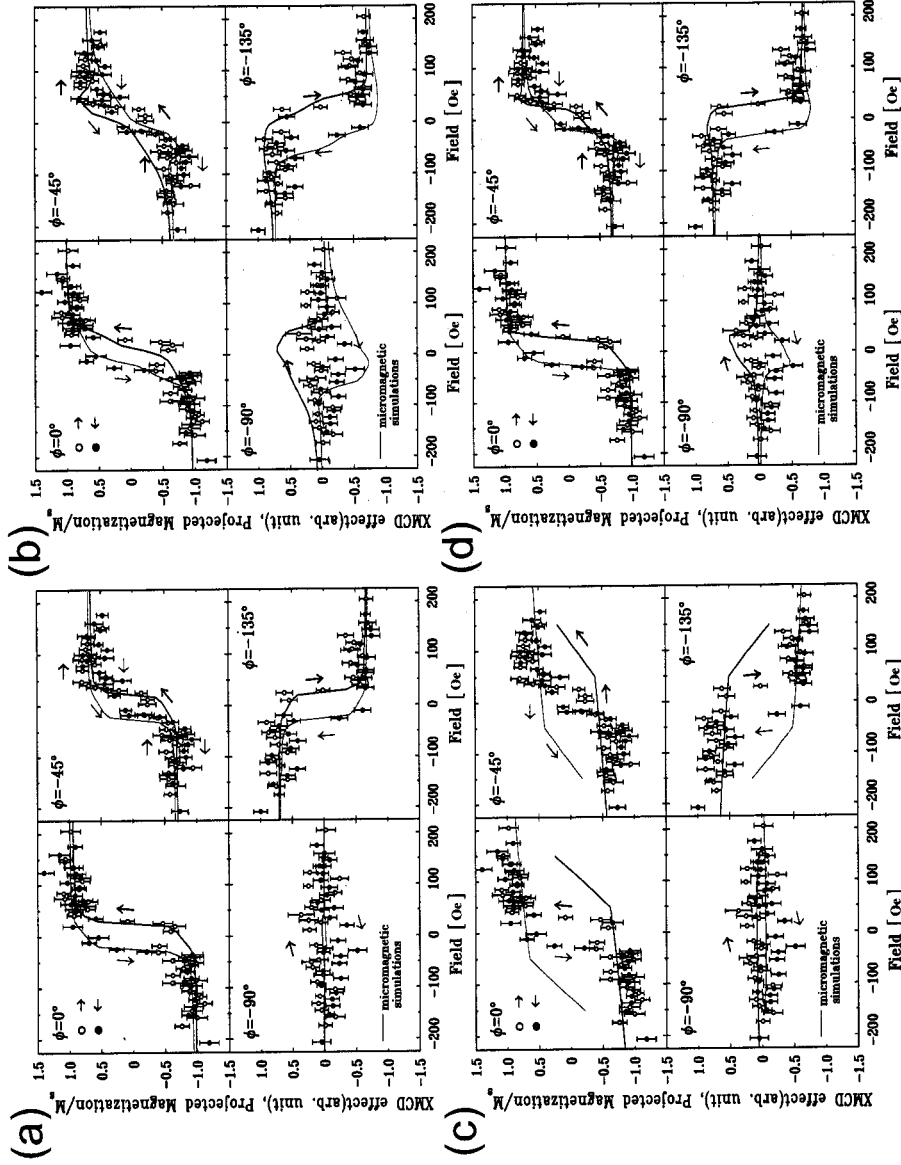


Figure 4.9. The XMCD measurement results are shown as symbols and the micromagnetic simulation results are shown as lines. (a) Simulation results with no intrinsic anisotropy. (b) Simulation results with an increased intrinsic anisotropy ($K_u=5000 \text{ J/m}^3$). (c) Simulation results with a layer thickness of 40 nm instead of 30 nm. (d) For comparison, Fig. 4.7 was re-plotted

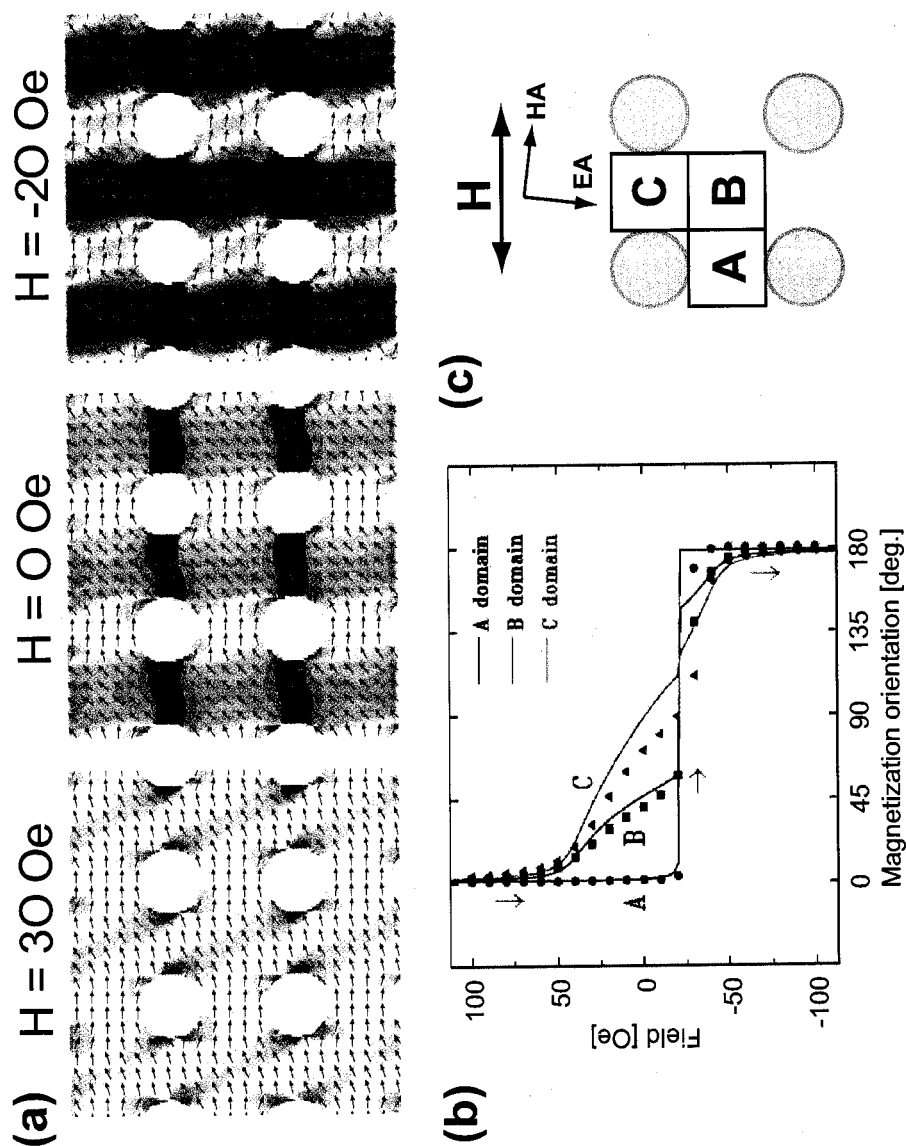


Figure 4.10. (a) Spin configurations of the hole array from micromagnetic simulation at three different fields, 30, 0, and -20 Oe. (b) Magnetization orientations for the domains, A, B, and C from the micromagnetic simulations (symbols) and from the three domain model energy calculation (lines). (c) Schematic showing three characteristic domains (A, B, and C), the applied field direction (H), and the easy/hard axis (EA , HA).

4.1.4. A phenomenological energy calculation with three domain model

To understand the rotations of the domains intuitively, a phenomenological energy calculation was performed. In this calculation, the Stoner-Wohlfarth single domain model with an effective shape anisotropy was employed [62], and it was assumed the unit cell contained only three simple types of domains [domain A, B, and C as in Fig. 4.10(c)] with the magnetization directions of which are defined by θ_A , θ_B and θ_C , respectively. It was assumed that the contributions from dipole interactions between each domain and domain wall energies at the boundaries are negligible. This assumption is proved to be reasonable since the final calculation output was not changed when these effects were included.

The total magnetic energy density of the system is then given as:

$$(4.2) \quad E_{\text{tot}} = - \sum_{i=A,B,C} \left[M_s H \cos(\theta_i - \theta_H) + K_u \cos^2(\theta_i - \theta_E) \right] + E_{\text{shape}},$$

where M_s is the saturation magnetization, H is the magnitude of the applied field and θ_H is its orientation, and K_u is the intrinsic uniaxial anisotropy constant and θ_E is the orientation of its easy axis. The uniaxial anisotropy direction was in the direction that was determined from the MOKE and the micromagnetic simulation results earlier. While the first and second terms in Eq. 4.2 represent the typical Zeeman and uniaxial anisotropy energies, respectively, E_{shape} is the total self-demagnetization energy (or the shape anisotropy, generally) ascribed to the hole arrays. Since the free pole density is proportional to the component perpendicular to the boundary surface, E_{shape} can

be expressed phenomenologically as:

$$(4. \mathfrak{E})_{\text{shape}} = N_{\text{eff}} \frac{M_s^2}{2\mu_0} \left[\sin^2 \theta_A + (\cos \theta_A - \cos \theta_B)^2 + \cos^2 \theta_C + (\sin \theta_B - \sin \theta_C)^2 \right],$$

where μ_0 is the permeability of free space, and N_{eff} is the effective demagnetization factor that was treated as an adjustable parameter.

Substituting Eq. 4.3 into Eq. 4.2, the magnetization directions of each domain in static equilibrium can be obtained by the following conditions: $\partial E_{\text{tot}}/\partial \theta_i = 0$ and $\partial^2 E_{\text{tot}}/\partial \theta_i^2 > 0$. The solutions for θ_i were superimposed on the data from micromagnetic calculations, as shown in Fig. 4.10(c).

Despite the assumed simplicity of the model, the calculation shows good agreement with the micromagnetic simulation results in Fig. 4.10(b). This strongly suggests that the interplay between the shape anisotropy and the intrinsic uniaxial anisotropy can explain the coherent rotations of domains as well as characteristic domain formations in the hole array. As the applied field decreases, while the domain C starts to rotate to 90° , minimizing both shape and intrinsic anisotropy energy, the domain A prefers to align to the field direction due to relatively stronger shape anisotropy exerted on it. A compromise between A and C domains leads to an energetically favorable domain configuration at remanence, i.e., $\theta_A \sim 0^\circ$, $\theta_B \sim 45^\circ$, and $\theta_C \sim 90^\circ$, as shown in Figs. 4.7 and 4.10.

4.1.5. Conclusion

In conclusion, the coherent rotations of the domains in a laterally confined magnetic film during a magnetic reversal process were studied by a combined approach

of XMCD-vector magnetometry measurements and micromagnetic simulations. The observed results were explained using a simple three-domain model [63]. The characteristic domains were the result of the interplay between the shape anisotropy induced by patterning and the intrinsic anisotropy.

4.2. Pseudo-spin-valve wire

Ferromagnetic film layers separated by a nonmagnetic spacer layer have been intensely studied because they exhibit a variety of effects such as giant magnetoresistance, tunnel magnetoresistance, and spin polarization of a nonmagnetic spacer layer. In a pseudo-spin-valve (PSV) structure, a conducting nonmagnetic layer is sandwiched between two magnetic layers with different coercivities. The electrical resistance in such layered materials can vary greatly depending on the relative magnetization orientation (parallel/antiparallel) between the two magnetic layers (the giant magnetoresistance effect). Using this effect, these structures have been considered as potential candidates for nonvolatile storage devices [64].

Local magnetization was studied in a submicron wire with pseudo-spin-valve (PSV) structure, Py(10 nm)/Cu(5 nm)/Co(10 nm)/Si with an Au capping layer (3 nm) on top of the Py layer. Here *Py* stands for permalloy ($\text{Ni}_{80}\text{Fe}_{20}$). The layers were patterned into a wire with two different widths connected by a narrow channel. Compared with a simple PSV wire pattern that has only two different magnetization orientations (parallel/antiparallel), the PSV wire pattern with two sections can have more than two magnetization orientations due to the different shape anisotropy in each section.

Many interesting magnetic systems that are composed of alloyed or heterostructured multilayer films, and the PSV structure is one of such system. In these heterostructured structures it becomes important to learn about individual constituents in a layer-specific or element-specific way. Commonly used probing methods, such as MOKE, magnetoresistance, and SQUID, measures the overall response from the whole system. For an element-specific magnetism study, x-ray magnetic circular dichroism (XMCD) was used in this work. XMCD measurements were performed in fluorescence geometry, and the penetrating capability of hard x rays enables magnetism studies from buried structures. XMCD signals were used to provide layer-specific magnetization information, and with a micro-focused x-ray beam, local magnetization information was obtained.

4.2.1. Local Magnetization Measurement

A PSV wire [Au(3 nm)/Py(10 nm)/Cu(3 nm)/Co(10 nm)] on a Si substrate was made by a combination of e-beam lithography, e-beam evaporation, and lift-off processes. The top Au layer was deposited to prevent oxidation. The wire was patterned into two sections with different widths (0.6, 0.3 μm), connected by a tapered narrow section (0.1 μm) that acts as a domain wall trap [65] (Fig. 4.11).

To probe local magnetization from two different sections with different widths, XMCD measurements were performed on the PSV-wire with micro-focused x-ray beam. At the sample position, the circularly polarized beam was focused down to 1.5 $\mu\text{m} \times 1.5 \mu\text{m}$ using focusing mirrors in Kirkpatrick-Baez geometry [66] as described in Fig. B.8 in **Appendix B**. In addition, by tuning the incoming x-ray energy to

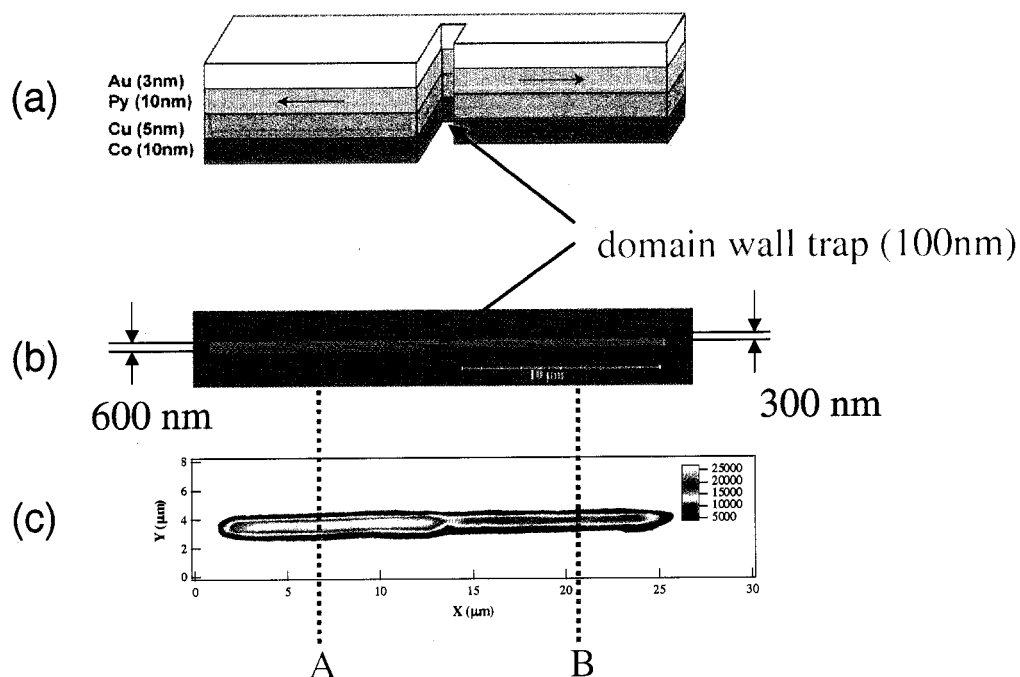


Figure 4.11. A pseudo-spin-value structure patterned into a wire shape. (a) A schematic of the layer structure. (b) SEM image of the structure. (c) Co $K\alpha$ fluorescence signal mapping. Hysteresis loops were measured at A and B.

absorption energies of the two different layers, magnetization reversal processes of the soft and hard layer were investigated separately.

Fluorescence from the sample was collected by energy dispersive Ge solid state detectors, and a magnetic field was applied along the sample using an electromagnet. By tuning the incoming photon energy to near absorption edges of each constituent element, the magnetization reversal processes of the soft (NiFe) and hard layer (Co) can be investigated separately.

The incoming x-ray energy was first tuned to near the Co K edge, and dichroic x-ray absorption spectra were taken to find the energy with the maximum XMCD

signal (7.713 keV). Here the *XMCD signal* is the asymmetry ratio, $(I^+ - I^-)/(I^+ + I^-)$ where $I^{+,-}$ are the Co- $K\alpha$ fluorescence intensities for the two opposite helicities of the incoming x-ray. The homogeneity of the buried Co layer was mapped by moving the sample on a micro-stage and monitoring the Co $K\alpha$ fluorescence as shown in Fig. 4.11. The hysteresis measurement from the Co layer was obtained by monitoring the XMCD signal while sweeping an applied magnetic field. The magnetization of the bottom Co layer, which is below Au/permalloy/Cu layers, can be deduced from the Co XMCD signal. Two separate hysteresis loop measurements were done at the point *A* and *B* as indicated in Fig. 4.11. The XMCD hysteresis loops for the Co layer are shown in Fig. 4.12(a). The hysteresis loop for the thin section shows a larger switching field than that of the thick section.

Subsequently, similar XMCD measurements at the Ni and Fe K edges (7.112 and 8.333 keV respectively) were performed on the permalloy ($\text{Ni}_{80}\text{Fe}_{20}$) layer. However, the lower Fe content in this layer on one hand, and the reduced XMCD signal at the Ni K -edge of NiFe relative to other Ni concentrations on the other [67], resulted in noisier data at these edges. This problem, however, can be overcome at Fe and Ni L -edges, as shown by Castaño et al [68].

4.2.2. Micromagnetic simulation

Micromagnetic calculations on the PSV-wire system were performed using OOMMF program [61]. In a system where two ferromagnetic layers are separated by a nonmagnetic spacer layer, the interlayer coupling effects, such as Ruderman-Kittel-Kasuya-Yoshida (an indirect exchange mediated by the electrons in the nonmagnetic layer)

[69] and Neel's orange peel coupling (a magnetostatic effect due to correlated roughness) [70], could play a significant role. However, because of the thick Cu layer between the permalloy and Co layers, the interlayer coupling effects were assumed to be not significant here. It was also assumed that in each layer, the magnetization is uniform in the out-of-plane direction, allowing for two-dimensional simulations. The simulation cell size was $20\text{ nm} \times 20\text{ nm}$, and the equilibrium configuration was assumed when $|M \times H|/M_S^2 \leq 10^{-5}$ was reached. From the simulations, the hysteresis loop for the thin (thick) section was obtained by averaging the projected magnetization of the cells that are in the thin (thick) section. The simulation results for the Co layer are shown in Figs. 4.12(b)-(c). The experimental results are in good agreement with the simulation results [Figs. 4.12(a)-(b)].

Figure 4.13(b) shows four calculated hysteresis loops of thin and thick sections from each layer by OOMMF program. The field values of the upper loops at which domain schematics were drawn in Fig. 4.13(a) are designated $h1 \sim h5$. These schematics represent magnetic domain configuration from the micromagnetic simulation results. Initially the whole sample is magnetized to the left ($h1$). As the field direction is reversed, the permalloy magnetization of the thick section is reversed first ($h2$). This is expected since permalloy is magnetically soft compared with Co, and the shape anisotropy of the thick section is lower than that of the thin section. The connecting narrow section in the middle acts as a barrier preventing domain propagation, i.e., a domain wall trap. As the field is increased in the reverse direction, the Co magnetization of the thick section ($h3$) is reversed. The domain wall in this Co layer is also in the connecting narrow section. As the applied field is increased further, the

field is strong enough to overcome the domain wall trap barrier, and the permalloy magnetization of the thin section (h_4) is reversed next. The magnetization of both layers is reversed at higher field eventually (h_5).

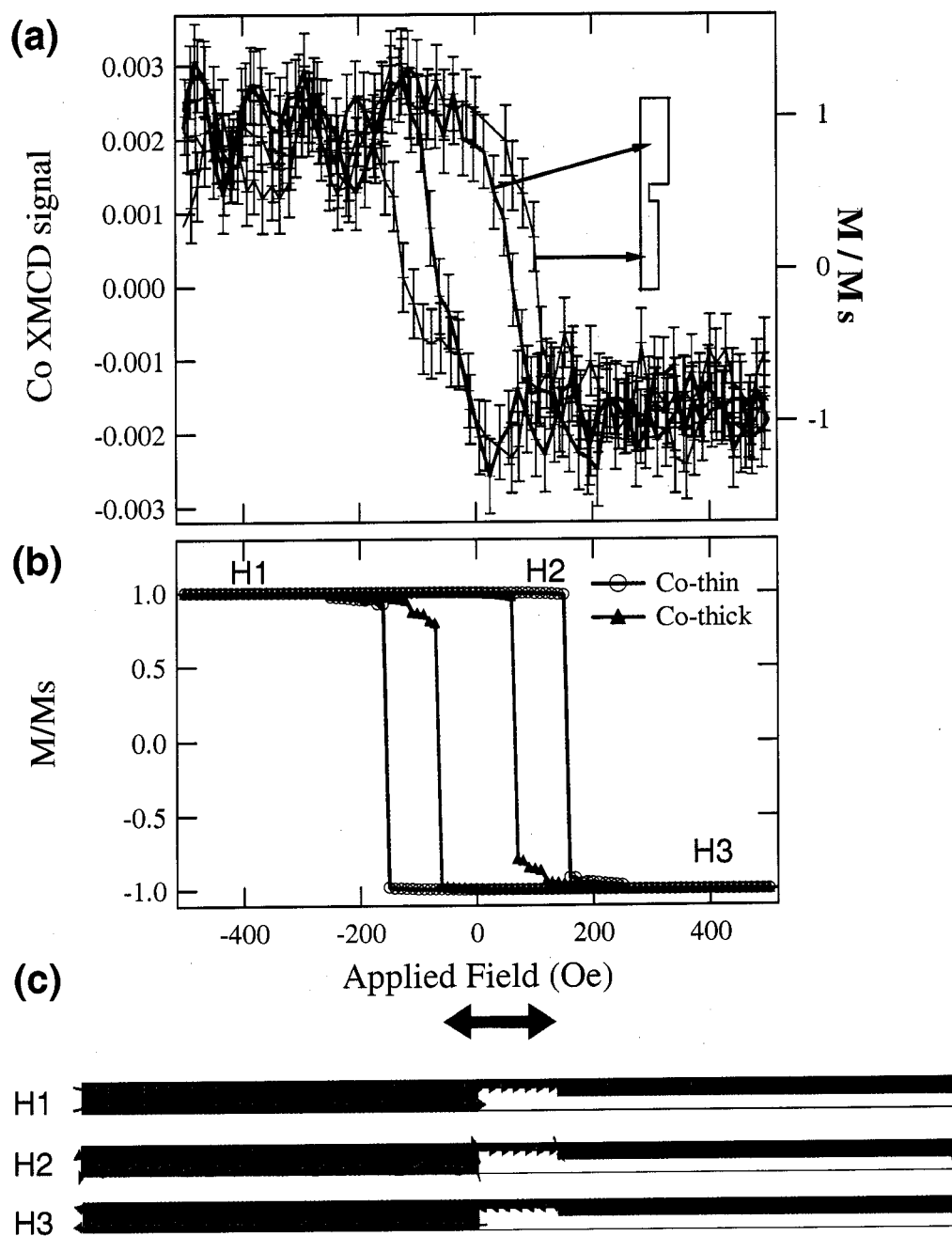


Figure 4.12. (a) XMCD hysteresis loops measured from the buried Co layer. (b) Micromagnetic simulations on the Co layer. (c) Three spin configurations at different field values (H1-H3), from the Co simulation results.

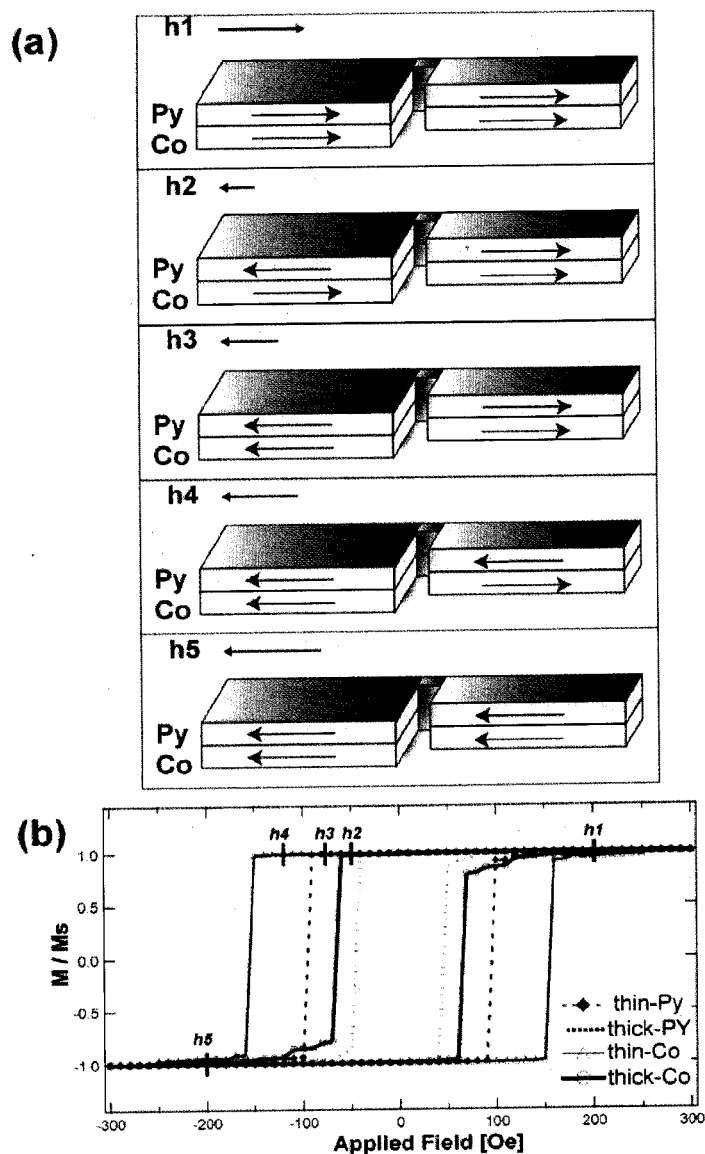


Figure 4.13. (a) Micromagnetic simulations results on Co and permalloy layers. For each layer, two hysteresis loops, corresponding to the thin and wide sections, are shown. (b) Magnetization orientation schematics from micromagnetic simulation. The Au and Cu layers are not shown. The arrows inside the films indicate layer magnetization directions. $h1 \sim h5$ refer to their respective fields on the hysteresis loops from micromagnetic simulation in (a).

4.2.3. Conclusion

In conclusion, element-specific hysteresis loops were measured from the buried Co layer in a PSV system that is patterned into a wire-shape. It was shown that the two sections of different widths can be isolated by having a domain wall trap in between. As a reversing field is applied, the thick section reverses its magnetization while the thin section retains its magnetization. The domain wall trap in the middle prevents domain propagation from the thick section to the thin section. The XMCD measurements show that the two sections have different switching fields. This result was simulated using a micromagnetic simulation program, and the experimental results. The simulation result also shows that a single pattern can have more than two magnetization orientations depending on the applied field strength.

CHAPTER 5

Structural and magnetic characterization of Co dot arrays using soft x-ray resonant magnetic scattering

Recently, because of their fundamental interest and potential applications, periodic arrays of magnetic nanostructures have received much attention. These patterned nanostructures exhibit unique properties that are different from their continuous film counterparts. The patterning modifies the magnetization dynamics of the magnetic medium, and this magnetization dynamics are typically studied by monitoring magnetic responses from a sample while varying external parameters such as changing an applied field in direction, magnitude, and time. The unique properties of the magnetic nanostructure arrays heavily depends on their structural parameters such as size, shape, and spacing [71]. For structural studies of these magnetic arrays, scanning electron microscopy and atomics force microscopy are typically used. These scanning techniques are predominantly used as local probes, providing bulk sensitivity. In this chapter, structural and magnetic characterization of Co dot arrays are described using polarized soft x rays in order to get depth-dependent information that may not be obtained using other conventional probing techniques.

5.1. Experiments

A square array of disk-shaped Co dots was fabricated on a Si-substrate using e-beam lithography and lift-off processes. The nominal thickness of the dots are 30 nm, and the Co dots with a diameter of 1 μm were made with 2 μm spacing [Fig. 5.1(a)]. The sample size was about 1 cm \times 1 cm, and the entire area was covered with the pattern.

To probe magnetic structure of the Co dot arrays, soft x-ray resonant magnetic scattering (SXRMS) [72] measurements were conducted in the low angle specular reflectivity mode. The scattering measurements were performed at the beamline 4ID-C of the Advanced Photon Source at Argonne National Laboratory. Polarized x rays were generated by a novel circularly polarizing undulator at the beamline [73]. The photon energy was tuned to the Co L_3 absorption edge (778.1 eV) to enhance the magnetic sensitivity. At this x-ray energy, the absorption by air is not negligible so that the entire scattering setup has to be kept inside a vacuum chamber. Inside the vacuum chamber, diffracted intensities were collected by a Si photo-diode detector on the 2θ -arm as the 2θ -arm and the sample stage were rotated. The scattering geometry and the applied magnetic field direction is illustrated in Fig. 5.1(b). The applied field direction is in the scattering plane, and using this setup and circularly polarized x rays, the magnetization component parallel/antiparallel to the applied field is probed.

To find the energy where magnetic contrast is maximized, x-ray absorption spectra were measured across the Co L_3 absorption edge with left- and right-circularly

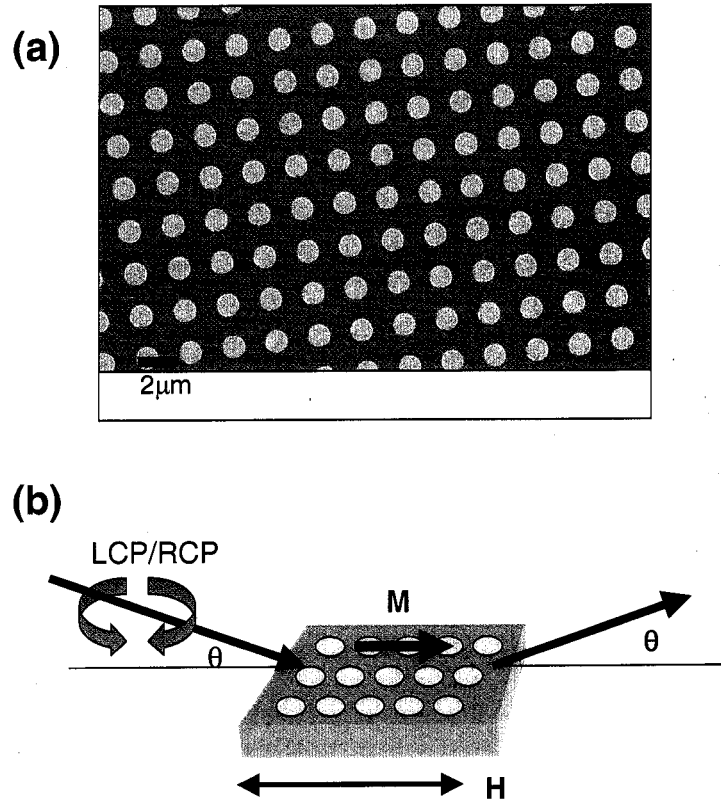


Figure 5.1. (a) SEM image of a Co dot array. (b) Scattering geometry for soft x-ray resonant magnetic scattering. LCP(RCP) represents left(right) circularly polarized x rays. M : magnetization component probed; H : applied field; θ : incident angle. The field H was applied along the nearest-neighbor direction and in the scattering plane. The maximum field applied was ± 650 Oe.

polarized x rays, as shown in Figs. 5.2(a),(b). An electromagnet was used to apply the magnetic field. With the incoming x rays of right-circular polarization, the magnetic field direction was switched back and forth, and the difference in the reflected intensities between the two opposite field directions was collected. Subsequently, the polarization was switched to left-circular polarization and the difference in the reflected intensities between the two opposite field directions was collected

again. Assuming the maximum field is strong enough to magnetically saturate samples [Fig. 5.2(c)], this procedure can remove artifacts in the XMCD signals. Thus the *difference signal* is defined as $\Delta I = [(I^{++} - I^{+-}) - (I^{-+} - I^{--})]/2$ where the first and second superscripts stand for the x-ray helicity (RCP/LCP) and the applied field direction (parallel/antiparallel), respectively. Similarly, the *sum signal* is defined as $I_{sum} = [(I^{++} + I^{+-}) + (I^{-+} + I^{--})]/2$. The maximum contrast between the two polarizations was measured at 775.9 eV in the XMCD scan [Fig. 5.2(a)-(b)]. The incident energy was fixed to this energy for the angle-dependent reflectivity measurements as shown in Fig. 5.2(d)-(e). The reflectivity in the sum channel is due to the electron density variation of the sample in the depth direction (thus called *charge reflectivity* herein), and the reflectivity in the difference channel is due the interference between the charge and magnetic density variations (thus called *charge-magnetic reflectivity* herein).

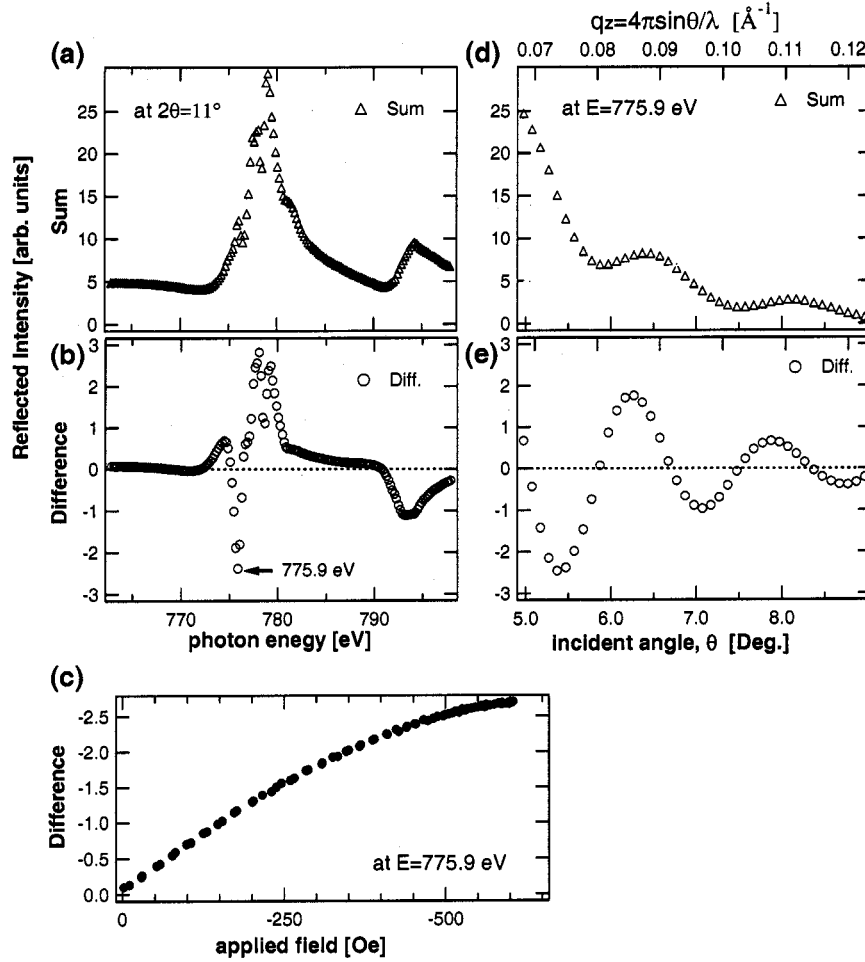


Figure 5.2. (a)-(b) X-ray absorption and XMCD spectra near the Co L_3 absorption edge from the Co dot sample. Reflected intensities as a function of the incident x-ray energy was plotted. Sum (a) and difference (b) between the intensities for the two polarizations. The applied field was ± 650 Oe. (c) A magnetization curve of the Co dot was measured by monitoring dichroic signal as a function of the applied field at the incident photon energy of 775.9 eV where the maximum contrast was observed. Near $H=-650$ Oe, the magnetization curve becomes almost flat, indicating the Co dots are nearly saturated along the field direction. (d)-(e) Reflected intensities as a function of the incident angle at the incident photon energy 775.9 eV with the applied field of -650 Oe. Due to the limited range of the 2θ -arm motion, the angular range was $5^\circ < \theta < 9^\circ$.

5.2. Analysis and Discussion

To analyze the reflectivity data, the “density-profile approximation” was employed. For the analysis of x-ray reflectivity from laterally structured surfaces, Tolan *et al.* [74] developed this approximation in which the electron density of gratings were approximated by geometrical averaging of optical constants based on the area coverage ratio. Here this approximation is extended to a two dimensional structure. This approximation is valid only if the coherence of x-ray is much larger than the lateral periodicity, and the coherence at the beamline 4ID-C is expected to be much larger than $2\ \mu\text{m}$.

The sample was covered with the dot patterns entirely, and within illuminated area approximately 2.0×10^6 dots were probed in the reflectivity measurements, as illustrated in Fig. 5.3(a). Within the unit cell, the coverage ratio was $\pi/16$ as shown in Fig. 5.3(b). Assuming the structural uniformity along the depth direction, the dots are approximated to be disks. At a given depth z , the refractive index for the dot array can be approximated as:

$$(5.1) \quad n(z) = \begin{cases} 1 & \text{for } z > t \\ 1 - \frac{\pi}{16}(\delta + i\beta)_{Co} & \text{for } 0 \leq z \leq t \\ 1 - (\delta + i\beta)_{\text{substrate}} & \text{for } z \leq 0 \end{cases}$$

where t is the thickness of the dots and n is the refractive index $n = (1 - \delta + i\beta)$. For the reflectivity calculation, the resonant optical constants that were obtained from measurements on a standard Co film were used.

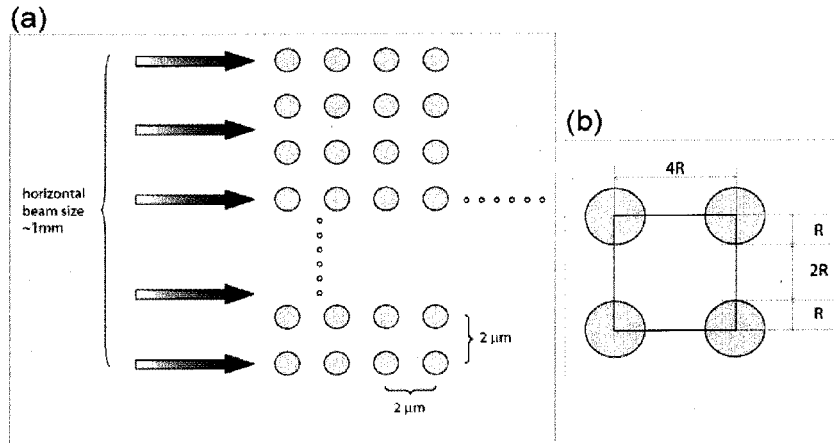


Figure 5.3. (a) Geometry for x-ray scattering measurements on the Co dot array. The beam size is about 1 mm×1 mm, and for $5^\circ < \theta < 9^\circ$, the illuminated area is calculated to be about 1 mm×6.4~11.5 mm. The corresponding number of dots illuminated is about 1.6~2.9 million dots. (b) The coverage area ratio of the Co is calculated to be $\pi R^2/(4R)^2 = \pi/16$.

Base on this approximation and using the distorted-wave Born approximation (DWBA) for magnetic films [32], the charge and charge-magnetic reflectivity curves are fitted as shown in Fig. 5.4. Fig. 5.5 shows the model that was used to calculate the charge and charge-magnetic reflectivity curves, and the fitted parameters are also shown. The model used here has three layers with variable magnetization values. Initially, the data was fitted with an one-layer model. The fitting with this model reproduced the charge-reflectivity data successfully, but it could not reproduce the periodicity observed in the charge-magnetic reflectivity data at all. From this result, it was concluded that the dots were not uniformly magnetized across the depth direction. With the three-layer model, the periodicity (period and positions of the peaks) of the charge-magnetic reflectivity data was reproduced reasonably well. The relative

density of the layers were constrained to be the same, and the interior layer magnetization is constrained to be one. The total thickness was fitted to be 30.47 nm, and the top (8.55 nm) and bottom (8.78 nm) layers have different relative magnetization values (relative to bulk Co). The top layer magnetization is enhanced relative to its bulk value while the bottom layer magnetization is reduced. This result is consistent with what others observed in continuous Co films [75].

It is worthwhile to discuss the model dependency of the charge- and charge-magnetic reflectivity fitting procedure. The three-layer model calculation resulted in good agreement between the calculated and measured reflectivity curves. However, this does not mean that the three-model is the unique solution, as typical in any other reflectivity fittings. The fitting can be refined more by adding more extra

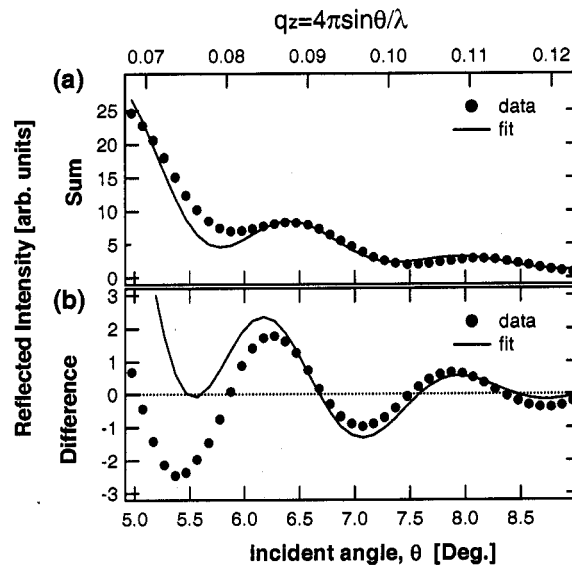


Figure 5.4. SXRMS reflectivity data and fits are plotted. The solid circles represent measured data and the lines represent fits. (a) The sum of two reflected intensities with the opposite polarizations. (b) The difference between the two reflected intensities.

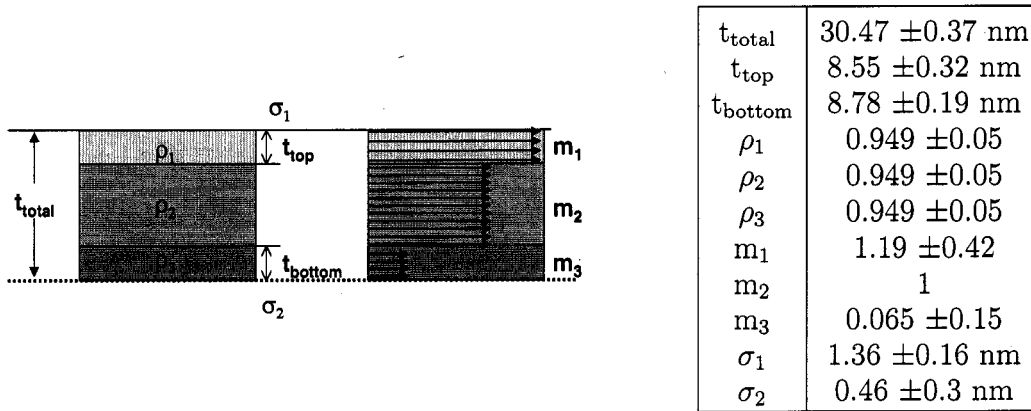


Figure 5.5. The fitted parameters and model used for the SXRMS reflectivity fit. The cross-sectional view of the Co dots is shown. ρ and m represent relative density and relative magnetization of each layer, respectively. Layer thicknesses are represented by t . σ_1 and σ_2 are the effective rms roughnesses for the air-Co and Co-Si interfaces respectively.

layers in the model, but with the limited angular (q_z) range in this measurement, models with too many layers can be artificial. The three-layer model can be justified here since the uniformly magnetized model (one-layer model) could not reproduce the features in the charge-magnetic scattering data. Compared with the two-layer model, the three-layer model reproduced the features better, and thus the three-layer model was selected to explain the measured data.

5.3. Future Work

Using the similar approach, the pseudo-spin valve structured permalloy(Py, Ni₈₀Fe₂₀)-Cobalt dot arrays were studied. Circular dot arrays of the same lateral dimensions are made using e-beam lithography, lift-off, and e-beam deposition. One dot array was made with a Cu spacer layer in the middle (Co[30 nm]/Cu[3 nm]/Py[20 nm]/Cu [3

nm]), and another dot array was made without the spacer layer (Co[30 nm]/Py[20 nm]/Cu [3 nm]). The effect of the spacer layer in the middle was studied by measuring element-specific (thus layer-selective) XMCD-magnetization hysteresis loops and soft x-ray resonant magnetic scattering (SXRMS) in reflectivity mode. The hysteresis loops can give field-dependent information from each layer, and the SXRMS data can give magnetic depth profiles of each layer. The dot structure and hysteresis loops are shown in Fig. 5.6. The measurements were performed at the beamline 4ID-C of the Advanced Photon Source at Argonne National Laboratory. With circularly-polarized x rays, reflected intensities from the dot array samples were collected as the applied field was changed. The Fe hysteresis loops (probing the permalloy, $Ni_{80}Fe_{20}$ layer) were collected with the incident x-ray energy at the Fe- L_3 edge, and the Co loops were measured with the incident x-ray energy at the Co- L_3 edge. Without the spacer layer, the Fe loop follows the trend of the Co loop [Fig. 5.6(b)]. However, with the Cu spacer layer, the field-dependence of the permalloy layer is changed [Fig. 5.6(a)].

In order to study the interfacial layers near the spacer layer in the permalloy and Co layers, SXRMS measurements in reflectivity mode were conducted Fig. 5.7. On each sample, SXRMS reflectivity measurements were performed at the Fe and Co absorption edges with circularly polarized x rays. While the charge reflectivity curves (sum-channel) can give structural information in the depth direction, the charge-magnetic reflectivity curves (difference-channel) can give magnetic information as demonstrated for the Co dot arrays earlier in this chapter. All of the SXRMS measurements here are sensitive to the structural properties, but with the incident x-ray near the Fe- L_3 , the charge-magnetic reflectivity curves are sensitive to the permalloy

(Ni₈₀Fe₂₀) magnetic properties only. Similarly, with the charge-magnetic reflectivity curves measured near the Co- L_3 absorption edge are sensitive to the Co layer magnetization but not to the permalloy layer magnetization.

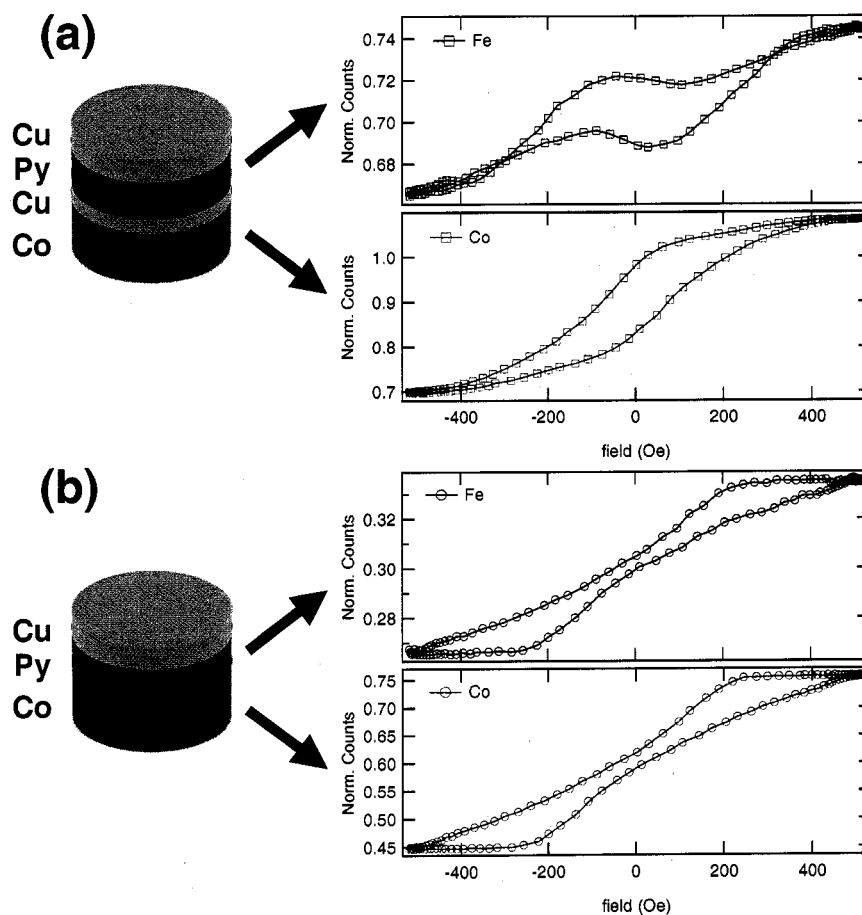


Figure 5.6. Layer selective magnetization hysteresis loops from the permalloy(Py, $\text{Ni}_{80}\text{Fe}_{20}$)-Cobalt dot arrays with and without a spacer layer. (a) Fe and Co XMCD hysteresis loops from the Co/Cu/Py dot array. (b) Fe and Co XMCD hysteresis loops from the Co/Py dot array.

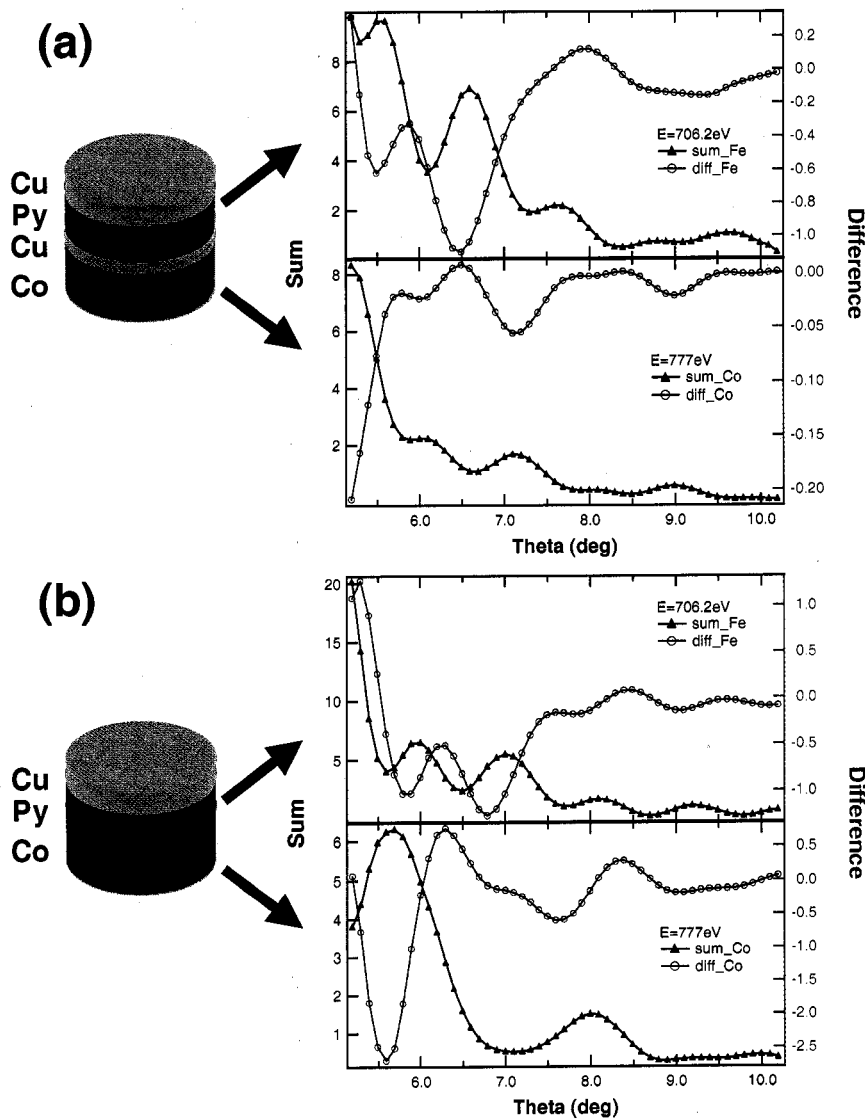


Figure 5.7. SXRMS reflectivity data from the permalloy(Py, Ni₈₀Fe₂₀)-Cobalt dot arrays with and without a spacer layer. On each sample, SXRMS measurements were done at the Fe and Co absorption edges to obtain magnetic depth profiles in the permalloy and the Co layers, respectively. (a) SXRMS reflectivity data from the Co/Cu/Py dot array at the Fe-edge (top) and at the Co-edge (bottom). (b) SXRMS reflectivity data from the Co/Py dot array at the Fe-edge (top) and at the Co-edge (bottom).

5.4. Conclusion

The structure and magnetization profiles of a Co dot array were studied using the soft x-ray resonant magnetic scattering. The optical constants of the Co dots were obtained by geometrical averaging following the “density profile approximation”. The charge- and charge-magnetic reflectivity curves were fitted with the magnetic DWBA calculation [32] (described more in **Chapter 2**). The fitting results show that the dots are not uniformly magnetized in the depth direction, but the top and bottom layers have different relative magnetization values compared with the magnetization of the interior. This approach was further extended to pseudo-spin-valve structured dot arrays to study how the magnetization profiles might be altered depending on the existence of a non-magnetic conducting layer in between the permalloy and Co layers. The analysis of the charge-magnetic reflectivity data is in progress.

CHAPTER 6

Conclusion

In this dissertation, the effects of interfacial coupling, proximity, anisotropy (intrinsic and shape), and termination were investigated in continuous and patterned magnetic multilayer films with an emphasis on how they affect the magnetization reversal processes and magnetization depth profiles. For element-specific magnetism studies, x-ray resonant techniques were used to achieve element-specificity and enhanced magnetic sensitivity.

First, a Gd-aligned Fe/Gd multilayer was studied using x-ray resonant scattering and absorption techniques with an emphasis on the temperature evolution of the Gd-magnetization profiles. The volume averaged magnetization values of the Gd layers were obtained using x-ray magnetic circular dichroism, and depth-resolved magnetic profiles were obtained using x-ray resonant magnetic scattering in charge-magnetic reflectivity mode. The charge-magnetic reflectivity data was analyzed using the distorted wave Born approximation, and the results were compared with the Born approximation calculation results. In this multilayer, the Gd magnetic ordering near the Fe/Gd interfaces was found to be persisting even near room temperature that is above bulk Gd Curie temperature.

Secondly, Fe/Gd multilayers with a different thickness ratio between Fe and Gd layers from that of the previous study were investigated to investigate field-induced

spin reorientation. It was found that the termination layer plays an important role in determining in-field spin configurations of these multilayers. The surface twisted state and the bulk twisted state in the Fe-terminated multilayer were observed, and these inhomogeneous magnetization states were reproduced by the micromagnetic simulations. At low temperatures, the inhomogeneous magnetic state is driven by surface twisting of the top Fe layer, and at high temperatures, the surface layers lag behind their interior counterparts in terms of canting away from the applied field direction. Near the ferrimagnetic compensation temperature, it was found that the anisotropy in the Fe layers plays an important role causing field shifting and non-reversing of the hysteresis loops. These phenomena were not observed in the similarly grown Gd-terminated multilayer, showing a termination layer effect.

Magnetic domains on patterned magnetic films were studied using x-ray magnetic circular dichroism, magneto-optical Kerr effect, and micromagnetic calculations. The magnetic dichroism measurements were performed to obtain magnetic hysteresis loops. By rotating the angle between an applied field and x-ray direction, different magnetic components in lateral directions were probed. From the Kerr effect measurements with laser light, it was found that the films have an intrinsic anisotropy, and this anisotropy was included in the simulations in addition to the shape anisotropy due to patterning. The measured XMCD hysteresis curves were then compared quantitatively with micromagnetic calculations to reconstruct the microscopic magnetization configurations. The best fit reveals the existence of three types of characteristic domains: two that rotate coherently during magnetization reversal and one that is strongly pinned.

On a wire-shaped pseudo-spin-valve structure (Co/Cu/NiFe), the separation of the two regions with different width was achieved by a lateral domain trap in the middle. With micro-focused x-ray beam, local magnetization was probed by x-ray magnetic circular dichroism measurements. Layer-specific magnetization was measured from the Co layer, but the same measurements could not be repeated for the NiFe layer due to weak fluorescence count rates. Micromagnetic simulations were also performed on the same structure, and the experimental and simulation results showed that the two regions were separated due to the presence of the domain wall trap in the middle.

Co circular dot arrays in a square lattice were studied using x-ray resonant magnetic scattering in the soft x-ray region. The charge-magnetic reflectivity data was analyzed using the distorted wave Born approximation for magnetic multilayers. From the analysis, the magnetic depth profiles of the dots were obtained, and they show that the Co dots are not uniformly magnetized in the depth direction. The extension of this approach to Co/Cu/NiFe dot arrays is in progress.

References

- [1] S. S. P. Parkin, "Origin of enhanced magnetoresistance of magnetic multilayers: Spin-dependent scattering from magnetic interface states," *Phys. Rev. Lett.* **71**, 1641-1644 (1993);
P. Beliën, R. Schad, C. D. Potter, G. Verbanck, V. V. Moshchalkov, and Y. Bruynseraede, "Relation between interface roughness and giant magnetoresistance in MBE-grown polycrystalline Fe/Cr superlattices," *Phys. Rev. B*, **50**, 9957-9962 (1994);
J. Barnaś and G. Palasantzas, "Interface roughness effects in the giant magnetoresistance in magnetic multilayers," *J. Appl. Phys.* **82**, 3950-3956 (1997);
P. Grünberg, D. E. Bürgler, R. Gareev, D. Olligs, M. Buchmeier, M. Breidbach, B. Kuanr, and R. Schreiber, "Experiments on the relation between GMR and interface roughness and on the interlayer exchange coupling across semiconductors," *J. Phys. D: Appl. Phys.* **35**, 2403-2409 (2002).
- [2] J. Nogues and I. K. Schuller, "Exchange bias," *J. Magn. Magn. Mater.* **192**, 203-232 (1999).
- [3] G. A. Prinz, "Magnetoelectronics," *Science* **282**, 1660-1663 (1998).
- [4] R. Fiederling, M. Keim, G. Reuscher, W. Ossau, G. Schmidt, A. Waag, and L. W. Molenkamp, "Injection and detection of a spin-polarized current in a light-emitting diode," *Nature* **402**, 787-790 (1999);
Y. Ohno, D. K. Young, B. Beschoten, F. Matsukura, "Electrical spin injection in a ferromagnetic semiconductor heterostructure," H. Ohno, and D. D. Awschalom, *Nature* **402**, 790-792 (1999).

- [5] S. G. E. te Velthuis, J. S. Jiang, S. D. Bader, and G. P. Felcher, "Spin Flop Transition in a Finite Antiferromagnetic Superlattice: Evolution of the Magnetic Structure," *Phys. Rev. Lett.* **89**, 127203 (2002);
C. Micheletti, R. B. Griffiths, and J. M. Yeomans, "Surface spin-flop and discommensuration transitions in antiferromagnets," *Phys. Rev. B* **59** 6239-6249 (1999);
F. Keffer and H. Chow, "Dynamics of the Antiferromagnetic Spin-Flop Transition," *Phys. Rev. Lett.* **31**, 1061 (1973).
- [6] R. W. Wang, D. L. Mills, Eric E. Fullerton, J. E. Mattson, and S. D. Bader, "Surface spin-flop transition in Fe/Cr(211) superlattices: Experiment and theory," *Phys. Rev. Lett.* **72**, 920-923 (1994).
- [7] *Ferromagnetic Materials, Volume 1*, edited by E. P. Wohlfarth (North-Holland publishing company, New York, 1980).
- [8] F. J. Himpsel, J. E. Ortega, G. J. Mankey, and R. F. Willis, "Magnetic nanostructures," *Advances in Physics* **47**, 511-597 (1998).
- [9] S. W. Lovesey and S. P. Collins, *X-ray scattering and Absorption by Magnetic Materials*, (Oxford University Press, Oxford, 1996).
- [10] J. P. Hannon, G. T. Trammell, M. Blume, and Doon Gibbs, "X-Ray Resonance Exchange Scattering," *Phys. Rev. Lett.* **61**, 1245-1248 (1988).
- [11] D. Gibbs, J. P. Hill, and C. Vettier, "Recent Advances in X-Ray Magnetic Scattering," *Phys. Status Solidi B* **215**, 667-678 (1999).
- [12] G. Schütz, W. Wagner, W. Wilhelm, P. Kienle, R. Zeller, R. Frahm, and G. Materlik, "Absorption of circularly polarized x rays in iron," *Phys. Rev. Lett.* **58**, 737-740 (1987).
- [13] J. Stöhr, "Exploring the microscopic origin of magnetic anisotropies with X-ray magnetic circular dichroism (XMCD) spectroscopy," *J. Magn. Magn. Mater.* **200**, 470-497 (1999).
- [14] R. E. Camley and D. R. Tilley, "Phase transitions in magnetic superlattices," *Phys. Rev. B* **37**, 3413-3421 (1988).

- [15] J. G. LePage and R. E. Camley, "Surface phase transitions and spin-wave modes in semi-infinite magnetic superlattices with antiferromagnetic interfacial coupling," *Phys. Rev. Lett.* **65**, 1152-1155 (1990);
R. E. Camley, "Surface spin reorientation in thin Gd films on Fe in an applied magnetic field," *Phys. Rev. B* **35**, 3608-3611 (1987).
- [16] Y. Kamiguchi, Y. Hayakawa, and H. Fujimori, "Anomalous field dependence of magnetoresistance in Fe/Gd multilayered ferrimagnets," *Appl. Phys. Lett.* **55**, 1918-1919 (1989);
H. Fujimori, Y. Kamiguchi, and Y. Hayakawa, "New phenomena of magnetoresistance in ferrimagnetic Fe/Gd multilayers," *J. Appl. Phys.* **67**, 5716-5718 (1990);
José L. Prieto, "Transport properties of sharp antiferromagnetic boundaries in GdFe multilayers," Bas B. van Aken, Gavin Burnell, Chris Bell, Jan E. Evetts, Neil Mathur, and Mark G. Blamire, *Phys. Rev. B*, **69**, 054436 (2004).
- [17] M. Grimsditch, A. Hoffmann, P. Vavassori, Hongtao Shi, and D. Lederman, "Exchange-Induced Anisotropies at Ferromagnetic-Antiferromagnetic Interfaces above and below the Néel Temperature," *Phys. Rev. Lett.* **90**, 257201 (2003).
- [18] J. G. LePage and R. E. Camley, "Surface phase transitions and spin-wave modes in semi-infinite magnetic superlattices with antiferromagnetic interfacial coupling," *Phys. Rev. Lett.* **65**, 1152-1155 (1990).
- [19] D. Haskel, G. Srajer, Y. Choi, D. R. Lee, J. C. Lang, J. Meersschaut, J. S. Jiang, and S. D. Bader, "Nature of inhomogeneous magnetic state in artificial Fe/Gd ferrimagnetic multilayers," *Phys. Rev. B* **67**, 180406(R) (2003).
- [20] A. N. Bogdanov and U. K. Rößler, "Chiral Symmetry Breaking in Magnetic Thin Films and Multilayers," *Phys. Rev. Lett.* **87**, 037203 (2001).
- [21] C. Rau and S. Eichner, "Evidence for ferromagnetic order at gadolinium surfaces above the bulk Curie temperature," *Phys. Rev. B* **34**, 6347-6350 (1986).
- [22] D. Weller, S. F. Alvarado, W. Gudat, K. Schröder and M. Campagna, "Observation of Surface-Enhanced Magnetic Order and Magnetic Surface Reconstruction on Gd(0001)," *Phys. Rev. Lett.* **54**, 1555-1558 (1985).
- [23] H. Tang, D. Weller, T. G. Walker, J. C. Scott, C. Chappert, H. Hopster, A. W. Pang, D. S. Dossau, and D. P. Pappas, "Magnetic reconstruction of the Gd(0001) surface," *Phys. Rev. Lett.* **71**, 444-447 (1993).

- [24] C. Vettier, D. B. McWhan, E. M. Gyorgy, J. Kwo, B. M. Buntschuh, and B. W. Batterman, "Magnetic x-ray scattering study of interfacial magnetism in a Gd-Y superlattice," *Phys. Rev. Lett.* **56**, 757-760 (1986).
- [25] J. Kwo, E. M. Gyorgy, D. B. McWhan, M. Hong, F. J. DiSalvo, C. Vettier, and J. E. Bower, "Magnetic and Structural Properties of Single-Crystal Rare-Earth Gd-Y Superlattices," *Phys. Rev. Lett.* **55**, 1402-1405 (1985).
- [26] M. Taborelli, R. Allenspach, G. Boffa, and M. Landolt, "Magnetic coupling of surface adlayers: Gd on Fe(100)," *Phys. Rev. Lett.* **56**, 2869-2872 (1986).
- [27] N. Ishimatsu, H. Hashizume, S. Hamada, N. Hosoi, C. S. Nelson, C. T. Venkataraman, G. Srajer, and J. C. Lang, "Magnetic structure of Fe/Gd multilayers determined by resonant x-ray magnetic scattering," *Phys. Rev. B* **60**, 9596-9606 (1999).
- [28] D. Haskel, G. Srajer, J. C. Lang, J. Pollmann, C. S. Nelson, J. S. Jiang, and S. D. Bader, "Enhanced Interfacial Magnetic Coupling of Gd /Fe Multilayers," *Phys. Rev. Lett.* **87**, 207201 (2001).
- [29] J. C. Lang and G. Srajer, "Bragg transmission phase plates for the production of circularly polarized x rays," *Rev. Sci. Instrum.* **66**, 1540-1542 (1995).
- [30] R. M. Osgood III, S. K. Sinha, J. W. Freeland, Y. U. Idzerda, and S. D. Bader, "X-ray scattering from magnetic, rough surfaces," *J. Appl. Phys.* **85**, 4619-4621 (1999).
- [31] S. K. Sinha, E. B. Sirota, S. Garoff, and H. B. Stanley, "X-ray and neutron scattering from rough surfaces," *Phys. Rev. B* **38**, 2297-2311 (1988).
- [32] D. R. Lee, S. K. Sinha, D. Haskel, Y. Choi, J. C. Lang, S. A. Stepanov, and G. Srajer, "X-ray resonant magnetic scattering from structurally and magnetically rough interfaces in multilayered systems. I. Specular reflectivity," *Phys. Rev. B* **68**, 224409 (2003).
- [33] L. G. Parratt, "Surface Studies of Solids by Total Reflection of X-Rays," *Phys. Rev.* **95**, 359-369 (1954).
- [34] L. Nevot and P. Croce, "Caractérisation des surfaces par réflexion rasante de rayons X. Application à l'étude du polissage de quelques verres silicates" *Rev. Phys. Appl.* **15**, 761-779 (1980).

- [35] M. Blume and D. Gibbs, "Polarization dependence of magnetic x-ray scattering," *Phys. Rev. B* **37**, 1779-1789 (1988).
- [36] S. A. Stepanov and S. K. Sinha, "X-ray resonant reflection from magnetic multilayers: Recursion matrix algorithm," *Phys. Rev. B* **61**, 15302-15311 (2000).
- [37] D. K. G. de Boer, "Glancing-incidence x-ray fluorescence of layered materials," *Phys. Rev. B* **44**, 498-511 (1991).
- [38] M. Sajieddine, Ph. Bauer, K. Cherifi, C. Dufour, G. Marchal, and R. E. Camley, "Experimental and theoretical spin configurations in Fe/Gd multilayers," *Phys. Rev. B* **49**, 8815-8820 (1994).
- [39] J. C. Lang, Xindong Wang, V. P. Antropov, B. N. Harmon, A. I. Goldman, H. Wan, G. C. Hadjipanayis, and K. D. Finkelstein, "Circular magnetic x-ray dichroism in crystalline and amorphous GdFe₂" *Phys. Rev. B* **49**, 5993-5998 (1994).
- [40] J. P. Rueff, R. M. Galéra, S. Pizzini, A. Fontaine, L. M. Garcia, Ch. Giorgetti, E. Dartyge, and F. Baudelet, "X-ray magnetic circular dichroism at the Gd L edges in Gd-Ni-Co amorphous systems," *Phys. Rev. B* **55**, 3063-3070 (1997).
- [41] V. Holý and T. Baumbach, "Nonspecular x-ray reflection from rough multilayers," *Phys. Rev. B* **49**, 10668-10676 (1994).
- [42] A. Berger, G. Campillo, P. Vivas, J. E. Pearson, S. D. Bader, E. Baca, and P. Prieto, "Critical exponents of inhomogeneous ferromagnets," *J. Appl. Phys.* **91**, 8393-8995 (2002).
- [43] K. Binder and P. C. Hohenberg, "Surface effects on magnetic phase transitions," *Phys. Rev. B* **9**, 2194-2214 (1974).
- [44] O. F. K. McGrath, N. Ryzhanova, C. Lacroix, D. Givord, C. Fermon, C. Miramond, G. Saux, S. Young, and A. Vedyayev, "Observation and interpretation of a partial Gd twisted spin state in an epitaxial Gd/Fe bilayer," *Phys. Rev. B* **54**, 6088-6091 (1996).
- [45] W. Hahn, M. Loewenhaupt, Y. Y. Huang, G. P. Felcher, and S. S. P. Parkin, "Experimental determination of the magnetic phase diagram of Gd/Fe multilayers," *Phys. Rev. B* **52**, 16041-16048 (1995).

- [46] K. Cherifi, C. Dufour, Ph. Bauer, G. Marchal, and Ph. Mangin, "Experimental magnetic phase diagram of a Gd/Fe multilayered ferrimagnet," K. Cherifi, C. Dufour, Ph. Bauer, G. Marchal, and Ph. Mangin, *Phys. Rev. B* **44**, 7733-7736 (1991).
- [47] D. T. Cromer and D. Liberman, "Relativistic Calculation of Anomalous Scattering Factors for X Rays," *J. Chem. Phys.* **53**, 1891-1898 (1970).
- [48] http://www.cxro.lbl.gov/optical_constants/;
B. L. Henke, E. M. Gullikson, and J. C. Davis. *X-ray interactions: photoabsorption, scattering, transmission, and reflection at E=50-30000 eV, Z=1-92*, Atomic Data and Nuclear Data Tables Vol. **54** (no.2), 181-342 (July 1993).
- [49] Zhong Zhong, Dean Chapman, Bruce Bunker, Grant Bunker, Robert Fischetti, and Carlo Segre, "A bent Laue analyzer for fluorescence EXAFS detection," *J. Synchrotron Rad.* **6**, 212-214 (1999).
- [50] LLG Micromagnetics Simulator, <http://llgmicro.home.mindspring.com>
- [51] L. Landau and E. Lifshitz, "On the theory of the dispersion of magnetic permeability in ferromagnetic bodies," *Phys. Z. Sowjet* **8**, 153-169 (1935).
- [52] C. C. Shir, "Computations of the micromagnetic dynamics in domain walls," *J. Appl. Phys.* **49**, 3413-3421 (1978);
R. Victora, "Quantitative theory for hysteretic phenomena in CoNi magnetic thin films," *Phys. Rev. Lett.* **58**, 1788-1791 (1987).
- [53] Michael R. Scheinfein and Elizabeth A Price *LLG User Manual v2.36*.
- [54] Y. Choi, D. Haskel, R. Camley, D. R. Lee, J. C. Lang, G. Srajer, J. S. Jiang, and S. D. Bader, "Temperature evolution of the Gd magnetization profile in strongly coupled Gd/Fe multilayers," *Phys. Rev. B* **70**, 134420 (2004).
- [55] *Frontiers in Magnetism of Reduced Dimension Systems*, edited by Vitor G. Bar'yakhtar, Phillip E. Wigen, and Natalia A. Lesnik (Kluwer Academic Publishers, Boston, 1998).

- [56] R. P. Cowburn, A. O. Adeyeye, and J. A. C. Bland, "Magnetic domain formation in lithographically defined antidot Permalloy arrays," *Appl. Phys. Lett.* **70**, 2309-2311 (1997);
 L. Torres, L. Lopez-Diaz, and J. Iñiguez, "Micromagnetic tailoring of periodic antidot permalloy arrays for high density storage," *Appl. Phys. Lett.* **73**, 3766-3768 (1998);
 A. Y. Toporov, R. M. Langford, and A. K. Petford-Long, "Lorentz transmission electron microscopy of focused ion beam patterned magnetic antidot arrays," *Appl. Phys. Lett.* **77**, 3063-3065 (2000);
 C. T. Yu, J. Jiang, L. Shen, P. J. Flanders, and G. J. Mankey, "The magnetic anisotropy and domain structure of permalloy antidot arrays," *J. Appl. Phys.* **87**, 6322-6324 (2000);
 U. Welp, V. K. Vlasko-Vlasov, G. W. Crabtree, C. Thompson, V. Metlushko, and B. Ilic, "Magnetic domain formation in perforated permalloy films," *Appl. Phys. Lett.* **79**, 1315-1317 (2001);
 I. Guedes, N. J. Zaluzec, M. Grimsditch, V. Metlushko, P. Vavassori, B. Ilic, P. Neuzil, and R. Kumar, "Magnetization of negative magnetic arrays: Elliptical holes on a square lattice," *Phys. Rev. B* **62**, 11719-11724 (2000).
- [57] M. J. Freiser, "A survey of magnetoopic effects," *IEEE Trans. Magn.* **MAG-4**, 152-161 (1968).
- [58] P. Vavassori, V. Metlushko, R. M. Osgood III, M. Grimsditch, U. Welp, G. Crabtree, Wenjun Fan, S. R. J. Brueck, B. Ilic, and P. J. Hesketh, "Magnetic information in the light diffracted by a negative dot array of Fe," *Phys. Rev. B* **59**, 6337-6343 (1999);
 P. Vavassori, N. Zaluzec, V. Metlushko, V. Novosad, B. Ilic, and M. Grimsditch, "Magnetization reversal via single and double vortex states in submicron Permalloy ellipses," *Phys. Rev. B* **69**, 214404 (2004).
- [59] V. Chakarian, Y. U. Izderda, G. Meigs, E. E. Chaban, J.-H. Park, and C. T. Chen, "Element-specific vector magnetometry with magnetic circular dichroism," *Appl. Phys. Lett.* **66** 3368-3370 (1995).
- [60] M. Tolan, W. Press, F. Brinkop, and J. P. Kotthaus, "X-ray diffraction from laterally structured surfaces: Crystal truncation rods," *J. Appl. Phys.* **75** 7761-7769 (1994).
- [61] <http://math.nist.gov/oommf>

- [62] E. C. Stoner and E. P. Wohlfarth, "A mechanism of magnetic hysteresis in heterogeneous alloys," *Philos. Trans. R. Soc. London, Ser. A* **240**, 599-644 (1948).
- [63] D. R. Lee, Y. Choi, C.-Y. You, J. C. Lang, D. Haskel, G. Srajer, V. Metlushko, B. Illic, and S. D. Bader, "Magnetization reversal measurements in Gd/Fe multilayer antidot arrays by vector magnetometry using x-ray magnetic circular dichroism," *Appl. Phys. Lett.* **81** 4997-4999 (2002).
- [64] B. A. Evertitt and A. V. Pohm, "Pseudo spin valve magnetoresistive random access memory," *J. Vac. Sci. Technol. A* **16**, 1794-1800 (1998);
S. Tehrani, E. Chen, M. Durlam, M. DeHerrera, J. M. Slaughter, J. Shi, and G. Kerszykowsky, "High density submicron magnetoresistive random access memory," *J. Appl. Phys.* **85**, 5822-5827 (1999);
J. M. Daughton, A. V. Pohm, R. T. Fayfield, and C. H. Smith, "Applications of spin dependent transport materials," *J. Phys. D* **32**, R169-177 (1999).
- [65] R. D. McMichael, J. Eicke, M. J. Donahue, and D. G. Porter, "Domain wall traps for low-field switching of submicron elements," *J. Appl. Phys.* **87**, 7058-7060 (2000).
- [66] P. J. Eng, M. L. Rivers, B. X. Yang, and W. Schildkamp, "Micro-focusing 4 KeV to 64 KeV X-Rays with bent Kirkpatrick-Baez mirrors," *Proc. SPIE* **2516**, 41-51 (1995);
J. C. Lang, J. Pollmann, D. Haskel, G. Srajer, J. Maser, J. S. Jiang, and S. D. Bader, "Imaging buried magnetic domains using hard x-rays," *Proc. SPIE* **4499**, 1 (2001).
- [67] H. Sakurai, F. Ito, H. Maruyama, A. Koizumi, K. Kobayashi, H. Yamazaki, Y. Tanji, and H. Kawata, "Circular Magnetic X-Ray Dichroism at the K-Absorption Edge in Fe-Ni Alloys," *J. Phys. Soc. Jpn.* **62**, 459-463 (1993).
- [68] F. J. Castaño, Y. Hao, S. Haratani, C. A. Ross, B. Vögeli, Henry I. Smith, C. Sánchez-Hanke, C.-C. Kao, X. Zhu, P. Grütter, "Magnetic force microscopy and x-ray scattering study of $70 \times 550 \text{ nm}^2$ pseudo-spin-valve nanomagnets," *J. Appl. Phys.* **93**, 7927-7929 (2003).

- [69] M. A. Ruderman and C. Kittel, "Indirect Exchange Coupling of Nuclear Magnetic Moments by Conduction Electrons," *Phys. Rev.* **96**, 99-102 (1954);
T. Kasuya, "A theory of metallic ferromagnetism and antiferromagnetism on Zeners model," *Prog. Theor. Phys.* **16**, 45-57 (1956);
K. Yosida, "Magnetic Properties of Cu-Mn Alloys," *Phys. Rev.* **106**, 893-898 (1957).
- [70] L. Neel, *C.R. Acad. Sci.* "On a new coupling mode between the magnetization of two ferromagnetic thin films," **255**, 1676 (1962).
- [71] R. P. Cowburn, D. K. Koltsov, A. O. Adeyeye, M. E. Welland, and D. M. Tricker, "Single-Domain Circular Nanomagnets," *Phys. Rev. Lett.* **83**, 1042-1042 (1999);
J. A. Johnson, M. Grimsditch, V. Metlushko, P. Vavassori, B. Ilic, P. Neuzil, and R. Kumar, "Magneto-optic Kerr effect investigation of cobalt and permalloy nanoscale dot arrays: Shape effects on magnetization reversal," *Appl. Phys. Lett.* **77**, 4410-4412 (2000);
J. Rothman, M. Kläui, L. Lopez-Diaz, C. A. F. Vaz, A. Bleloch, J. A. C. Bland, Z. Cui, and R. Speaks, "Observation of a Bi-Domain State and Nucleation Free Switching in Mesoscopic Ring Magnets," *Phys. Rev. Lett.* **86**, 1098-1101 (2001).
- [72] C. Kao, J. B. Hastings, E. D. Johnson, D. P. Siddons, G. C. Smith, and G. A. Prinz, "Magnetic-resonance exchange scattering at the iron L_{II} and L_{III} edges," *Phys. Rev. Lett.* **65**, 373-373 (1990).
- [73] J. W. Freeland, J. C. Lang, G. Srajer, R. Winarski, D. Shu, and D. M. Mills, "A unique polarized x-ray facility at the Advanced Photon Source," *Rev. Sci. Instrum.* **73**, 1408-1410 (2001).
- [74] M. Tolan, W. Press, F. Brinkop, and J. P. Kotthaus, "X-ray diffraction from laterally structured surfaces: Total external reflection," *Phys. Rev. B* **51**, 2239-2251 (1995).
- [75] A. Ney, P. Pouloupoulos, and K. Baberschke, "Surface and interface magnetic moments of Co/Cu(001)," *Europhys. Lett.* **54**, 820-825 (2001).
- [76] A. Gibaud, G. Vignaud, and S. K. Sinha, "The Correction of Geometrical Factors in the Analysis of X-ray Reflectivity," *Act Cryst. A* **49**, 642-648 (1993).
- [77] www.aps.anl.gov/About/APS_Tour.

- [78] K. Hirano, T. Ishikawa and S. Kikuta, "Perfect crystal X-ray phase retarders," Nucl. Instrum. & Methods Phys. Res. A **336**, 343-353 (1993).
- [79] B. W. Batterman and H. Cole, "Dynamical Diffraction of X Rays by Perfect Crystals," Rev. Mod. Phys. **36**, 681-717 (1964).
- [80] K. Hirano, K. Izumi, T. Ishikawa, S. Annaka, and S. Kikuta, "An X-Ray Phase Plate Using Bragg-Case Diffraction," Jpn. J. Appl. Phys. **30**, L407-410 (1991); K. Hirano, "Polarization-Tunable X-Ray Optics for Synchrotron Radiation," Jpn. J. Appl. Phys. **36**, L637-638 (1997).
- [81] *Resonant Anomalous X-ray Scattering: Theory and Applications*, edited by G. Materlik, C. J. Sparks, and K. Fischer (North-Holland, Amsterdam, 1994).
- [82] L. G. Parratt and C. F. Hempstead, "Anomalous Dispersion and Scattering of X-Rays," Phys. Rev. **94**, 1593 (1954).
- [83] J. O. Cross, M. Newville, J. J. Rehr, L. B. Sorensen, C. E. Bouldin, G. Watson, T. Gouder, G. H. Lander, and M. I. Bell, "Inclusion of local structure effects in theoretical x-ray resonant scattering amplitudes using ab initio x-ray-absorption spectra calculations," Phys. Rev. B **58**, 11215-11225 (1998).
- [84] J. D. Jackson, *Classical Electrodynamics*, (John Wiley & Sons, New York, 1975).
- [85] A. Hubert, R. Schäfer, *Magnetic domains*, Springer (1998).
- [86] J. Slonczewski, "Overview of interlayer exchange theory," J. Mag. Magn. Mater. **150**, 13-24 (1995).

APPENDIX A

Specular X-ray Reflectivity

A.1. Parratt's recursive relation with Nevot-Croce roughness

X-ray reflectivity has been a widely used technique to study electron density profile in the direction normal to the surface of a flat film. Since the phase information is lost in x-ray reflectivity measurements, the measured reflectivity cannot be directly inverted directly to get the depth profile. Therefore the measured reflectivity is compared or fitted with the calculated reflectivity that is based on a model structure.

X-ray specular reflectivity of a multilayer without roughness can be exactly calculated using the Parratt's recursive relation with boundary conditions at each interface. For the tangential components of the electric and magnetic fields, the ratio between the amplitudes of reflected and transmitted fields at the bottom of the j th layer (as shown in Fig. A.1) can be written as [33],

$$\begin{aligned}
 R_j &= \frac{E_j^R}{E_j^T} = \frac{r_{j,j+1} + R_{j+1}e^{2ik_{z,j+1}d_{j+1}}}{1 + r_{j,j+1}R_{j+1}e^{2ik_{z,j+1}d_{j+1}}} \\
 r_{j,j+1} &= \frac{k_{z,j} - k_{z,j+1}}{k_{z,j} + k_{z,j+1}} \\
 k_{z,j} &= k_0 \sqrt{(n_j^2 - \cos^2 \theta_0)} \\
 k_0 &= \frac{2\pi}{\lambda}
 \end{aligned}
 \tag{A.1}$$

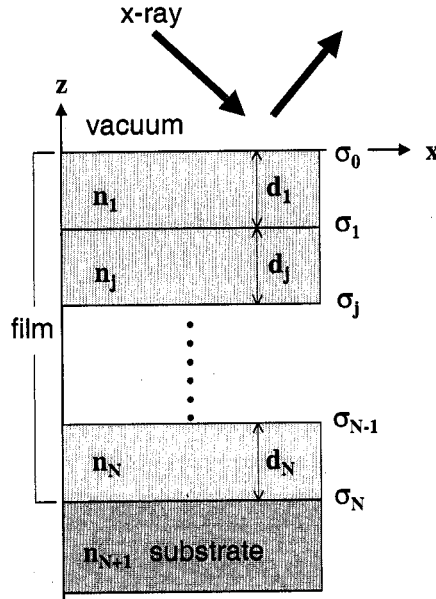


Figure A.1. Multilayer structure with N layers on a substrate. The z axis is perpendicular to the film surface. n_j is the refractive index of the j th layer with a thickness of d_j .

where d_j is the thickness of j th layer and $r_{j,j+1}$ is the Fresnel reflectivity coefficient of a single interface. The z component of the wavevector in the j th layer is $k_{z,j}$ as obtained from Snell's law. k_0 is the wavevector in vacuum and λ is the wavelength of incident x-ray. n_j is the refractive index of the j th layer, and the θ_0 is the incident angle. For a semi-infinite substrate ($d_{\text{substrate}} \gg d_{\text{film}}$), assuming $R_{\text{sub}} = 0$, the overall reflected intensity normalized to the incident intensity can be obtained by $\text{Refl.} = |R_0|^2$ using the equation Eq. A.1.

Roughness effects can be introduced to Eq. A.1 by multiplying a static Debye-Waller-like factor to the Fresnel reflectivity coefficient of an ideal interface. For a rough interface with a Gaussian height distribution, the reflectivity coefficient can be

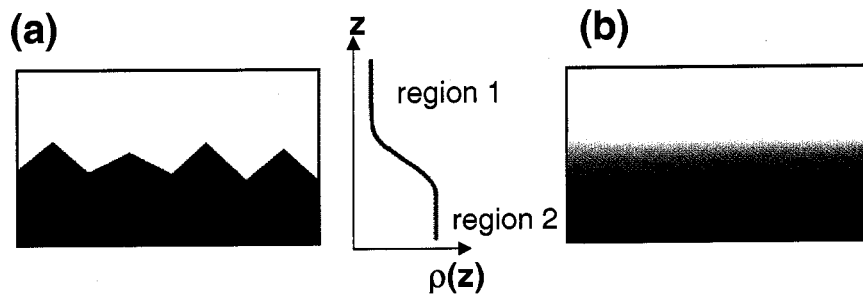


Figure A.2. (a) An ideal interface with roughness and (b) an ideal interface with intermixing. Since specular reflectivity measured laterally averaged density profiles, the two interfaces can have an identical density profile as shown in the middle.

expressed following the method by Nevot and Croce as [34]:

$$(A.2) \quad r_{j,j+1}^{rough} = r_{j,j+1}^{ideal} e^{-2\sigma_j^2 k_{z,j} k_{z,j+1}},$$

where σ_j is the rms roughness of the j th interface. The roughness included here is *effective* roughness. In a real sample, an interface can have roughness, interdiffusion (intermixing, alloying), or both. Specular reflectivity measures a density profile along the interface normal direction and the density is averaged over lateral area probed. Because of this lateral averaging, an interface with roughness and an interface with intermixing can have identical density profiles as illustrated in Fig. A.2. Thus, from specular reflectivity, the above two cases cannot be distinguished, but instead, the interface effects observed in the specular reflectivity is due to *effective* roughness that includes both of the two effects. In order to distinguish the two interface effects, diffuse scattering measurements are necessary since a purely intermixed interface does not give rise to diffuse scattering while a rough interface does.

A.2. Geometrical correction and resolution function

At very low incident angles ($\approx 0^\circ$) in reflectivity measurements, the finite x-ray beam and sample size effects [76] have to be included in reflectivity analysis (Fig. A.3). At $\theta=0$, the sample does not reflect any intensity but the half of the beam intensity falls into the detector [Fig. A.3(a)]. As the incident angle is increased, the detector at 2θ position sees the sum of the decreasing intensity coming from the direct beam and the increasing intensity reflected from the sample [Fig. A.3(b)]. This situation is continued until the incident angle θ is θ_b where the intensity measured is coming only from the intensity reflected from the sample [Fig. A.3(c)]. If the beam is uniform and described by a step function of full-width-half-maximum (FWHM) equal to w , then the corrected reflectivity intensity is expressed as:

$$(A.3) \quad I_c(2\theta) = \begin{cases} I(2\theta) \cdot (\sin \theta)L/w = I(2\theta) \cdot \sin \theta / \sin \theta_b & \text{for } \theta \leq \theta_b \\ I(2\theta) \cdot 1 & \text{for } \theta > \theta_b. \end{cases}$$

For x-ray specular reflectivity fitting procedure, the geometrical correction factor can be included in the fitting program. The θ_b angle can be obtained by measuring a footprint scan as shown in Fig. A.4. An alternative method is using the fit of the footprint scan. Once the analytical expression is obtained from the fitting of the footprint scan, this expression can be included as a geometrical correction in the reflectivity calculation.

Specular reflectivity is sensitive to structural variations of a film in direction perpendicular to the film plane. The momentum transfer perpendicular to the surface

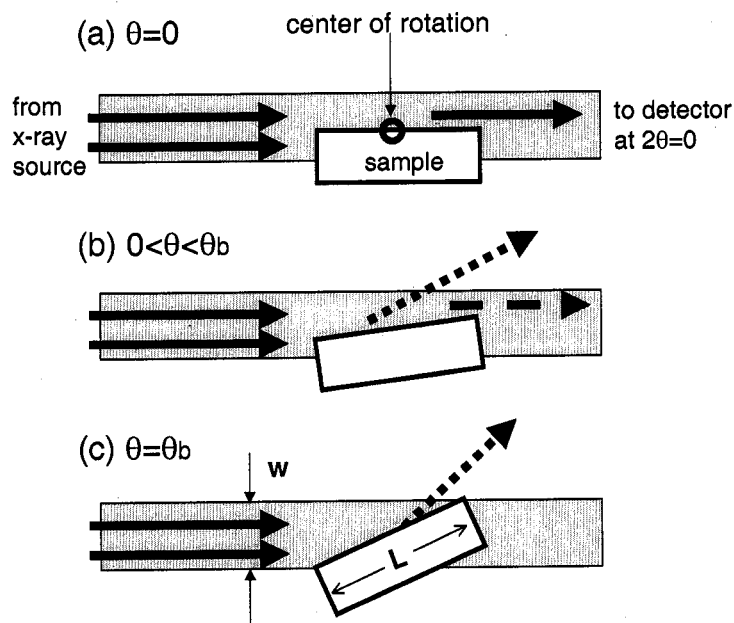


Figure A.3. Geometrical factor correction at grazing incident angles. w , L , and, θ are the beam width, the length of the sample, and the incident x-ray angle, respectively.

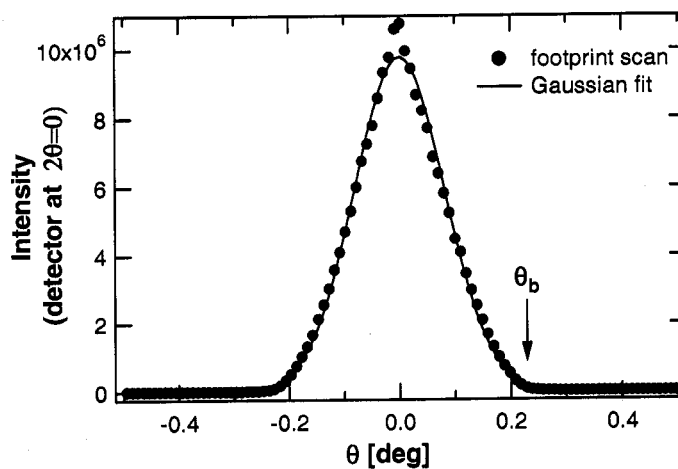


Figure A.4. A footprint scan for the geometrical factor correction at grazing incident angles. The detector was fixed at $2\theta=0^\circ$, the sample was rotated around $\theta=0^\circ$. The symbols represent measured intensity, and the line is a Gaussian peak fit to it.

plane is expressed by:

$$(A.4) \quad q_z = k_0(\sin \alpha + \sin \beta) = 2k_0 \sin(2\theta/2) \cos(\omega),$$

where α and β are the incident and exit angles, respectively. k_0 is $2\pi/\lambda$. ω is the offset angle $\omega = \alpha - 2\theta/2$ where 2θ is the detector angle.

The finite resolution in the momentum transfer q_z can be obtained from the differential of Eq. A.5 with respect to α and β :

$$(A.5) \quad \delta q_z = k_0(\delta \alpha \cos \alpha + \delta \beta \cos \beta).$$

If $\delta \alpha$ and $\delta \beta$ are assumed to be statistically independent variables with Gaussian distribution of rms values of $\Delta \alpha$ and $\Delta \beta$, the uncertainty in q_z is given by:

$$(A.6) \quad \Delta q_z = k_0 \sqrt{\Delta \alpha^2 \cos^2 \alpha + \Delta \beta^2 \cos^2 \beta} \approx k_0 \sqrt{\Delta \alpha^2 + \Delta \beta^2}.$$

For specular reflectivity, the angles are very small so that Δq_z is almost constant over the scan range. Therefore the resolution function of Δq_z can often be neglected.

APPENDIX B

Experimental Setup for Magnetism studies using polarized synchrotron radiations

B.1. Beamline Optics: phase retarder, monochromator, microfocusing

Magnetic characterizations with polarized x rays were conducted at the beamline 4ID-D [73] of the Advanced Photon Source at Argonne National Laboratory. First, generation of synchrotron radiation will be briefly described [77]. Electron-positron pairs are produced by an electron linear accelerator, and the electrons go through another accelerator and an accumulator where they are compressed into a bunch. After the accumulator, the electron bunches are injected into a booster where they are accelerated to 7 GeV, and the booster injects the electron bunches into a bucket in the storage ring. The storage ring is 1104 meters in circumference, consisting of 40 sectors and a radiofrequency system. As the electrons orbit the storage ring, the beam of electrons is steered and focused by electromagnets. While orbiting the storage ring, the electron beam decelerates as it emits synchrotron radiation. The lost energy due to the emission is replenished by the radiofrequency system. The storage ring is made of straight sections where linear arrays of permanent magnets with alternating polarity are inserted. These arrays of magnets are called insertion devices. As the orbiting electrons are accelerated and their trajectory is altered by

the insertion devices, the synchrotron radiation is emitted in a direction tangential to the arc of the electron beam.

X-ray optics setup leading to the 4ID-D beamline is shown in Fig. B.1. The undulator, as an insertion device, is used to produce a high brilliance beam of synchrotron radiation. Once the synchrotron radiation (white beam radiation) comes out of the undulator, and it goes through a set of Si (111) liquid nitrogen cooled high heat load monochromator optics. The monochromator diffracts only a narrow range of wavelength satisfying Bragg's law, and the double-crystal configuration keeps x-ray beams at the same height. By changing the angle of the monochromator optics, the energy of incident x-ray can be selected. Typically, the monochromator is calibrated before experiments by performing transmission measurements of a known standard metal film across an absorption edge.

After going through the monochromator, a diamond (111) Bragg transmission phase retarder (Fig. B.2) is used to provide circularly polarized x rays [29] that are essential for magnetic characterizations. Circularly polarized x rays have an angular momentum so that they couple with angular momenta in magnetic materials [78]. Before the phase retarder, the x-ray beam is linearly polarized (σ polarized), and the phase retarder transforms linear polarization into circular polarization by inducing $\pi/2$ phase shift between equal amounts of σ and π polarized radiation. X-ray phase retarder is based on dynamic diffraction, using the fact that inside a crystal the wave vectors for σ - and π -polarization states are slightly different from each other due to the dispersion relation. By taking advantage of this difference, a phase retardation between the two polarization components can be induced. Based on the dynamical

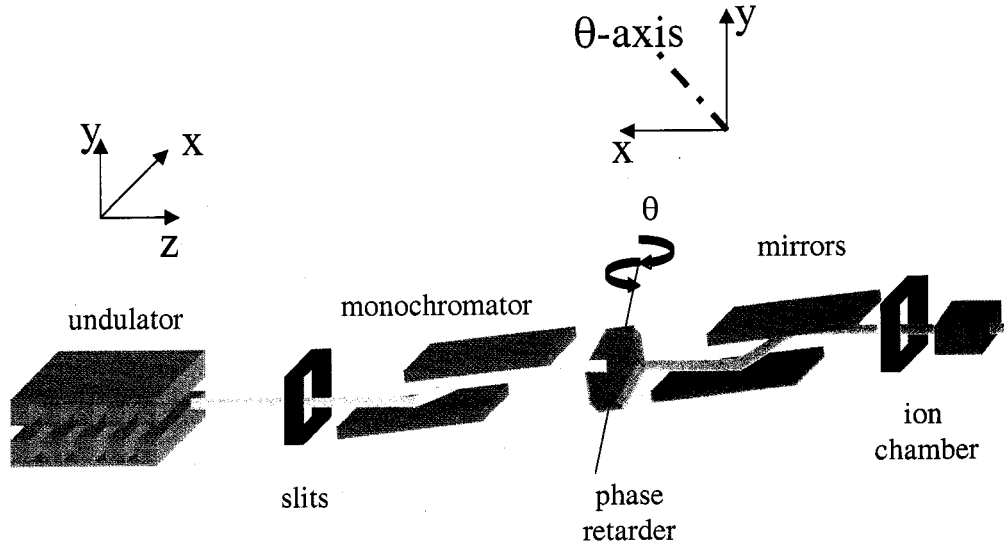


Figure B.1. The beamline optics at 4ID-A/B, APS, ANL. All shown beams lie in the vertical plane y - z . The rotation axis of the diamond (111) phase retarder is in the x - y plane, with 45° offset from the y -axis as shown on top.

theory of x-ray diffraction [79], a wave field for transmitted beam can be expressed as a linear combination of two plane waves with two wave vectors \mathbf{K}_σ and \mathbf{K}_π . Due to the slight difference between \mathbf{K}_σ and \mathbf{K}_π , the phase relation between the two waves changes while propagating through the crystal. At the back surface of the crystal, the two plane waves are recombined into one plane outside the crystal. Once outside the crystal the polarization state depends on the accumulated phase difference δ between σ - and π -components, and this phase difference can be expressed as [80]:

$$(B.1) \quad \delta = 2\pi\varepsilon |\mathbf{K}_\sigma - \mathbf{K}_\pi|t$$

Here, t is the thickness of crystal. For $|\mathbf{K}_\sigma| > |\mathbf{K}_\pi|$, $\varepsilon=1$ and for $|\mathbf{K}_\sigma| < |\mathbf{K}_\pi|$, $\varepsilon=-1$.

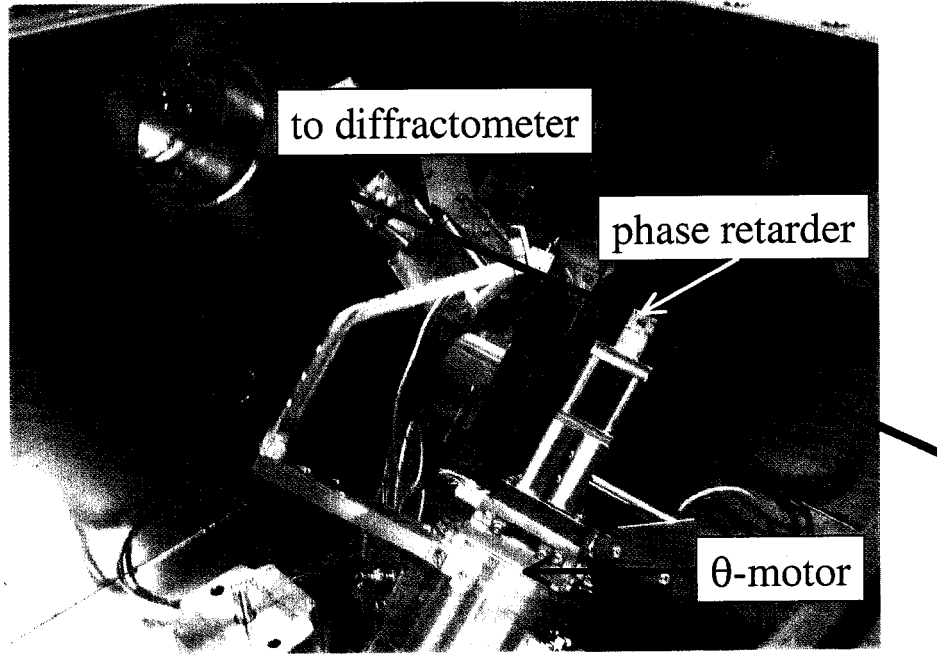


Figure B.2. Diamond phase retarder for circularly polarized x rays. The x rays from the monochromator optics are linearly polarized (blue arrow), and after going through the phase retarder, x rays are circularly polarized (red arrow).

The degree of this birefringence is a function of the offset of the incoming beam from the Bragg angle. The phase shift δ between the two polarization components for Bragg diffraction can be also expressed as [29],

$$(B.2) \quad \delta = \frac{\pi}{2} \left(\frac{r_e \lambda^2}{\pi V} \right)^2 \frac{t \sin 2\theta_B}{\lambda \Delta\theta \sin \theta_B} \text{Re}(F_H F_H^*),$$

where r_e is the classical electron radius, λ is wavelength, V is the volume of unit cell, t is the phase retarder thickness, and F_H is the structure factor.

For fixed t and λ values, shifting the offset angle $\pm\Delta\theta$ results in reversing the phase shift $\pm\delta$. Thus, by moving to opposite sides of the rocking curve, the helicity of the circularly polarized beam can be reversed. For the current experimental setup

as shown in Fig. B.2, the diamond phase retarder is attached on a lever arm with piezoelectric PZT (Lead Zirconate Titanate) so that the helicity of the x-ray can be rapidly reversed. After going through the phase plate, the x-ray beam is circularly polarized with a degree of polarization, $P_c \approx 0.95$. The thickness of the diamond phase plate is about $400 \mu\text{m}$, and x-ray intensity is typically attenuated by less than one order of magnitude by the phase retarder.

In Fig. B.3 an absorption measurement is shown as a function of the diamond phase retarder angle. For a fixed incoming x-ray energy, the phase retarder is rotated around to find the 111 Bragg peak by searching for an angle where the maximum absorption is measured. After the θ_{Bragg} is found, the optimum offset for circular polarization can be calculated using *PhaRet* program (Fig. B.4). The program is made using MS-Visual C++, and its calculation algorithm is based on Dr. Daniel Haskell's Fortran code. In Fig. B.5, the degree of circular polarization is plotted as a function of an offset angle from θ_{111} for a $400 \mu\text{m}$ thick diamond at $E=7.2 \text{ keV}$.

After the phase retarder, x rays go through focusing optics that are coated with Pd to reject higher harmonics that satisfy Bragg condition for Si(111) monochromators. For example, while the first harmonic (with an energy E_1) diffracts from Si-111 planes, a third harmonic (with an energy $3 \times E_1$) also diffracts from Si-333 planes. Calculated x-ray reflectivity from Pd mirror is plotted in Fig. B.6. As the mirror is slightly detuned purposely, the reflectivity for the third harmonics is reduced by 3 orders of magnitude while the first harmonics is reduced by less than 1 order of magnitude.

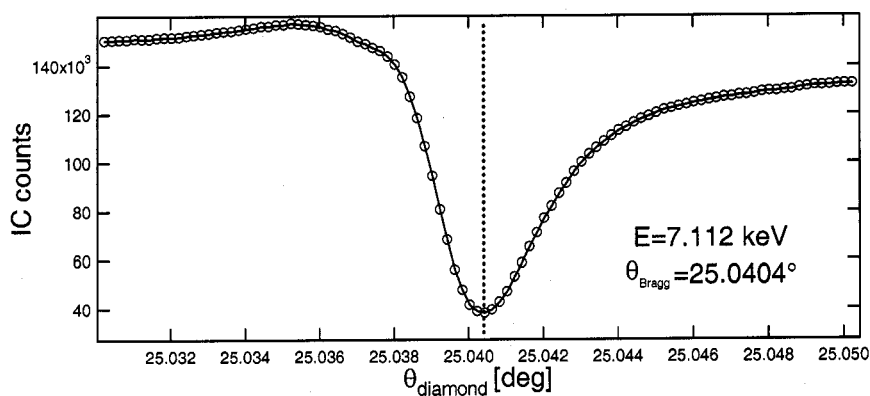


Figure B.3. The Diamond(111) phase retarder scan. An ion chamber (IC) is placed after the diamond, and absorption is measured as the diamond angle is changed around the Bragg angle. The incoming photon energy is 7.112 keV near the Fe K-edge.

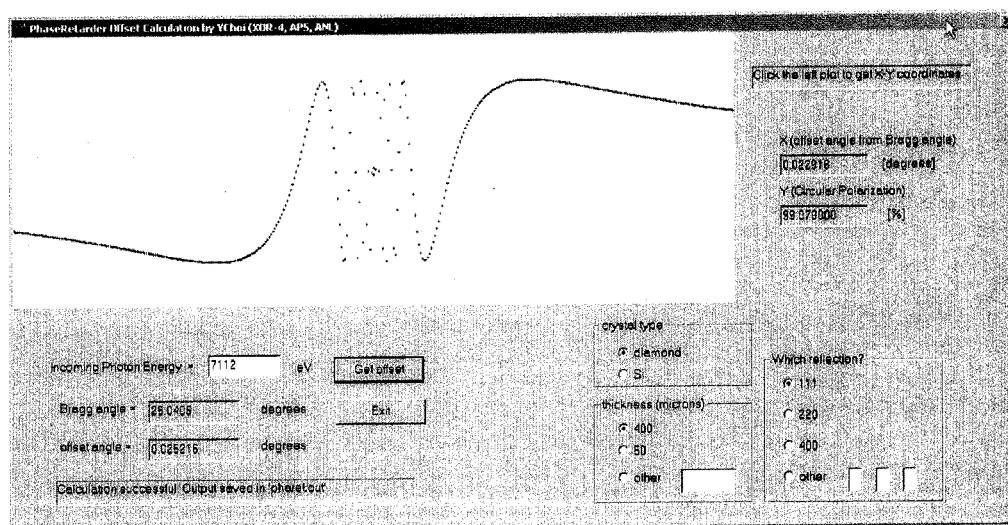


Figure B.4. *Pharet* program for calculation of the phase retarder offset angle.

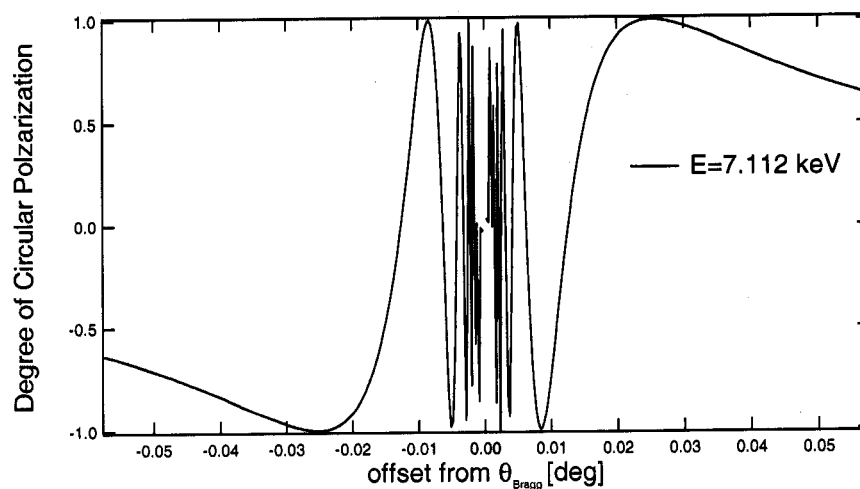


Figure B.5. The degree of circular polarization as a function of the phase retarder offset angle calculated by *Pharet* program at $E=7.112$ keV.

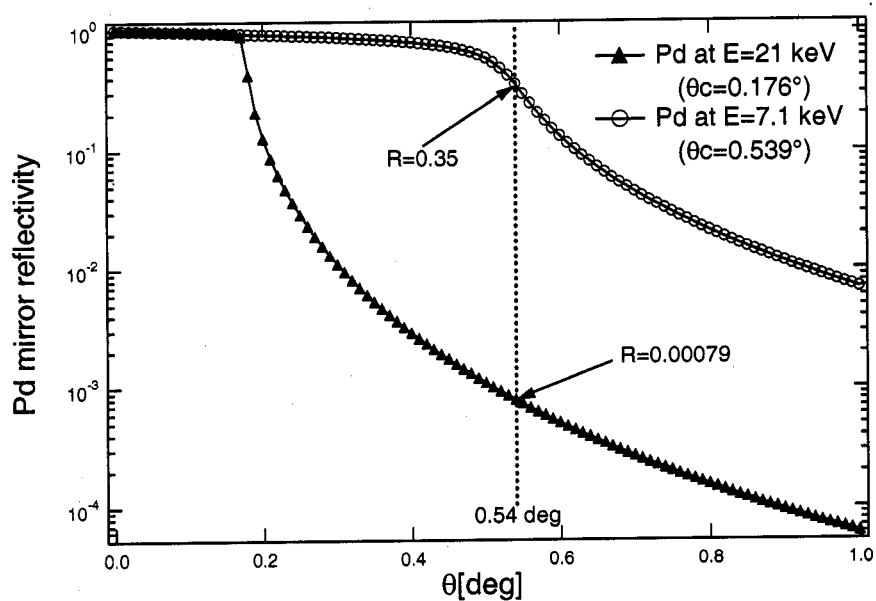


Figure B.6. Calculated x-ray reflectivity from Pd mirror at $E=7.1$ keV and $E=21$ keV (third harmonics).

B.2. Beamline Setup for Experiments

After going through the beamline optics as described in the previous section, x-ray beam now enters the experimental hutch 4ID-D where a diffractometer or a micro-imaging stage is placed (Figs. B.7-B.8). Ion chambers are used to measure x-ray intensity without reducing the beam intensity appreciably. In an ion chamber, an inert gas flows through two metal plate held at a potential difference, and as x rays pass through, the inert gas is ionized and an output current is produced proportional to the x-ray beam intensity. For absorption and diffraction measurements, these ion chambers are used as a monitor to correct any drift in the incoming beam intensity. In addition to the ion chambers, solid state and scintillation detectors are used. For absorption measurements, energy dispersive Ge solid-state detectors are used to discriminate fluorescence from the sample with an energy resolution of a few hundreds eV near 8 keV. For scattering experiments, NaI scintillation detectors are used.

In order to apply magnetic fields to the samples, a NdFeB permanent magnet or a two-pole electromagnet is used. These magnets are designed so that they apply an in-plane magnetic field without blocking either the incident or scattered beam. For temperature dependent scattering/absorption measurements, the sample is placed inside a Be-dome that is a part of a closed-cycle He refrigerator mounted on the diffractometer as shown in Fig. B.7.

For local magnetization measurements, a focusing optics setup is used to reduce the incident x-ray beam size without losing the x-ray intensity appreciably. The x-ray

beam is focused down to a few microns using a set of focusing mirrors in Kirkpatrick-Baez (KB) geometry [66] as shown in Fig. B.8. The first KB mirror focuses the incoming x-ray vertically and the second focuses horizontally. The mirrors are in a trapezoid shape and made of single-crystal Si coated with Cr(5 nm)/Rh(40 nm). Each mirror is bent slightly by two piezoelectric motors for focusing. The mirrors are 100 mm long, and typically they are bent with a central radius of curvature $R_o \approx 38$ m. The incident angle of x rays on the focusing mirrors is less than 8 mrad, and at this low incident angle, the change in the degree circular polarization of the incoming beam is negligible.

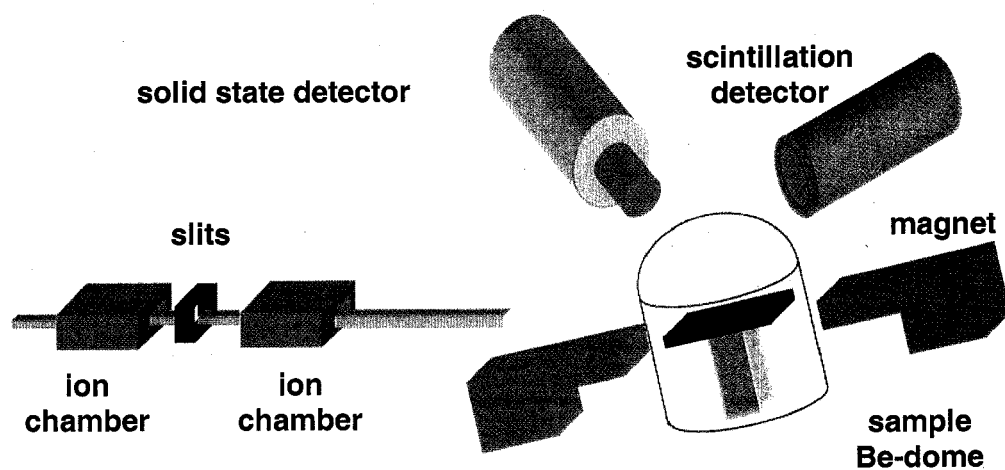


Figure B.7. The beamline optics at 4ID-D, APS, ANL.

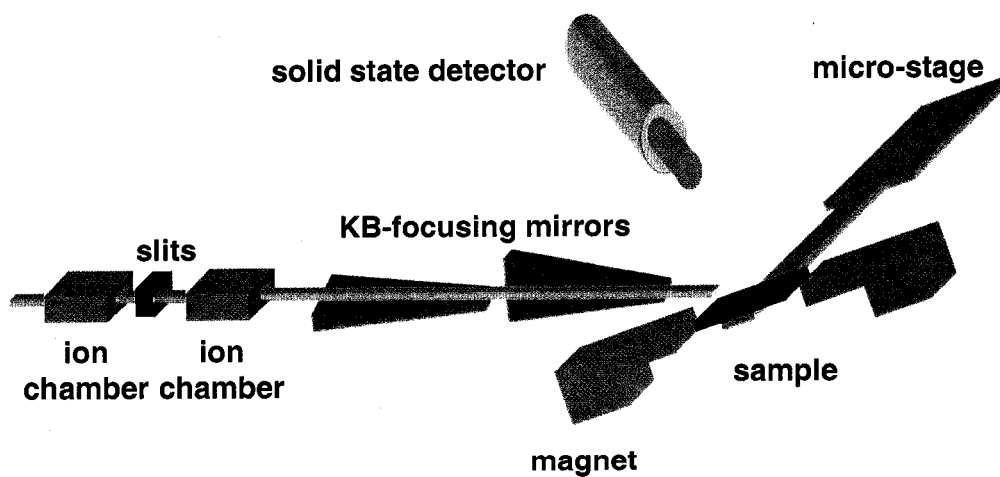


Figure B.8. KB focusing mirror setup for experiments with micro x-ray beam at 4ID-D, APS, ANL.

APPENDIX C

Atomic scattering factors for x-ray resonant scattering

C.1. Atomic scattering factors near resonant energies

The x-ray scattering amplitude can be expressed as $f = f_o + \Delta f$ where f_o is a photon energy independent term and Δf is the energy and polarization dependent resonant term. This resonant term has real and imaginary parts, $\Delta f = f' + if''$. The resonant term is normally small since x rays interact weakly with matter. However, when x-ray energy is near absorption edges of atoms, changing energy can cause significant changes in f' and f'' and in scattered intensities and absorption. Near an absorption edge, the resonantly excited electron probes the local geometry and the electron states in and around the absorbing atom and thus provide site specific information on charge distribution, magnetic moments, and density of unoccupied states [81].

For accurate analysis on resonant x-ray scattering data, it is important to obtain accurate resonant scattering amplitudes, $\Delta f = f' + if''$. Calculations of Δf assuming isolated atom models [47, 82] are accurate away from resonant energies, and typically these tabulated values are used for the analysis of x-ray scattering data when x-ray energy is away from resonant energies. However, near resonant energies, the tabulated values from the isolated atom models may not be accurate [83]. Since these values are based on the calculations that do not include the effects of the

local environment around the resonant atoms, some of important spectral features (for example, whitelines at certain absorption edges) can not be reproduced. The absorption cross section near a core electron resonance reflects the density of the final states available to the outgoing photoelectron, and the density of the states depend on the local environment around the resonant atom.

During the XRMS measurements on the Fe/Gd multilayer for structural and magnetic characterization, resonant scattering amplitude of the Gd atoms in the multilayer were obtained from x-ray absorption measurements through the L_2 absorption edge (Fig. C.1). In Fig. C.1(b), the tabulated values and the experimentally derived values are compared. Near the absorption edge, the discrepancy between the tabulated and experimental values becomes large. Absorption measurements are done in fluorescence geometry since the fluorescence intensity is proportional to absorption. The absorption, $\mu_e = [(\mu^+ + \mu^-)/2]$, and dichroism, $\mu_m = [\mu^+ - \mu^-]$, spectra were measured by alternating between opposite helicities of incoming x-rays at each photon energy with fixed applied magnetic field.

The imaginary parts of chemical and magnetic resonant scattering factors, $f''_{e,m}$, are related to the measured absorption spectra of Gd through the optical theorem,

$$(C.1) \quad f''_{e,m} = \frac{\mu_{e,m}}{2\lambda n_{at} r_e},$$

where r_e is the classical electron radius, n_{at} is the atomic density of the element, and λ is the wavelength. The real and imaginary parts of resonant scattering factors are related to each other by Kramers-Kronig relations (or dispersion relations) that can

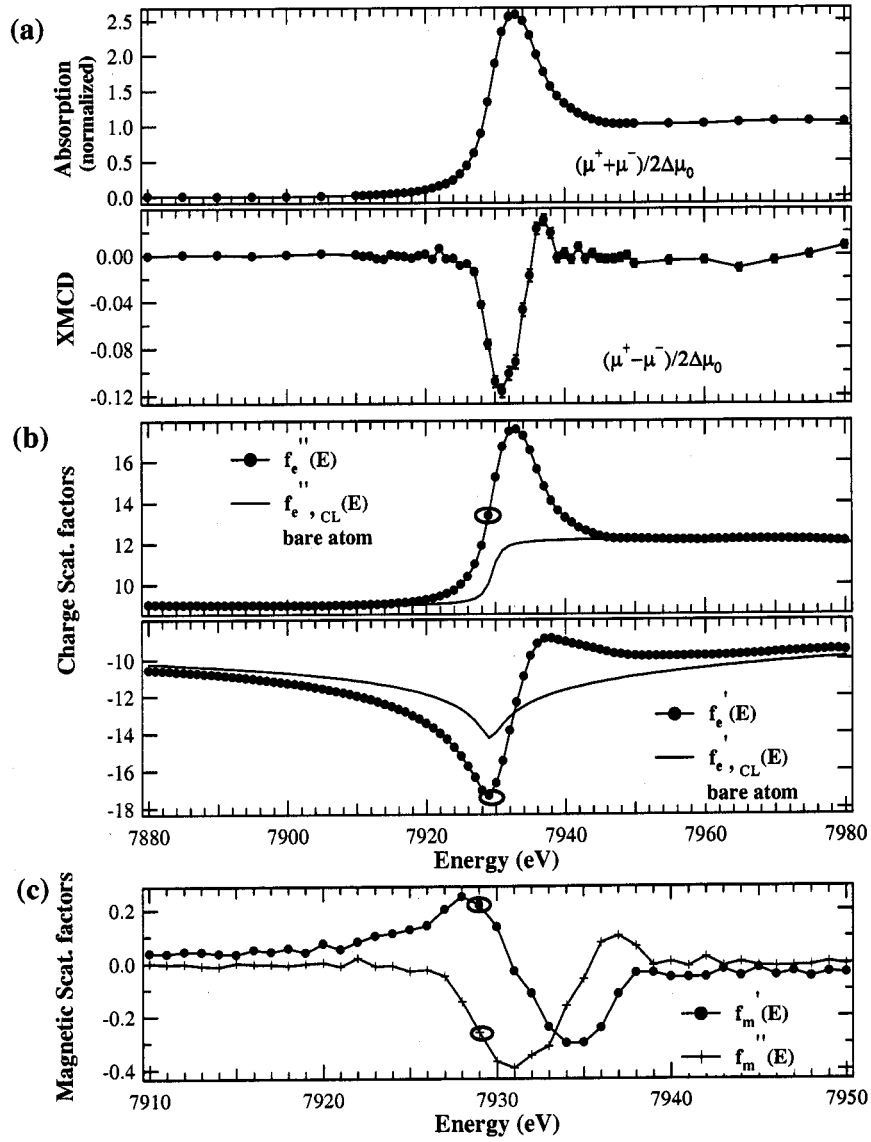


Figure C.1. Absorption measurements in fluorescence geometry near the Gd L_2 edge at $T=20$ K, and 2.1 kOe applied field. (a) Edge-jump normalized sum and difference of the two intensities with opposite helicities. Charge (b) and magnetic (c) scattering factors across the Gd L_2 edge. (b) shows tabulated atomic scattering factors for a single atom (f_e'') and experimentally derived atomic scattering factors including solid-state effects (f_e'). The circles on the graphs denote the energy at which the reflectivity measurements were performed.

be written as [84]:

$$\begin{aligned}
 f'(\omega) &= 1 + \frac{2}{\pi} P \int_0^\infty \frac{\omega' f''(\omega')}{\omega'^2 - \omega^2} d\omega' \\
 f''(\omega) &= -\frac{2\omega}{\pi} P \int_0^\infty \frac{f'(\omega') - 1}{\omega'^2 - \omega^2} d\omega'
 \end{aligned}
 \tag{C.2}$$

where ω is the frequency ($\hbar\omega \cdot \lambda = E$) and P means that the principal part of the integral is to be taken. The real parts of resonant scattering factors, $f'_{e,m}$, were obtained using differential Kramers-Kronig transforms [83]. The procedure uses tabulated scattering factors away from resonance for absolute normalization [47]. Resonant scattering factors for Gd are shown in Figure C.1. Since the real part of the magnetic scattering factor dominates the resonant magnetic scattering, the incident photon energy was tuned to 7929 eV, where f'_m is maximized.

C.2. Optical constants

For x rays, the complex refractive index is close to 1 and it can be written as,

$$n(E) = 1 - \delta(E) + i\beta(E). \tag{C.3}$$

where δ and β are related to the dispersion and absorption in the medium, respectively. The atomic scattering factors and these optical constants are related by,

$$\begin{aligned}
 \delta(E) &= \frac{r_e h^2 c^2 n_{at}}{2\pi E^2} f'(E) \\
 \beta(E) &= \frac{r_e h^2 c^2 n_{at}}{2\pi E^2} f''(E)
 \end{aligned}
 \tag{C.4}$$

where r_e is the classical electron radius, n_{at} is the atomic density of the element, and E is the incoming photon energy. For a given material, $r_e h^2 c^2 n_{at} / 2\pi$ can be treated

as constant, and thus the above equations can be expressed as,

$$\begin{aligned}
 \delta(E) &= X \frac{f'(E)}{E^2} \\
 \beta(E) &= X \frac{f''(E)}{E^2} \\
 (C.5) \quad X &= \frac{r_e h^2 c^2 n_{at}}{2\pi}
 \end{aligned}$$

where the energy-independent parameter X can be obtained by comparing tabulated values of $\delta(\beta)$ and $f'(f'')$ at any energies.

For accurate analysis of resonant scattering data (for example, resonant x-ray reflectivity), accurate optical constants are needed. Since the tabulated atomic scattering factors at resonant energies are often not accurate (as described in the previous section), the tabulated optical constants can be inaccurate at resonant energies. For resonant x-ray measurements, once f'' is obtained through an absorption measurement, f' can be calculated using Kramers-Kronig transforms. With these parameters, optical constants at resonant energies can be calculated using the above equations.

APPENDIX D

Micromagnetic Simulation

Micromagnetics is the continuum theory of magnetic moments to describe magnetic microstructure. Micromagnetics is based on the variational principle in which the vector field of magnetization directions $\mathbf{m}(\mathbf{r}) = \mathbf{M}(\mathbf{r})/M_S$ is chosen to minimize the total energy under the constraint $\mathbf{m}^2=1$. With the minimum energy principle and the constant magnetization constraint, the torque on the magnetization at each point, as derived from the energy by variational calculus, has to vanish [85].

For ferromagnetic materials, the equilibrium magnetic state can be calculated by finding the minimization state of the system's free energy. The minimization state can be reached by balancing exchange, magnetocrystalline anisotropy, self-magnetic field, and surface anisotropy energies. The continuous magnetization distribution of a ferromagnetic film is approximated by a discrete magnetization distribution consisting of equally sized cells with the constraint of constant magnetization M_S . With the fixed magnitude of the magnetization, only its direction is varied until the minimum energy state is reached. The output of the calculation is the orientation of the magnetization of each cell and the contribution of each energy to the total energy.

A local magnetic configuration can be found by solving the Landau-Lifshitz-Gilbert equation in the following form [51, 52, 53].

$$(D.1) \quad \frac{\partial \mathbf{M}}{\partial t} = -\frac{1}{1+\alpha^2} \left[\gamma \mathbf{M} \times \mathbf{M}_{eff} + \frac{\gamma\alpha}{M_S} \mathbf{M} \times (\mathbf{M} \times \mathbf{H}_{eff}) \right]$$

γ is the gyromagnetic frequency, α is the damping factor, \mathbf{H}_{eff} is the effective field, M_S is the saturation magnetization, and \mathbf{M} is the sample magnetization. The effective magnetic field on each magnetic moment, \mathbf{H}_{eff} , is determined from the total system energy as $\mathbf{H}_{eff} = -\partial E_{tot}/\partial \mathbf{M}_S$. The effective magnetic field includes all the effects from exchange, anisotropy, external fields and demagnetizing fields.

The exchange energy is related to the fundamental property of a ferromagnet that prefers a constant equilibrium magnetization direction. Any deviation from the constant direction is compensated by a energy penalty that is described by the “stiffness” equation [51]:

$$(D.2) \quad E_{ex} = A \int (\text{grad } \mathbf{m})^2 dV.$$

V is the volume, and A is a exchange stiffness constant, a material constant, in units of J/m or erg/cm . As in multilayer thin films, when two different media are in contact, the exchange interface coupling is usually different from the bulk exchange coupling. The interface coupling can be expressed phenomenologically as an interface energy density function [86],

$$(D.3) \quad e_{Int} = C_1(1 - \mathbf{m}_1 \cdot \mathbf{m}_2) + C_2(1 - (\mathbf{m}_1 \cdot \mathbf{m}_2)^2).$$

Here $\mathbf{m}_{1,2}$ are the magnetization vectors of layer-1 and layer-2. C_1 and C_2 are the bilinear and biquadratic coupling constants, respectively. $C_1 > 0$ will lead to a parallel alignment between \mathbf{m}_1 and \mathbf{m}_2 , and $C_1 < 0$ will lead to an antiparallel alignment. If the biquadratic coupling is dominant and $C_2 < 0$, a perpendicular orientation between $\mathbf{m}_{1,2}$ becomes favorable.

The anisotropy energy describes the interaction of the magnetization direction with the structural axes of the material. This interaction is originated from spin-orbit interactions, and the anisotropy can be distinguished between crystal anisotropy of undisturbed crystal structure and induced anisotropy due to any deviations from the ideal case [85].

The external field energy is also called *Zeeman energy*, and it describes the interaction energy of the magnetization vector field with an external field H_{ext} as:

$$(D.4) \quad E_{Zeeman} = -M_s \int \mathbf{H}_{ext} \cdot \mathbf{m} dV.$$

This energy depends on the net magnetization of the sample but not on detailed domain structures.

The demagnetizing field energy (also called stray field energy, magnetic dipole interaction, or magnetostatic energy) arises from the magnetic field generated by the magnetic body itself. The stray field generated by the divergence of the magnetization \mathbf{M} is expressed as:

$$(D.5) \quad \text{div } \mathbf{H}_d = -\text{div } (\mathbf{M}/\mu_0),$$

where μ_0 is vacuum permeability. The stray field (demagnetizing) energy can be written as:

$$(D.6) \quad E_d = \frac{1}{2}\mu_0 \int^{all \ space} \mathbf{H}_d^2 dV = -\frac{1}{2} \int^{sample} \mathbf{H}_d \cdot \mathbf{M} dV$$

This energy can be considered as the energy needed to bring up the constituent dipoles from infinity or the energy associated with a given magnetization distribution.

The stray field (demagnetizing field) can be expressed as $\mathbf{H}_d = -N\mathbf{M}$ where N is a dimensionless demagnetizing factor that depends on the sample geometry.

The minimum energy state is found iteratively using a relaxation method based on the calculations of the variations of the total energy due to an infinitesimal rotation of the magnetization vectors. For LLG Micromagnetic Simulator program [50], the convergence criterion for exiting the calculation is when the largest relative change in the largest component of the directional cosines is less than $10^{-7} \sim 10^{-9}$. For OOMMF program [61], the convergence criterion is when the largest value of when the torque $|\mathbf{M} \times \mathbf{H}|/M_S^2$ over all the spins is less than $10^{-4} \sim 10^{-5}$.